Change in tropical cyclone integrated kinetic energy between present and future climate in the CNRM climate model

Master's Thesis
MSc Climate Physics: Meteorology & Physical Oceanography

Faculty of Mathematics and Natural Sciences
Christian-Albrechts-University zu Kiel
GEOMAR – Helmholtz Centre for Ocean Research Kiel

Author: **Philip Kreußler**
Matriculation Number: **1018085**

First Examiner: Prof. Dr. Katja Matthes
Second Examiner: Dr. Louis-Philippe Caron

Kiel, 26 May 2020

Table of Contents

Abstract

Tropical cyclones (TCs) pose a great threat to lives and have the potential to induce huge financial losses. In particular, insurance businesses are interested in estimating the damage potential of TCs and their future developments. Commonly used indices to assess the destructive potential of TCs focus on the use of the maximum wind speed only. They fall short to include the size of the storms, which has been found to be a crucial factor to estimating cyclone-related damages. Integrated Kinetic Energy (IKE) is a recent integrated measure which takes into account maximum intensity and the spatial extent of the wind field. As the first study to do so, this work investigates the effect of increased horizontal model resolution and the impact of climate change on the simulation of IKE of TCs. This is done by comparing various integrations of the CNRM climate model: two uncoupled atmosphere-only experiments for a historical forced simulation (1950-2014) and a future projection (2015-2050), following the CMIP6 HighResMIP protocol, each run at a standard (LR: $1.4° \times 1.4°$) and an enhanced resolution (HR: $0.5° \times 0.5°$).

Analyses of the TC climatology in the northern hemisphere (NH) show an increase in storm intensity and frequency with resolution in all ocean basins. However, the number of storms in both configurations is still biased low with respect to observations. Surprisingly, comparing the present and the future period in LR and HR against each other does not reveal a considerable change in global TC activity. Probability densities (PDs) of TC maximum lifetime IKE in the Western North Pacific (WNP) and the North Atlantic (NA) are significantly impacted by the refinement in resolution, although the opposing effects of higher wind speed and reduced storm size with resolution somewhat balance one another and result in relatively similar IKE values, with storm size being the stronger IKE driver. Seasonally accumulated track IKE (TIKE) is considerably higher in HR than in LR for all basins, owing to the higher storm frequency. The increase from LR to HR is most pronounced over the NA, where the range of the TIKE exhibits reasonable values compared to observations. Interestingly, it is shown that for both resolutions there is no clear impact of the change in forcings on storm size and intensity which is in contrast to previous studies. Consequently, the PDs of maximum IKE are not significantly distinguishable from one another between the periods and no robust basin wide changes could be found in any of the basins.

Overall, the presented study highlights the relevance of model resolution for estimating TC IKE as it impacts storm intensity and size. Including the storm size in IKE estimates is emphasised as it can balance the effect of changing intensities. The influence of a changing climate on maximum IKE of the simulated storms in this particular model and experiment configuration is unexpectedly low, potentially owing to the single ensemble member tested here. Especially, insurances could benefit from further studies to establish IKE as a robust measure to extrapolate future changes in losses related to TCs.

Zusammenfassung

Tropische Zyklonen (TCs) stellen eine lebensgefährliche Bedrohung dar und haben das Potenzial, enorme finanzielle Verluste zu verursachen. Insbesondere Versicherungsunternehmen sind daran interessiert, das Schadenspotenzial von TCs und deren Entwicklung in der Zukunft abzuschätzen. Häufig verwendetete Indizes um das zerstörerische Potenzial von TCs zu erfassen konzentrieren sich lediglich auf die Verwendung der maximalen Windgeschwindigkeit. Sie vernachlässigen die Einbeziehung der Sturmgröße, welche als wesentlicher Faktor für die Bestimmung von Schäden durch Zyklonen identifiziert werden konnte. Integrierte Kinetische Energie (IKE) ist eine Größe, die neben der maximalen Windgeschwindigkeit auch die räumliche Ausdehnung des Windfeldes miteinbezieht. Als erste Studie untersucht diese Arbeit den Einfluss einer verbesserten horizontalen Modellauflösung und die Auswirkung des Klimawandels auf die Simulation der IKE von TCs. Dies wird durch den Vergleich verschiedener Modellläufe des CNRM Klimamodells realisiert: Zwei ungekoppelte Experimente mit einem Atmosphärenmodell, eine Simulation mit historischen Klimabedingungen (1950-2014) und eine Zukunftsprojektion (2015-2050), die beide dem CMIP6-HighResMIP-Protokoll folgen, werden jeweils mit einer Standardauflösung (LR: $1.4° \times 1.4°$) und einer erhöhten Auflösung (HR: $0.5° \times 0.5°$) durchgeführt.

Analysen der Klimatologie der TCs in der nördlichen Hemisphäre (NH) zeigen einen Anstieg der Sturmintensität und -frequenz mit der Modellauflösung in allen Ozeanbecken, dennoch bleibt die Anzahl der Stürme unter den Werten von Beobachtungen. Überraschenderweise liefert der Vergleich zwischen den beiden Zeiträumen mit unterschiedlichen Klimabedingungen keinen erheblichen Unterschied in der globalen Aktivität von TCs. Die Wahrscheinlichkeitsdichten (PDs) der maximalen IKE der TCs im westlichen Nordpazifik (WNP) und Nordatlantik (NA) werden signifikant durch die Verbesserung der Auflösung beeinflust, obwohl sich der gegenteilige Effekt von erhöhten Windgeschwindigkeiten und reduzierten Sturmgrößen mit der Auflösung nahezu gegenseitig ausgleichen und zu vergleichbaren IKE-Werten führen, wobei die Sturmgröße der ausschlaggebende Faktor für die IKE ist. Die IKE, kumuliert über die Zugbahnen aller TCs einer Sturmsaison (seasonal TIKE), zeigt in HR beträchtlich erhöhte Werte im Vergleich zu LR, begründet durch die höhere Sturmfrequenz. Der größte Anstieg von LR zu HR ist im NA festzustellen, wo die Reichweite der TIKE realistische Werte verglichen mit Beobachtungsdaten liefert. Interessanterweise wird für beide Modellauflösungen gezeigt, dass kein klarer Einfluss durch die unterschiedlichen Klimabedingungen auf Sturmintensität und -größe ausgeübt wird, was im Widerspruch zu anderen Studien steht. Folglich können die PDs der maximalen IKE nicht signifikant zwischen den zwei Zeiträumen unterschieden werden und in keinem der Ozeanbecken können robuste Änderungen festgestellt werden.

Die vorgelegte Studie hebt die Relevanz der Modellauflösung für die Abschätzung der IKE von TCs hervor, da diese die Sturmintensität und -größe beeinflusst. Des Weiteren zeigt sie die Wichtigkeit der Einbeziehung der Sturmgröße für die Abschätzung der IKE, da sie den Einfluss sich ändernder Windgeschwindigkeiten ausgleichen kann. Der Einfluss des Klimawandels auf die maximale IKE der simulierten Stürme in dieser Modell- und Experimentanordnung ist unerwarteterweise gering, möglicherweise zurückzuführen auf das Testen von nur einem Ensemble-Mitglieds. Besonders Versicherungsunternehmen könnten von weiteren Studien zur Etablierung der IKE als robustes Maß für die Extrapolierung von zukünftigen Änderungen in Schäden und Verlusten hervorgerufen durch TCs profitieren.

List of Abbreviations

ACE	Accumulated Cyclone Energy
AMM	Atlantic Meridional Mode
AMO	Atlantic Multidecadal Oscillation
AWP	Atlantic Warm Pool
CDF	Cumulative Distribution Function
CMIP	Coupled Model Intercomparison Project
CNRM	Centre National de Recherches Météorologiques
ENP	Eastern North Pacific
ENSO	El Niño/Southern Oscillation
HighResMIP	High Resolution Model Intercomparison Project
HR	High Resolution
IKE	Integrated Kinetic Energy
IPCC	International Panel on Climate Change
ITCZ	Intertropical Convergence Zone
KE	Kinetic Energy
KS	Kolmogorov-Smirnov
LR	Low Resolution
MJO	Madden-Julian Oscillation
MSLP	Mean Sea Level Pressure
NA	North Atlantic
NH	Northern Hemisphere
NOAA	National Oceanic and Atmospheric Administration
PD	Probability Density
PDF	Probability Density Function

PDI	Power Dissipation Index
PDO	Pacific Decadal Oscillation
SH	Southern Hemisphere
SSHWS	Saffir-Simpson Hurricane Wind Scale
SSP	Shared Socioeconomic Pathway
SST	Sea Surface Temperature
TC	Tropical Cyclone
TIKE	Track Integrated Kinetic Energy
WCRP	World Climate Research Programme

1 Introduction

Natural disasters are high-impact events that affect thousands of people worldwide each year (*World Economic Forum*, 2019). They pose a great threat to lives and have the potential to cause significant damage to property, structures and to provoke considerable financial losses (*Munich Re*, 2018). Tropical cyclones (**TC**s) - intense storms that form over warm tropical oceans and are characterised by low atmospheric pressure (e.g., hurricanes in the Atlantic) - are one of the costliest catastrophes (*Landsea*, 2000; *Emanuel*, 2005; *Aon Benfield*, 2018; *Munich Re*, 2018) as they can bring a number of hazards such as high winds, heavy precipitation, storm surges, inland and coastal flooding, tornadoes or landslides. An infamous example is the *Bhola Cyclone* (1970) that struck present-day Bangladesh and killed in excess of 300 000 people (*Landsea*, 2000). It is regarded as the deadliest TC on record and as one of the deadliest natural disasters to have ever occurred. As of today, *Hurricane Katrina* (2005) has been the costliest TC with US$160 billion in damage, followed by *Hurricane Sandy* (2012) (*NOAA*, 2018). A few of the storms from the 2017 Atlantic hurricane season (*Hurricanes Harvey*, *Irma* and *Maria*) also rank among the storms associated with the highest financial losses. More recent examples like *Hurricane Dorian* (2019) and *Cyclone Harold* (2020), which caused widespread damage across the Bahamas and in the South Pacific respectively, show that TCs have the potential to threaten some of the most vulnerable countries which makes them especially dangerous.

As a large portion of the costs caused by TCs is insured (*Munich Re*, 2018), insurance companies are highly interested in predicting storm activity and the associated potential damages and losses. Traditionally, the destructive potential of TCs is estimated by their maximum intensity, i.e., their 1-minute maximum sustained wind speed and classification on the Saffir-Simpson Hurricane Wind Scale (**SSHWS**) (*Simpson*, 1971; *NOAA*, 2019) which can be seen in Tab. 1. Commonly used indices to estimate the damage potential are the Accumulated Cyclone Energy index (**ACE**) (*Bell et al.*, 2000) and the Power Dissipation Index (**PDI**) (*Emanuel*, 2005) which are integrated measures of number, intensity and duration of cyclones that can be used to represent the level of activity of a hurricane season. ACE and PDI have the ability to reflect changes in key factors influencing TC activity, such as sea surface temperatures (**SST**s) (*Camargo & Sobel*, 2005; *Villarini & Vecchi*, 2012). Particularly, the PDI has been found to show empirical and statistical relationships with further key factors like wind shear and vorticity which can help simulate future TC activity in a changing climate (*Emanuel*, 2007), making both indices useful tools. However, ACE and PDI neglect the actual storm size which is why these measures introduce uncertainties to damage estimates (*Kantha*, 2006). For instance, the ACE has been suggested to inordinately overestimate the energy content of TCs (*Yu et al.*, 2009; *Yu & Chiu*, 2012). Studies by *Mahendran* (1998), *Kantha* (2006)

Description	Category	Wind speed in $\mathrm{m\,s^{-1}}$	Wind speed in $\mathrm{km\,h^{-1}}$	Associated minimum pressure in hPa
Major hurricane	5	≥ 70	≥ 252	< 920
Major hurricane	4	58 – 69	209 – 251	920 – 945
Major hurricane	3	50 – 57	178 – 208	945 – 965
Hurricane	2	43 – 49	154 – 177	965 – 980
Hurricane	1	33 – 42	119 – 153	> 980
Tropical storm	0	18 – 32	63 – 118	> 1000

Table 1: SSHWS with associated categorisation and ranges of wind speed and minimum pressure (*Simpson*, 1971; *Kantha*, 2006; *NOAA*, 2019).

and *Zhai & Jiang* (2014) show that including the storm size and structure is beneficial to damage estimates and the explained variance in associated losses.

A more recent measure to address this issue, the so-called Integrated Kinetic Energy (**IKE**) (*Powell & Reinhold*, 2007), was developed. This metric includes the size of the storm by integrating the energy of the entire wind field. As IKE is a measure that is equivalent to the wind pressure, it thus is a good indicator for the wind loading on structures and thus potential damages (*ASCE*, 2016), hence why it is supposed to correlate better with damages (*Wang & Toumi*, 2016). Moreover, storms from the past two decades have shown the importance of introducing storm size to damage estimates: hurricanes that caused extensive damage and mortality in the US like *Ivan* (2004) and *Katrina* (2005) were rated relatively weak on the SSHWS at landfall, for example compared to category 5 hurricane *Camille* (1969) which caused considerably less damage. However, in terms of IKE, these storms would be rated as significantly more dangerous owing to the large extent of their wind fields (see Tab. 2), more in line with the large devastation they brought (*Kantha*, 2006; *Powell & Reinhold*, 2007; *Kozar & Misra*, 2019).

Another topic of interest for insurance companies is the projection of damages and losses associated with TCs in the future. The processes determining TC formation, intensification and propagation, and thus defining the related hazards, are non-linear and non-stationary and strongly dependent on the prevalent environmental conditions

Storm name	SSHWS category	Radius of the tropical storm wind field in km	IKE of the tropical storm wind field in TJ
Camille (1969)	5	230	65
Ivan (2004)	3	326	81
Katrina (2005)	3	454	122

Table 2: Comparison of *Hurricanes Camille*, *Ivan* (in Alabama) and *Katrina* (in Louisiana) at landfall with respect to SSHWS category and IKE (*Powell & Reinhold*, 2007).

(*Gray*, 1975). How these conditions will be impacted by anthropogenic climate change will be crucial to assessing the future risk associated with TCs. The relatively short-lived database of observed storms makes it difficult to extrapolate a robust trend in TC characteristics and, moreover, natural variabilities inherent in the climate system may mask existing trends (*Walsh et al.*, 2016; *Knutson et al.*, 2019). Consequently, climate models are the best available tool for assessing potential changes in TCs related to a changing climate and thus for estimating future damages. Recent studies using climate models suggest that certain TC characteristics, including precipitation or the maximum lifetime intensity, are projected to increase (*Knutson et al.*, 2019). Other features like the overall global frequency and storm size have been projected with contradicting results and are still unclear. In particular, changes at the individual ocean basin scale remain highly uncertain (*Knutson et al.*, 2019).

With usual diameters of about 400 km (*Chavas & Emanuel*, 2010), TCs are (relatively) small-scale phenomena, especially compared to extratropical cyclones (see Fig. 1) which typically reach diameters of about 1000 km (*Rudeva & Gulev*, 2007). Thus, the horizontal model resolution plays a crucial role in representing TCs and the processes relevant to their formation. *Krishnamurti et al.* (1989) showed that TC formation and motion could significantly be enhanced with an increase in horizontal resolution because key processes such as surface layer fluxes could be represented with higher fidelity. The importance of horizontal resolution has been further highlighted by various recent studies. These studies find that, among others, TC characteristics like genesis potential, formation, frequency, intensity, size, geographical distribution and climate modes such as the Madden-Julian Oscillation (**MJO**) and El Niño/Southern Oscillation (**ENSO**) - which influence those characteristics - are positively impacted by a refinement in resolution (*Bengtsson et al.*, 2007; *Shaffrey et al.*, 2009; *Caron et al.*, 2011; *Jiang et al.*, 2012; *Shaevitz et al.*, 2014; *Villarini et al.*, 2014; *Camargo & Wing*, 2016; *Walsh et al.*, 2016).

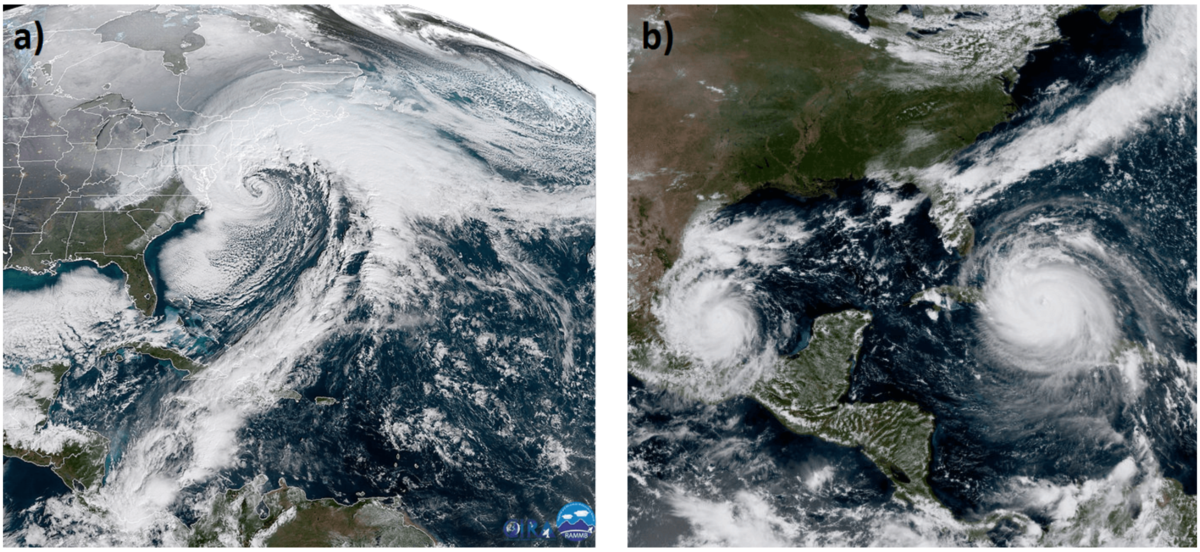

Figure 1: Comparison of the horizontal scale of an extratropical cyclone (a) and two TCs (b) in the Atlantic (`https://scijinks.gov/noreaster/`).

Due to the limitation of computational resources, most model studies during the last decade, which aimed at investigating the impact of climate change on TC characteristics, were restricted to resolutions between 100-300 km (*Walsh et al.*, 2016). These resolutions were capable of producing reasonable figures of the average number of TCs and their variability (*Zhao et al.*, 2009; *Sugi et al.*, 2012). However, the representation of the observed intense TC wind speeds and TC size remained an issue. The models were still too coarse to resolve mixing processes and smaller-scale features within the storms so that the models were unable to intensify storms to the observed strengths and to represent them at the observed smaller storm sizes (*Williams et al.*, 2015; *Walsh et al.*, 2016; *Davis*, 2018). Regional climate models, variable-resolution models or adaptive grids are techniques that enable a local refinement of the model resolution up to 1 km which would be sufficiently fine to resolve TC processes (*Gentry & Lackmann*, 2010), but due to their high computational costs they are not used for climate studies with scales of several decades (*Skamarock & Klemp*, 1993; *Kendon et al.*, 2012; *Tang et al.*, 2013; *Zarzycki et al.*, 2014; *Davis et al.*, 2016; *Baudouin et al.*, 2019).

The H2020 PRIMAVERA project aims at investigating the effects of increased model resolution on the simulated climate and the sensitivity of the model projections to model resolution. Simulations performed in PRIMAVERA follow the High Resolution Model Intercomparison Project (**HighResMIP**) (*Haarsma et al.*, 2016) protocol, defined within the sixth phase of the Coupled Model Intercomparison Project (**CMIP**6). *Roberts et al.* (2020) and *Roberts et al.* (subm.) have provided a first analysis of TC activity in the PRIMAVERA simulations. Both studies show that an enhancement in horizontal resolution toward 25 km leads to a better representation of TC frequency, intensity and spatial distribution relative to observations. They demonstrate that existing low biases in northern hemisphere (**NH**) track density and frequency could be reduced with resolution and that storm intensities increased over all models. Additionally, *Roberts et al.* (subm.) were able to detect mixed responses in NH basins to future forcing.

However, so far, no study has assessed the role of climate change and model resolution on IKE. Given the interest in enhancing TC simulation and predicting the risks associated with them, this study aims at answering the following two questions:

- What is the influence of a refinement in horizontal model resolution on the simulation of Integrated Kinetic Energy?
- How is Integrated Kinetic Energy impacted by a future climate change scenario?

These questions will be addressed by using a cyclone tracker to analyse two integrations of the CNRM climate model, which has been found to produce TC wind speeds and frequencies close to observations (*Roberts et al.*, 2020) and thus is a a suitable model. TC activity and IKE statistics in a historical forced experiment and a future projection at a standard and an increased horizontal resolution will be compared in order to obtain insight into their relationships with the prevalent climate conditions and model resolution. The PRIMAVERA project offers the ideal framework to perform these experiments and to contribute to answering the questions mentioned above.

The structure of this study is as follows: Sect. 2 provides an overview of the mechanisms and the current state-of-the-art knowledge related to TCs. In Sect. 3, the project framework, technical information on the model, definitions and statistical methods are described. The process of setting up the cyclone tracker used to analyse the model data is outlined in Sect. 4. Sect. 5 presents the findings and discusses them. Finally, in Sect. 6, the conclusions are drawn.

2 Background

2.1 Characteristics of Tropical Cyclones (TCs)

2.1.1 Preconditioning, Formation and Propagation

TCs are an inherent mechanism of the Earth system to redistribute heat between the tropics and the poles. Due to the tilt of the Earth, the tropics receive, on average, more solar energy than higher latitudes which results in an energy imbalance. The planet tries to balance this discrepancy by transporting heat poleward via the mean atmospheric and oceanic circulations. The atmosphere accounts for the majority of this transport as air can travel at faster speeds than water, is also available over the continents and because the troposphere extends, on average, more than the ocean. Nevertheless, at times of intense differential heating like the respective hemispheric summer months, the regular, laminar atmospheric flow can fail to balance this discrepancy. As a consequence, the meridional temperature gradient becomes very pronounced and thus provides an energy source for a more effective, turbulent flow that can lead to meso- to synoptic scale eddies like TCs. In more detail, a list of preconditions has to be met before tropical cyclogenesis can be initiated and a tropical storm can be born (*Gray*, 1975):

- High enough SSTs to fuel the storm with energy;
- Large enough distance to the equator to allow Coriolis force to deviate inflow of air (at least 5°);
- Atmospheric instability to allow for convection;
- Sufficient humidity in the lower and middle part of the troposphere to facilitate condensation and to provide enough energy to maintain the system;
- Low-level disturbances with sufficient vorticity and convergence to enable organised convection;
- Little vertical wind shear to prevent the storm from being vertically disrupted (barotropic conditions).

A TC is a prime example of a Carnot heat engine in which heat energy is extracted from the ocean and converted to kinetic/mechanical energy (i.e., wind) and dissipated by surface friction (*Emanuel*, 1987). In order to provide enough heat energy, SSTs need to exceed 26.5°C so enough water can evaporate (typically in the tropics), rise and form a pronounced negative sea surface air pressure anomaly. As adjacent air tries to balance the negative anomaly, a convergent inflow of air is created which is further accelerated and deviated away from the centre of the anomaly by the Coriolis force to form an anti-clockwise rotating system in the NH and a clockwise rotating system in the southern

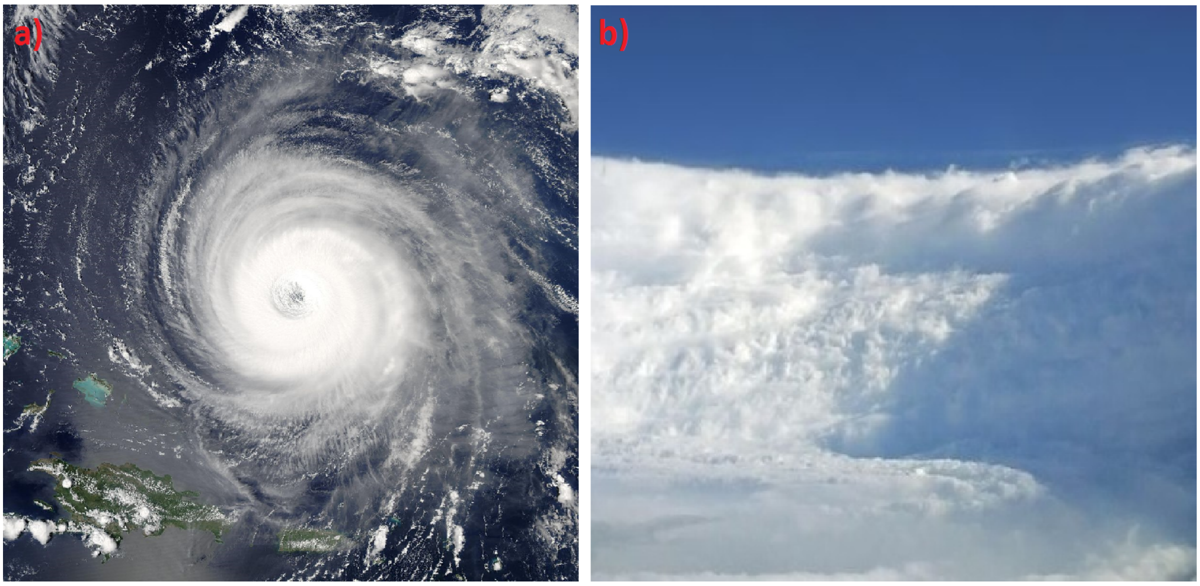

Figure 2: (a) A satellite image of *Hurricane Isabel* in 2003 with clearly visible spiral structures (https://upload.wikimedia.org/wikipedia/commons/thumb/7/7e/Hurricane_isabel2_2003.jpg/1200px-Hurricane_isabel2_2003.jpg). (b) Depiction of the eyewall and eye of *Hurricane Katrina* in 2005 as seen from a Hurricane Hunter aircraft (https://thenanitesolution.wordpress.com/2016/03/26/how-does-a-hurricane-form/).

hemisphere (**SH**): a cyclone. If the atmosphere is unstable and facilitates convection, the warm air continues to rise and to rotate cyclonically. During its ascent through the troposphere, the positive vorticity created by the convergent airflow needs to be maintained and organised to form a potent storm. Low-level disturbances in the atmosphere can provide the convergence and vorticity needed to do so. These features often arise from tropical waves, disturbances in the intertropical convergence zone (**ITCZ**), monsoon troughs, interaction with orophraphy or from outflow boundaries of other mesoscale storm systems. Additional surface frictional forces lead to an inward displacement of the converging air and the typical inward spiraling structures arise which are well known from satellite imagery (Fig. 2a).

Once the ascent of the storm is organised, condensation of moisture held by the air and the associated latent heat release can trigger thunderstorms and play an important role in providing extra energy to maintain the system. As the air further rises, it cools and creates an upper-level high air pressure anomaly that leads to an increasing outflow of air near the top of the storm (height at which no further uplift is possible due to missing buoyancy) where large cirrus cloud shields form. The divergent airflow is characterised by negative vorticity and hence has an opposite rotation to that of the surface inflow. The ascent of air within the moist, cloudy and rainy structure of the storm requires an equal amount of descending air within the core (eye) of the storm or further away from the centre where dry and cloud free conditions can be found. The eyewall is where the highest winds and rain bands with the strongest precipitation can be observed (Fig. 2b).

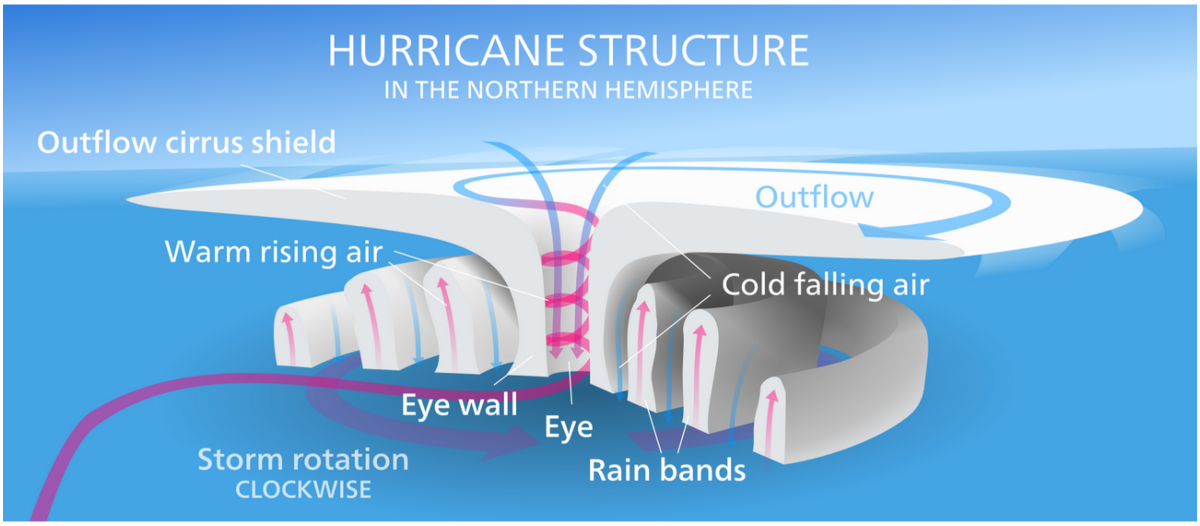

Figure 3: Schematic depiction of the processes relevant to TC formation (https://sites.google.com/site/kimberlyshurricanes/causes-of-hurricanes).

The entire system can be sustained as long as the heat supply can balance the energy lost to friction or until the atmosphere becomes too baroclinic. In strongly baroclinic conditions, vertical wind shear becomes too strong due to rapid changes in surface temperature and thus disrupts the vertical organisation of the storm, i.e., the lower and upper part of the storm will be disconnected from each other and the upper part will not be supplied with sufficient moisture and latent heat energy to maintain itself (*Emanuel*, 1987). This limits the growth potential of the storm and plays a major role in determining the size of a storm. Together with quick surface pressure changes, the absence of a heat/energy source is the main reason why tropical storms rapidly weaken and decay after entering regions of cooler SSTs (usually higher latitudes) or making landfall. Fig. 3 summarises the described processes relevant to TC formation.

Whenever the above conditions are met, TCs can develop and be sustained. Usually, they are about 200 km in radius but can reach up to several hundreds of kilometres of radius (*Chavas & Emanuel*, 2010) and exceed wind speeds of 250 $\mathrm{km\,h^{-1}}$ (*Simpson*, 1971; *NOAA*, 2019). All three main ocean basins can develop TCs and have their respective names for them: In the North Atlantic (**NA**) and the Eastern North Pacific (**ENP**) the storms are called *hurricanes*, in the Western North Pacific (**WNP**) *typhoons* and in the South Pacific and Indian Ocean simply *tropical cyclones*. According to their maximum intensity, i.e., their 1-minute maximum sustained wind speed, they are categorised into different storm categories on so-called TC intensity scales of which the most known is the SSHWS. Further differences between the basins concern the hemisphere in which the TCs form. Fig. 4 displays recorded storm tracks from the IBTrACS data base from 1979-2007 by *Knapp et al.* (2010) and shows that there are almost no registered storms in the South Atlantic and in the eastern part of the South Pacific. This is mainly due to

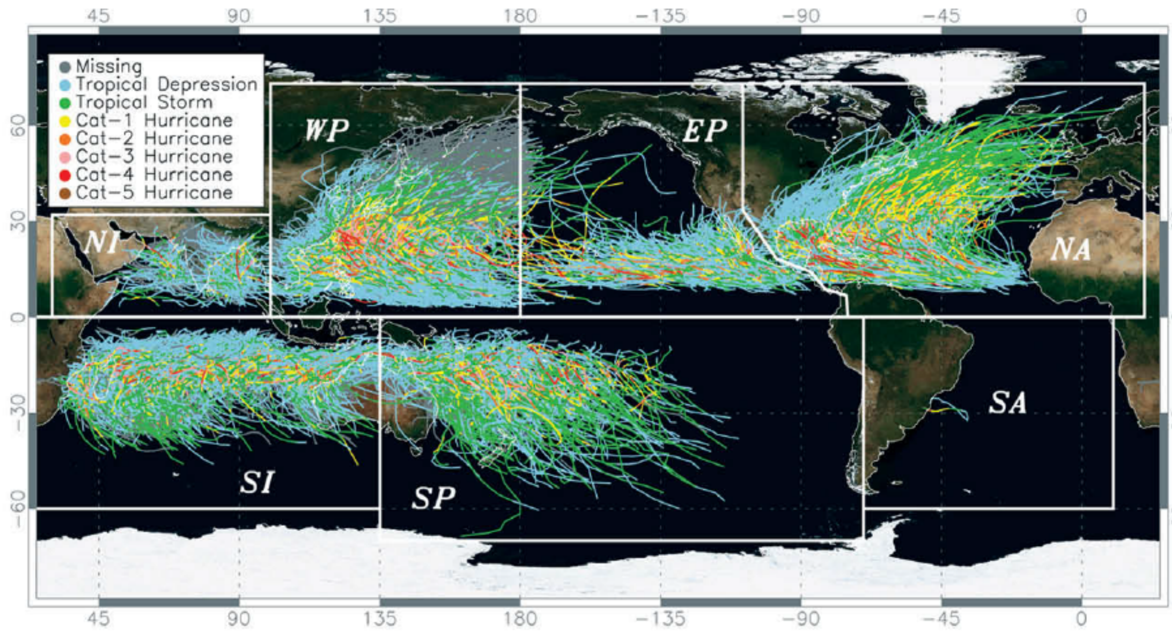

Figure 4: Global recorded storm tracks from the IBTrACS data base from 1979-2007 (*Knapp et al.*, 2010). For the study by *Knapp et al.* (2010) the respective basins were outlined and abbreviated: North Indian (NI), Western North Pacific (WP), Eastern North Pacific (EP), North Atlantic (NA), South Indian (SI), South Pacific (SP) and the South Atlantic (SA).

the lower SSTs in these regions which are advected by the Antarctic Circumpolar Current and its extensions, in specific by the Malvinas Current at the east coast of South America (*Evans & Braun*, 2012) and the Humboldt Current at the west coast (*Terry*, 2007). In the Central South Pacific, further away from the cold-water inflow, the conditions are more favourable for cyclone formation, especially in late summer when SSTs are the highest and provide.

Further factors exacerbating cyclone formation in the eastern South Pacific and South Atlantic are strong vertical wind shear and the lack of tropical disturbances. The strong vertical wind shear, which is a consequence of the prevalent temperature and landmass patterns, removes the heat and moisture from the axis of rotation of the storm system and prevents the storm from growing vertically (*Gray*, 1975). The landmass distribution between the tropics in the NH and the SH, especially in the Atlantic Ocean, also influences the required disturbances in the pressure field and thus the available vorticity: Less landmass in the SH leads to a less southward displacement of the ITCZ during summer and thus results in less disturbances in the development regions of the cyclones. Moreover, the lack of landmass south of the equator hampers the development of a SH counterpart of the African Easterly Jet in the NH which generates tropical disturbances and thus is the main source of storm seeds in the NA (*Landsea et al.*, 1998). In addition, the shape of the continents and the ocean basin in the South Atlantic feature a lack of space for storms to grow and intensify sufficiently.

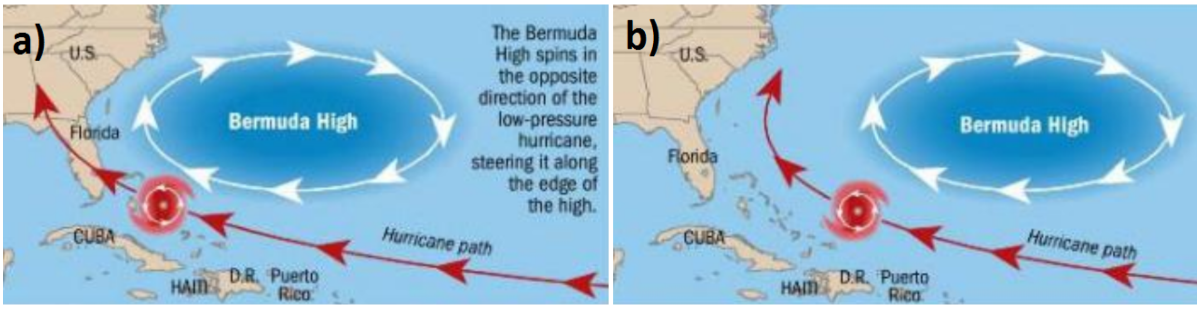

Figure 5: (a) A more pronounced and extended Bermuda High has impacts on the steering of Atlantic hurricanes and influences their probability of making landfall in the US. (b) Vice versa: a weaker and more contracted Bermuda High allows for an early northward propagation of the storms and decreases the probability of US landfalls (http://www.atmo.arizona.edu/students/courselinks/fall15/atmo336/lectures/sec2/hurricanes2.html).

Overall, about 80 TCs form under these conditions around the globe per year of which approximately 70% develop in the NH and 30% in the SH (*Ramsay*, 2017). As suggested by Fig. 4, in the NH the Western Pacific is the basin that hosts the most storms with about 25 cyclones on average per year, followed by the Eastern Pacific with 15, the Atlantic with 13 and the Indian with about 3 storms (*Ramsay*, 2017). Fig. 4 also reveals that there seems to be a common pattern of propagation for storms in all basins: first, a westward propagation, followed by a deflection toward the respective hemispheric pole and occasionally an eastward retroflection. In fact, the biggest influence on a cyclone's track are the prevailing local wind patterns (*Carr III & Elsberry*, 1990). The stronger these steering winds are, the faster a storm will move. Usually, the trade winds are responsible for the westward steering of the storm. But also, mid and upper troposphere conditions can significantly influence the track as troughs will lead to a displacement of the lower troposphere system toward the trough (*Molinari & Vollaro*, 1989). On the contrary, high pressure features like subtropical highs can act as blocks and steer the storm away or around them. For example, the Bermuda High in the Atlantic is an important mechanism for determining whether a hurricane will make landfall in the US or turn poleward before hitting land (*Wang et al.*, 2011). If the high is stronger and more extended – initiated by a strong contrast in ocean surface and air temperature in summer – the cyclones are steered along the high and toward the coast of the US (Fig. 5a). In late summer and autumn, the temperature difference weakens and the subtropical high is less pronounced and more contracted, steering cyclones northward before they approach the US coast (Fig. 5b).

2.1.2 Natural Variability

Like almost all other natural processes, TCs are subject to natural variability driven by changes in environmental conditions (*Gray*, 1984; *Shapiro*, 1989; *Gray & Landsea*, 1992;

Elsner & Kocher, 2000; *Fink et al.*, 2010; *Kossin et al.*, 2010; *Hodges & Elsner*, 2012). These variabilities may occur at a variety of time scales and can impact the formation of cyclones, their frequency, intensity, distribution, lifetime and tracks. It is important to identify and understand these variabilities, especially on interannual and decadal time scales, since they can mask the long-term trend driven by anthropogenic climate change (*Walsh et al.*, 2016).

The most important process operating at the intraseasonal time scale and impacting TCs in all major basins is the MJO (*Camargo et al.*, 2009). The MJO is the most prominent mode of intraseasonal variability in the tropics and characterised by large-scale fluctuations of atmospheric deep convection along the equator with a period of about 30-80 days (*Madden & Julian*, 1972; *Madden & Julian*, 1994; *Zhang*, 2005). Fields known to impact TC activity like wind shear, vorticity and moisture are modulated by the MJO. For instance, *Klotzbach* (2014) was able to link increased TC formation to the enhancement of convection in MJO affected regions.

Another oscillation influencing TCs in multiple basins is ENSO. ENSO is an interannual coupled ocean-atmosphere phenomenon and describes the variability in tropical Pacific SSTs and their feedback with the atmospheric circulation (*Trenberth*, 1997). While a positive ENSO phase increases TC activity in the Central North Pacific and the South Pacific (*Chan*, 1985; *Chu & Wang*, 1997; *Lander*, 1994), it decreases activity in the Atlantic and in the Australian region (*Nicholls*, 1979; *Revell & Goulter*, 1986; *Gray*, 1984) and shifts activity in the WNP. El Niño events tend to increase upper troposphere westerly winds and increase the vertical wind shear in the Atlantic which contributes directly to decreased numbers of Atlantic storms (*Pielke & Landsea*, 1999). La Niña events typically bring opposite conditions than El Niño events and thus are connected to higher numbers of Atlantic storms.

Further climate variabilities affecting TCs in the Atlantic include the Atlantic Multidecadal Oscillation (**AMO**) (*Goldenberg et al.*, 2001), the Atlantic Meridional Mode (**AMM**) (*Vimont & Kossin*, 2007; *Patricola et al.*, 2014) and the Atlantic Warm Pool (**AWP**) (*Wang et al.*, 2011). These variabilities modulate tropical Atlantic SSTs and hence influence conditions for cyclone formation and propagation: SST changes related to AMO and AMM have been shown to impact the stability of the atmosphere, low-level vorticity, wind shear and to modulate the influence of ENSO on TC in the Atlantic (*Bell & Chelliah*, 2006; *Vimont & Kossin*, 2007; *Patricola et al.*, 2014). The AWP strongly alters SSTs of tropical waters in the Caribbean. Its magnitude and size influence the strength of the subtropical high in the Atlantic which thus have a profound impact on hurricane tracks and whether or not these make landfall (*Wang et al.*, 2011). A large AWP introduces eastward steering flow anomalies along the east coast of the US and lead to less storms making landfall (compare Fig. 5). In addition to the above mentioned variabilities, there exist more climate factors that have been identified to modulate Atlantic TC activity such as precipitation in the Western Sahel region (*Gray & Landsea*, 1992; *Fink et al.*, 2010), the North Atlantic Oscillation (*Elsner & Kocher*, 2000; *Kossin et al.*, 2010), the Quasi-Biennial Oscillation (*Gray*, 1984; *Shapiro*, 1989) or the 11-year solar cycle (*Hodges & Elsner*, 2012). The influence of these climate variabilities on TC activity has furthermore been shown to be non-stationary and to be varying with the phase of the AMO (*Caron et al.*, 2015).

The Pacific Decadal Oscillation (**PDO**) is - besides ENSO - one oscillation to be known to impact TCs in the Pacific basin (*Liu & Chan*, 2008). SST changes in the Pacific associated with the PDO have been demonstrated to facilitate cyclone formation, especially in the tropical Western Pacific. *Chan* (2008) showed that during the positive phase of the PDO, when SSTs are higher than normal in the south eastern part of the Western Pacific, atmospheric convection is promoted, thus yielding more favourable conditions for cyclone development. These conditions have the potential to steer the storms so that they can stay over water for a long time which allows them to intensify and become major typhoons.

2.2 Modelling TCs

The first study to investigate TCs in climate models was performed by *Manabe et al.* (1970) who recognised cyclonic vortices in the tropical regions of a global atmospheric circulation model. Although these vortices showed many characteristics of TCs such as low surface pressure, heavy precipitation, strong convergence of air near the surface or the development of a warm-core, the models were unable to sufficiently resolve the vortices and intensify the storms to tropical storm strength. A landmark study on TCs in global models by *Bengtsson et al.* (1982) found that the occurrence of these vortices in a model employing an increased horizontal resolution of 1.875° was similar to that of observed TCs, indicating the importance of horizontal resolution (*Camargo & Wing*, 2016). Further progress was made by *Krishnamurti et al.* (1989) who demonstrated that a high horizontal model resolution (about $1° \times 1°$), adequate resolution of surface layer fluxes and parameterisations of the boundary layer and convection processes significantly improved the representation of storm formation and motion.

Today, many global models have incorporated these processes leading to improved simulations of TC climatology, including reasonable figures of the average number of TCs and their year-to-year variability (*Zhao et al.*, 2009; *Sugi et al.*, 2012). However, present-day models still struggle to accurately represent the observed intense wind speeds (*Williams et al.*, 2015) which leads to a negative bias in severe storms of category 4 and 5. A large portion of the inability to intensify storms to those strengths still arises from the horizontal resolutions used in the simulations (*Walsh et al.*, 2016). Many of the processes critical to TC formation, such as up and downdrafts, convection and cloud formation act on scales too small to be resolved and hence are parameterised. As shown by *Bryan & Rotunno* (2009) and *Davis* (2018), coarse resolutions within TCs (up to 25 km or 0.25°) lead to an over-representation of horizontal mixing of angular momentum which is thus prevented from penetrating inward and which results in a limitation of the maximum possible wind speed. *Gentry & Lackmann* (2010) estimated that a 2 km resolution or better would be needed to accurately simulate the above processes and hence the maximum storm intensity. These resolutions can be achieved in regional climate models or in global variable-resolution models which employ a local refinement of resolution in the area of interest (*Walsh & Ryan*, 2000; *Chauvin et al.*, 2006; *Kendon et al.*, 2012; *Tang et al.*, 2013; *Zarzycki et al.*, 2014). A further technique to locally enhance the resolution is the use of adaptive grids which automatically increase the grid resolution where needed (*Skamarock & Klemp*, 1993). These can be used to locally refine the resolution along the track of a TC and capture the small-scale processes near and within the TC as it moves (*Fulton*, 2001). Due to the computational costs of running models at these resolutions, both methods are commonly used in medium-range weather forecasts rather than in multidecadal climate studies which makes them unavailable for the PRIMAVERA project (*Davis et al.*, 2016; *Baudouin et al.*, 2019).

During the last decade, the resolutions employed in most ocean-atmosphere coupled studies examining TCs at climate time scales typically ranged from 100-300 km and only in the last few years, model resolutions down to 10-50 km have become available due to limitations of computational resources (*Walsh et al.*, 2016). Recent studies incorporating those finer resolutions highlighted the benefits of enhanced resolution for the representation of various aspects of TCs with regard to observations, including genesis potential, formation, frequency, intensity, size, geographical distribution, track and precipitation patterns (*Bengtsson et al.*, 2007; *Caron et al.*, 2011; *Scoccimarro et al.*, 2014; *Shaevitz et al.*, 2014; *Villarini et al.*, 2014; *Walsh et al.*, 2016). Enhanced horizontal resolutions have also been shown to impact different small- and large-scale processes influencing TC characteristics. For instance, *Jiang et al.* (2012) showed that their high-resolution global climate model was able to reproduce the relationship between the MJO and TCs in the North Pacific. *Shaffrey et al.* (2009) demonstrated a reduction in global tropical SST errors and an improved representation of ENSO which both play a key role for TC formation. It is expected that with further refinement of the resolution, the processes affecting TC formation will positively impact their overall representation which is one of the main motivations of the PRIMAVERA project.

2.3 Climate Change and Future Projections

It is of great interest to have an understanding of how TCs and the processes that influence them look like in the future and how climate change will impact them. The relatively short-lived reliable datasets of global TCs make it difficult to establish statistically reliable trends in TC characteristics (*Walsh et al.*, 2016; *Knutson et al.*, 2019) and to attribute them to climate change. The database will become more comprehensive and detailed over time, but a lot of data for historical storms is missing as many storms do not make landfall and the spatial coverage by measurement instruments before the satellite era was scarce. Thus, because there are no long, global reliable datasets from which future TC activity can be extrapolated, global climate models are the main tool to project and estimate future activity.

Knutson et al. (2019) summarise the most recent findings of TC projections in response to a 2°C anthropogenic global warming. The most robust projected change is that sea level rise accompanying the warming will lead to higher storm surges caused by TCs. Further, a globally median increase of 14% in precipitation rates associated with TCs is projected with at least medium-to-high confidence (*Knutson et al.*, 2019). TC intensity, particularly the maximum lifetime surface wind speed (ca. +5%), is also projected to increase at a medium-to-high confidence level. Opinions are more mixed and confidence levels generally lower for projections including a poleward shift of the latitudes of maximum intensity, a decrease in global frequency and an increase of severe category 4 and 5 storms (*Knutson et al.*, 2019). An increase in the most intense storms can be explained by the fact that storms, if they form, can become more intense due to the increased energy supply resulting from increased SSTs. As the mechanisms determining the global annual number of TCs are still poorly understood (*Emanuel & Nolan*, 2004; *Walsh et al.*, 2016), *Held & Zhao* (2011) demonstrated that the increase in CO_2 and SSTs contributes to the reduction of future upward mass flux and they suggested this could be the main driver for decreased TC activity. Further explanations relate the decrease in frequency to an increase in the saturation deficit of the free troposphere with warming (*Camargo & Wing*, 2016). Establishing robust trends in TC tracks across studies remains difficult although several studies suggest a poleward or eastward expansion of TC occurrence, especially in the North Pacific. Projected changes in TC size and translation speed are highly variable between basins and studies and elude a clear trend (*Knutson et al.*, 2019).

3 Data and Methods

3.1 Framework

This study is carried out under the framework of the sixth phase of the Coupled Model Intercomparison Project (CMIP6) which is part of the World Climate Research Programme (**WCRP**). The WCRP aims at facilitating the analysis and prediction of Earth system variability and change in order to determine the predictability of climate and the effect of human activities on climate. The CMIP venture is a framework to harmonise the experiments of all participating institutes and working groups and to make the multi-model output publicly available in a standard format which will then be used for the International Panel on Climate Change (**IPCC**) reports. Every group receives the same input data (e.g., initial atmospheric and oceanic fields, boundary fields, such as CO_2 emissions, solar radiation etc.) and conducts the experiments following the provided guidelines to see how the different model formulations will produce different outcomes. This way, a better understanding of past, present and future climate changes arising from natural, unforced variability or in response to changes in radiative forcing in a multi-model context can be achieved. Moreover, the model performance during historical periods and the quantification of the causes of the spread in future predictions between models can be assessed.

Currently, there are 23 CMIP6-Endorsed MIPs. One of these is the so-called High Resolution Model Intercomparison Project (HighResMIP) (*Haarsma et al.*, 2016) which provides a common protocol for simulations with high horizontal resolutions of 25-50 km that will foster the analysis and understanding of the impact of model resolution and climate change on the simulated climate, especially with respect to small-scale weather phenomena like TCs. Prior to HighResMIP, only a few high-resolution global simulations at climate time scale had been performed (ca. 50 km in the atmosphere, ca. 25 km in the ocean) and without good coordination due to the extreme computational resources needed to perform them, such as *Delworth et al.* (2012) and *Sakamoto et al.* (2012). To assess the robustness of the response to horizontal resolution, a multi-model ensemble with a coordinated set of experiments is needed. It has been shown that the multi-model mean climate forecast skill has often been superior to individual models: In CMIP3 and CMIP5, the mean of seasonal (*Hagedorn et al.*, 2005) and decadal (*Bellucci et al.*, 2015) forecasting proved to be outperforming the individual models. The multi-model ensemble mean is also a necessary procedure to overcome one of the shortcomings of the protocol, which is the lack of multiple ensemble members for each model due to the high computational cost of running at these resolutions. With the availability of computing resources and the design of uniform experiments, CMIP6 HighResMIP is the ideal framework for testing and evaluating the effect of horizontal resolution on TCs in a changing climate.

This is done by running the experiments at two different model resolutions, a standard resolution (**LR**) and a high resolution (**HR**) which will then be compared against each other. The HighResMIP protocol requires all model configurations to be the same for both resolutions so that differences can directly be attributed to the change in resolution rather than to model physics or adjustments of parameterisations (*Haarsma et al.*, 2016).

Furthermore, this study is part of the PRIMAVERA project within the EU Horizon2020 programme, which is a project that follows the CMIP6 HighResMIP protocol to answer the questions mentioned above by carrying out the experiments. It is a collaboration between European partners under the lead of the Met Office and the University of Reading. These partners use different models at different resolutions to achieve the objectives in the CMIP6 framework.

3.2 The CNRM Climate Model

The model used to assess the effect of horizontal resolution and climate change on TC characteristics is the CNRM model, specifically the CNRM-CM6-1 model (*Voldoire et al.*, 2019) which is jointly developed in France by the Centre National de Recherches Météorologiques (**CNRM**) and Cerfacs, a basic and applied research center, specialised in modelling and numerical simulation. The CNRM model has been found to be able to produce TC wind speeds and frequencies close to observations, as discussed in *Roberts et al.* (2020) which motivates its choice for this study. The CNRM-CM6-1 model is a fully coupled atmosphere-ocean general circulation model that includes four main components for the atmosphere, land surface, ocean and sea ice which are coupled by the OASIS3-MCT software (*Craig et al.*, 2017).

The atmospheric component is based on the spectral atmospheric model ARPEGE-Climat version 6.3. It uses a linear triangular truncation T127 for the standard resolution and T359 for the high resolution version of the model (see Tab. 3). These are adopted together with a corresponding reduced Gaussian grid (*Hortal & Simmons*, 1991). The horizontal model resolution is about $1.4° \times 1.4°$ and $0.5° \times 0.5°$ at the equator for LR and HR, respectively. The CNRM-CM6-1 atmospheric component has 91 vertical levels, following a hybrid σ-pressure discretisation, with the highest level set at 0.01 hPa (ca. 80 km) and the boundary layer described with about 15 levels below 1500 m. The dynamical core is based on a two time level semi-Lagrangian numerical integration scheme, and a 15-min time step is used except for the radiative transfer module which is called every hour. More in-depth details and descriptions for the other model components - which are not used for this study and whose fields are prescribed following the HighResMIP protocol (see Sect. 3.3) - are documented in *Voldoire et al.* (2019).

Resolution	Truncation	Nominal resolution	Vertical levels	Analysis grid	Time stepping
LR	T127	250 km	91 (78.4 km)	regridded: $1.4° \times 1.4°$	15 min
HR	T359	50 km	91 (78.4 km)	regridded: $0.5° \times 0.5°$	15 min

Table 3: Summary of the two CNRM model configurations of standard resolution (LR) and enhanced resolution (HR).

3.3 Experiments and Forcings

In the following section, the HighResMIP experiments are described in detail. The experiments are atmosphere-only experiments, which means that the other modules, i.e., land surface, ocean and sea ice, are turned off and their fields will be prescribed by datasets described below. Both of the following experiments are carried out at a standard (LR) and an enhanced (HR) horizontal resolution in order to assess the effects of a changing resolution and climate separately.

3.3.1 Historic Simulation

The *highresSST-present* experiment is a historical forced simulation for the period 1950 through 2014 (called "present"). The atmospheric initial conditions are provided by the ERA-20C reanalysis dataset. While the atmosphere will be free to adjust to perturbations, the ocean and the sea ice components will be prescribed by the HadISST2 dataset (*Titchner & Rayner*, 2014). The HadISST2 dataset provides daily data on a 0.25° grid (ca. 25 km) which is in accordance with the expectations of the protocol to approach horizontal resolutions of up to 25 km. Fine resolutions in the ocean are also necessary to resolve SST gradients associated with ocean fronts and eddies that can significantly influence the state of the atmosphere via air-sea fluxes (*Minobe et al.*, 2008; *O'Reilly et al.*, 2016). However, high-resolution, high-frequent forcings for uncoupled experiments can have some adverse effects: For instance, due to the lack of atmospheric feedback to the ocean, the cooling of the sea surface associated with the upwelling of cold sub-surface waters resulting from divergent surface winds (associated with TCs) cannot be represented (*Emanuel*, 2001). This cooling reduces the exchange of heat between the ocean and the atmosphere and leads to a weakening of the TC (*Cione & Uhlhorn*, 2003). As a consequence, the intensity of TCs - with exception of rapidly moving storms - will likely be biased high in uncoupled experiments (*Cione & Uhlhorn*, 2003).

3.3.2 Future Projection

The *highresSST-future* experiment is a scenario extension of *highresSST-present* into the future and spans the period from 2015 through 2050 (called "future"). The final atmospheric field from *highresSST-present* is used but external forcings such as greenhouse gases, anthropogenic aerosol concentrations, solar forcing etc. (see Sect. 3.3.3) will be prescribed according to the high-end emission scenario of the Shared Socioeconomic Pathways (**SSP**s) SSP5-8.5. Future SST and sea ice forcings follow the methodology of *Mizuta* (2008) which is a blend of the HadISST2-based dataset described above and a climate change signal from CMIP5 RCP8.5 models. Interannual variability is derived from the period 1950-2014. This procedure enables a smooth and continuous transition from the present day into future. Details on this method are shown in *Appendix B* of *Haarsma et al.* (2016). Combining SST data from a CMIP5 RCP8.5 scenario with a CMIP6 SSP greenhouse gas forcing introduces an inconsistency to the simulation, but due to the wide range of climate sensitivity among climate models and the small differences in the model response up to 2050 for different scenarios, this inconsistency is argued to be minor (*Haarsma et al.*, 2016).

3.3.3 Further Common Forcings Fields

Other forcing fields used for greenhouse gas concentrations, aerosol concentrations, land surface properties or solar variability between 1950-2014 are mostly the same as those used in standard CMIP6 historical simulations described in *Eyring et al.* (2016). As mentioned above, future greenhouse gas and anthropogenic aerosol concentrations follow the high-end emission scenario of SSP5-8.5. The aerosol forcing consists of a background concentration climatology to which an anthropogenic time-varying, spatially uniform forcing from the MACv2-SP model (*Stevens et al.*, 2016) is added. In order to make the model forcing as simple and thus as comparable as possible, the land surface properties will be climatological seasonally varying conditions of the leaf area index. Moreover, a non-dynamic vegetation and a constant land use consistent with conditions centred around the year 2000 will be assumed. The atmosphere-land system requires several years of spin-up to reach quasi-equilibrium as is carried out and discussed in *Eyring et al.* (2016). More in-depth details on these common forcing fields can be found in *Haarsma et al.* (2016).

3.4 Cyclone Tracker

The tracker used to detect the formation and propagation of TCs within the model output data is the *BSC Cyclone Tracker* (called "tracker"). It is based on the Geophysical Fluid Dynamics Laboratory Vortex Tracker V3.5b by the National Oceanic and Atmospheric Administration (**NOAA**) (https://dtcenter.org/HurrWRF/users/downloads/Tracker_releases/V3.5b/stand_alone_tracker_UG_v3.5b.pdf). It provides an estimate of the location of the centre of potential TC candidates, their intensity and structure at each 6-hour time step. The tracker uses minima in the mean sea level pressure (**MSLP**) field as the main tracking feature and requires a list of input parameters needed for the tracking of cyclones:

- The MSLP field is required.
- Both horizontal wind speed components u and v at either 850 and 700 hPa or at 500 hPa are needed to estimate the path of the storm. It is possible to use all three pressure levels as input.
- Due to the dynamic connection between wind velocity and absolute vorticity, the tracker can instead use the vorticity of the horizontal wind speed field at the same levels. In this study, the wind speed components u and v are used.
- While the above listed quantities are mandatory to the tracker, the near surface wind speed at 10 m and the geopotential height at 850 and 700 hPa are optional values which can be used to correct the centre of the low, otherwise the centre of the low will be fixed to the minimum MSLP.
- The 400 hPa temperature field is a further optional variable and not mandatory for the detection of storms, but it is used to discriminate between warm-core and cold-core cyclones, i.e., between tropical and extratropical cyclones.

Given all this input data, the tracking process searches the model data for minima in the MSLP, lower than a given threshold parameter, selects suitable candidates and follows their evolution over time. In order to be further classified as a low and not to be rejected, the low requires at least one closed isobar (whose pressure level can be determined by a parameter) around its centre. An isobar is considered closed when the pressure at all eight neighbouring grid boxes increases with respect to the centre of the low pressure. For grid boxes with same pressure values as the centre, the neighbouring grid boxes of that grid box are taken into consideration. If it is not possible to close a single isobar around the centre, the candidate will be discarded. If an isobar can be closed, the process will be repeated until no further isobar can be closed. However, during the tracking process, there are two additional parameters which are constantly checked to evaluate whether the tracking of a potential cyclone should end: the outward surface pressure gradient and the tangential wind speed at 850 hPa (or 500 hPa), both of which need to exceed a certain threshold in order to continue the tracking of a storm. These thresholds are parameters of the tracker and can be adjusted by the user (see Sect. 4 for choice of parameters for this study).

Furthermore, the tracker registers all cyclone candidates which form inside a prescribed domain (see Sect. 3.5.1). Even if the storms leave the domain after first being registered in that domain, the tracker will follow them until one of the tracking criteria is no longer met. Pressure systems that formed before entering the designated tracking domain will only be tracked from their point of entrance into the domain, given they meet the required criteria.

Lastly, the tracker characterises each storm as either tropical or extratropical. Since cores of TCs are relatively warmer than cores of extratropical cyclones, the tracker discriminates between the two by checking the 400 hPa horizontal temperature profile of the candidate low pressure systems. If the maximum temperature value found near the centre of the storm decreases by a threshold parameter in the direction of all eight neighbouring grid boxes within 8°, the low is considered to be of tropical nature. If this criterion is not met, the tracker will still continue to track the storm but it will not be regarded as a TC in the further analyses.

3.5 Definitions and Statistical Tools

3.5.1 Tropical Storms

Following the description by NOAA, the most commonly used time period for the definition of the TC season in the NH is between May/June and the end of November, so that the time period from 1 June to 30 November is adopted for this study (`https://www.nhc.noaa.gov/climo/`). Further, a low pressure system is characterised as a TC if the surface wind speed in the vicinity of the centre exceeds 18 $\mathrm{m\,s^{-1}}$ for a consecutive period of 24 hours. According to these classifications, a potential storm candidate in the model must surpass this wind speed threshold and fulfil the specified warm-core criterion for five consecutive time steps at a 6-hour time resolution. For this study, a potential candidate is not classified as a cyclone if these criteria are not met, even if 20 single data points each overcome the threshold but without a single trace of five connected data points. Conversely, single, non-connected data points will not be omitted if at least one trace of five consecutive data points that all meet the requirements for a TC exists. Together with the outward temperature gradient, the wind speed of each potential storm is evaluated at each time step during the post-processing and the storms are selected according to the above criteria.

Each storm candidate that has been classified as a TC is then allocated to a basin. In case a storm crosses the border between two basins, the storm will be counted in both basins, provided at least one data point that fulfils the criteria is located within that basin. Since this study focuses on TCs in the NH, the three basins considered are as described in Tab. 4 and outlined in Fig. 6 below:

Basin	Longitude	Latitude
Western North Pacific (WNP)	100°E – 180°	0° – 40°N
Eastern North Pacific (ENP)	180° – 100°W 100°W – 90°W 90°W – 85°W 85°W – 70°W	0° – 40°N 0° – 17°N 0° – 15°N 0° – 10°N
North Atlantic (NA)	70°W – 0° 100°W – 90°W 90°W – 85°W 85°W – 70°W	0° – 40°N 17°N – 40°N 15°N – 40°N 10°N – 40°N

Table 4: Description of the spatial extent of the three considered basins in the NH: Western North Pacific (WNP), Eastern North Pacific (ENP) and North Atlantic (NA).

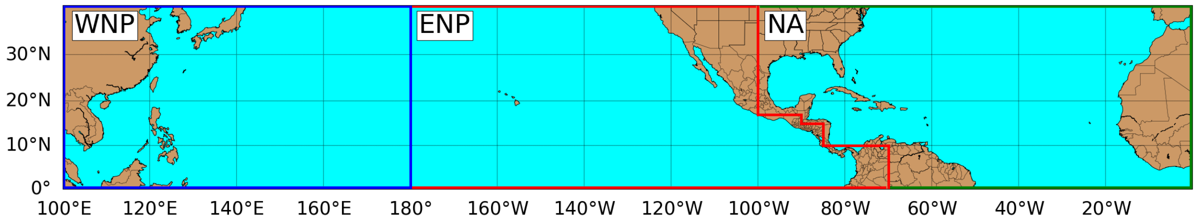

Figure 6: Outline of the three considered basins in the NH: Western North Pacific (WNP), Eastern North Pacific (ENP) and North Atlantic (NA).

3.5.2 Integrated Kinetic Energy (IKE)

Integrated Kinetic Energy (IKE) is an integrated measure to assess a storm's level of energy related to the motion of the air (*Powell & Reinhold*, 2007). Unlike other integrated measures like the Accumulated Cyclone Energy index (ACE) (*Bell et al.*, 2000) or the Power Dissipation Index (PDI) (*Emanuel*, 2005) which only consider the maximum wind speed associated with a storm, IKE also takes into account lower wind speeds and the size of a storm at a given time step. The destructive potential of a storm can much more accurately be assessed when the size of the damaging wind field is considered together with the intensity as pointed out by *Mahendran* (1998). *Kantha* (2006) further highlighted the need to account for storm size when assessing hurricane hazards and acknowledged the relevance of the dynamic wind pressure associated with the wind field. Since IKE is equivalent to the wind pressure it can be a good indicator for the wind loading on structures and strongly influence the caused damage (*Powell & Reinhold*, 2007; *ASCE*, 2016). Furthermore, *Zhai & Jiang* (2014) indicated that using a combination of storm size and maximum wind speed explains a larger portion of the variance in losses caused by a landfalling hurricane than using intensity or size alone. They suggest that economic losses from the landfall of *Hurricane Sandy* (2012) would have been approximately 20 times smaller if its size were comparable to an average sized hurricane. *Wang & Toumi* (2016) demonstrated that the wind structure at landfall is crucial to the destructive potential of hurricanes and that the maximum wind speed is a relatively weaker measure of the damage footprint than the spatially integrated measure, promoting the use of IKE.

Storm surge and waves generated by TCs, too, have been found to be closely connected to IKE as the shear stress of the wind on the ocean surface also scales with kinetic energy (**KE**) (*Powell et al.*, 2003; *Donelan et al.*, 2004). Consequently, the combination of storm size and intensity in the hours and days before landfall is likely to provide a robust estimate of wave and surge destructive potential (*Powell & Reinhold*, 2007; *Irish et al.*, 2008). Thus, IKE provides a metric strongly connected to the physical forces that contribute to damages associated with TCs. This favours the use of IKE over ACE and PDI which both lack information on spatial extent of damaging winds. IKE is defined as the volume integral of the KE per volume unit of the horizontal wind field of a storm:

$$KE = 0.5 \cdot \rho \cdot U^2, \tag{1}$$

with ρ the air density and U the surface wind speed at 10 m height with

$$U = \sqrt{u^2 + v^2}, \tag{2}$$

with u and v the horizontal surface wind speeds in x and y direction. *IKE* is calculated as the area over which the wind field exceeds a certain wind speed threshold, vertically integrated over a uniform 1-metre layer centred around 10 m height:

$$\begin{aligned} IKE &= \int_V KE \ dV = \int_V 0.5 \cdot \rho \cdot \sqrt{u^2+v^2}^2 \ dV \\ &= \int_x \int_y \int_z 0.5 \cdot \rho \cdot (u^2+v^2) \ dz\, dy\, dx = \int_x \int_y 0.5 \cdot \rho \cdot (u^2+v^2) \cdot 1 \text{ m} \ dy\, dx. \end{aligned} \tag{3}$$

In a finite differences approach, the wind speed at each grid point is evaluated. If it surpasses a specific threshold, then that wind speed and the area around that grid point contribute to the estimation of *IKE*. The area is defined by the horizontal resolution of the model Δx and Δy and corrected for the latitude of the grid point ϕ:

$$\int_x \int_y 0.5 \text{ m} \cdot \rho \cdot (u^2+v^2) \ dy\, dx \rightarrow \sum_x \sum_y 0.5 \text{ m} \cdot \rho \cdot (u^2+v^2) \cdot cos(\phi) \cdot \Delta x \cdot \Delta y. \tag{4}$$

The locally dependent air density ρ will be considered spatially uniform in this study. Furthermore, only grid points with wind speeds larger than 18 $\mathrm{m\,s^{-1}}$, which is the threshold required for a storm to be classified as a TC, will contribute to IKE_{TS} (turbulent wind fluctuations are ignored). Also, only grid points within a 2000 km square around the centre of the storm, i.e., 1000 km in all four directions N, E, S and W from the storm centre, are considered for the computation of the *IKE*. The final form of the equation is given below (for simplicity, the value IKE_{TS} will be referred to as IKE):

$$\rho(x, y, z) = \rho = 1\ \mathrm{kg\,m^{-3}}, \tag{5}$$

$$\begin{aligned} IKE_{TS} = IKE &= 0.5\ \mathrm{m} \cdot 1\ \mathrm{kg\,m^{-3}} \cdot \sum_{i=1}^{m}\sum_{j=1}^{n}(u_{i,j}^2 + v_{i,j}^2) \cdot cos(\phi_j) \cdot \Delta x_i \cdot \Delta y_j \\ &= 0.5\ \mathrm{kg\,m^{-2}} \cdot \sum_{i=1}^{m}\sum_{j=1}^{n}(u_{i,j}^2 + v_{i,j}^2) \cdot cos(\phi_j) \cdot \Delta x_i \cdot \Delta y_j, \end{aligned} \tag{6}$$

where i and j are the grid points in the x and y directions within the 2000 km square around the storm centre.

Fig. 7 below shows an example of a surface wind speed field associated with a TC in the WNP. The green dot represents the centre of the storm as identified by the tracker. The yellow isoline displays the 18 $\mathrm{m\,s^{-1}}$ isotach. Thus, all the grid points within this isotach are considered for the computation of the *IKE*. The figure reveals two issues related to the estimation of the *IKE*:

- Since the isotach is created via interpolation between the grid points, it does not align with the rectangular areas around the grid points. This means that some grid points contribute an area too large or too low to the *IKE*. This uncertainty is rather low as these two effects should, to first order, cancel each other out.
- The wind fields of exceptionally large storms may be larger than the 2000 km square, hence why for some storms the area contributing to the *IKE* could be underestimated. Furthermore, extremely small and contracted storms may receive contributions from nearby storm systems which are located within the same 2000 km square. Overall, these effects can be considered to occur with a very low frequency and to be consistent over the entire set of experiments which justifies this methodology.

One further measure of interest is the IKE of a storm, integrated over its entire lifetime. This quantity was introduced by *Misra et al.* (2013) and is called Track Integrated Kinetic

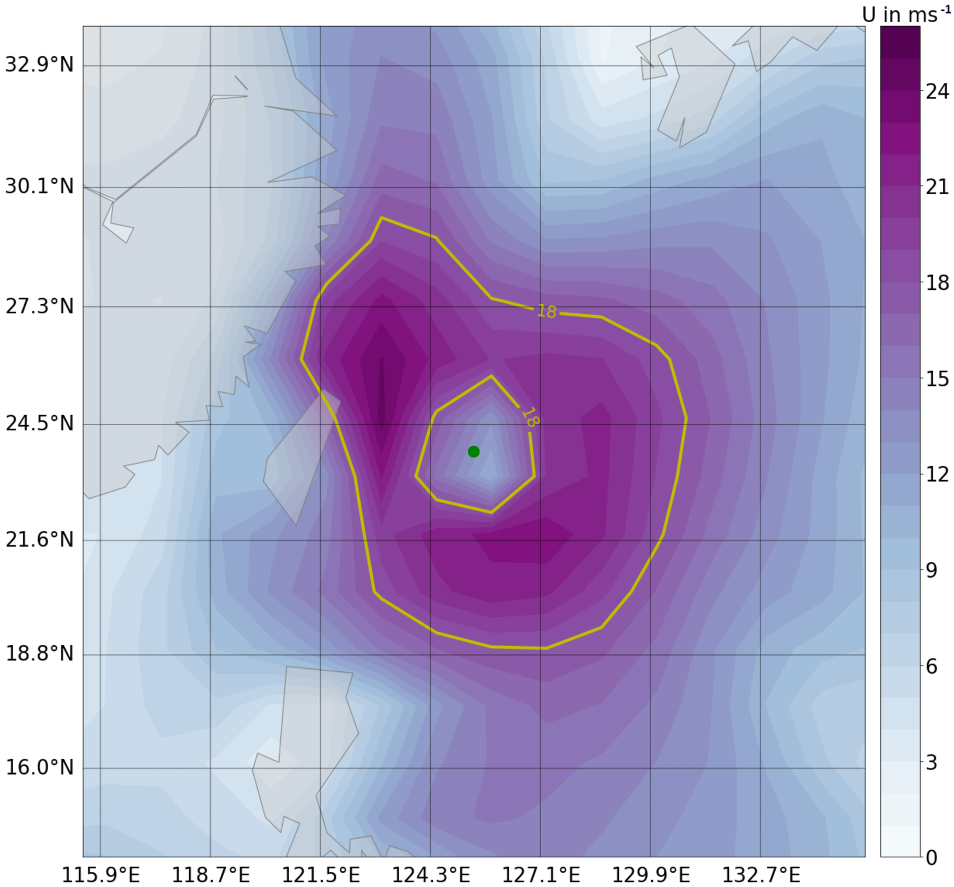

Figure 7: Example wind speed field of a TC in the WNP. Absolute wind speed U is given according to the colour coding. The storm centre as detected by the tracker is represented by the green dot. The 18 $\mathrm{m\,s^{-1}}$ isotach is highlighted in yellow. All the grid points located within the isotach are taken into consideration when calculating IKE.

Energy (**TIKE**) which in a finite differences approach becomes the following (since IKE is evaluated at 6-hour intervals, $\Delta t = 6$ h is cancelled out):

$$TIKE = \int_t IKE \ dt \rightarrow \sum_{k=1}^{o} (IKE)_k \cdot \Delta t_k = \sum_{k=1}^{o} (IKE)_k, \tag{7}$$

where t represents the points in time and k the observed time steps at which the storm fulfils the tropical storm criteria. Summing up the $TIKE$ of all storms of a season during a given year yields the *seasonal* $TIKE$, which serves as a measure for comparison of TC activity between different years:

$$seasonal \ TIKE = \sum_{l=1}^{p} (TIKE)_l = \sum_{l=1}^{p} \left(\sum_{k=1}^{o} (IKE)_k \right)_l , \tag{8}$$

where l represents all the storms during a storm season from June through November over which the summation is carried out.

3.5.3 PDO and AMO Indices

The PDO is a decadal climate oscillation in the Pacific Ocean. It is often described as a long-lived El Niño-like pattern of Pacific and North American climate variability, strongly driven by fluctuations in SST (*Zhang et al.*, 1997; *Mantua et al.*, 1997). Extreme phases of the PDO are classified as being warm or cool and they are defined by SST anomalies in the northeast and tropical Pacific Ocean. Anomalously low SSTs in the interior North Pacific and above-average SSTs along the Pacific coast characterise a positive PDO phase, reversed patterns a negative phase (*Mantua & Hare*, 2002). The PDO index is a measure to quantify the state of the PDO, using spatially averaged SST anomalies in the Pacific, north of 20°N (*Mantua & Hare*, 2002). This study uses the NCEI PDO index which is based on NOAA's extended reconstruction of SSTs (ERSST Version 4). It is constructed by regressing the ERSST anomalies against the Mantua PDO index (*Mantua & Hare*, 2002) for their overlap period, to compute a PDO regression map for the North Pacific ERSST anomalies. The ERSST anomalies are then projected onto that map to compute the NCEI index (`https://www.ncdc.noaa.gov/teleconnections/pdo/`).

The AMO is a similar climate oscillation as the PDO but operating on multidecadal timescales (60-80 years) in the Atlantic Ocean (*Trenberth et al.*, 2019). It has been found to impact Atlantic hurricane activity, North American and European summer climate, mean surface temperature in the NH and Arctic sea-ice anomalies (*Trenberth et al.*, 2019). Analogous to the PDO index, the AMO index is typically defined as the spatial average of SST anomalies in the NH between 0° and 80°N (*Trenberth et al.*, 2019). The AMO index used in this study is the smoothed version provided by NOAA, derived from the Kaplan SST dataset and is based on a spatial average of NA SST anomalies between 0° and 70°N (`https://psl.noaa.gov/data/timeseries/AMO/`).

3.5.4 Linear Regression and Pearson's Correlation Coefficient

The simple linear regression is a statistical method to model the linear relationship between two data series x and y of n data points $(x_i,\ y_i)$. It is a model in which one variable x is used as a linear predictor for the second variable y by using two parameters α and β, the intercept and slope (sometimes referred to as *trend*) of the regression line:

$$y_i^\circ = \alpha^\circ + \beta^\circ \cdot x_i. \tag{9}$$

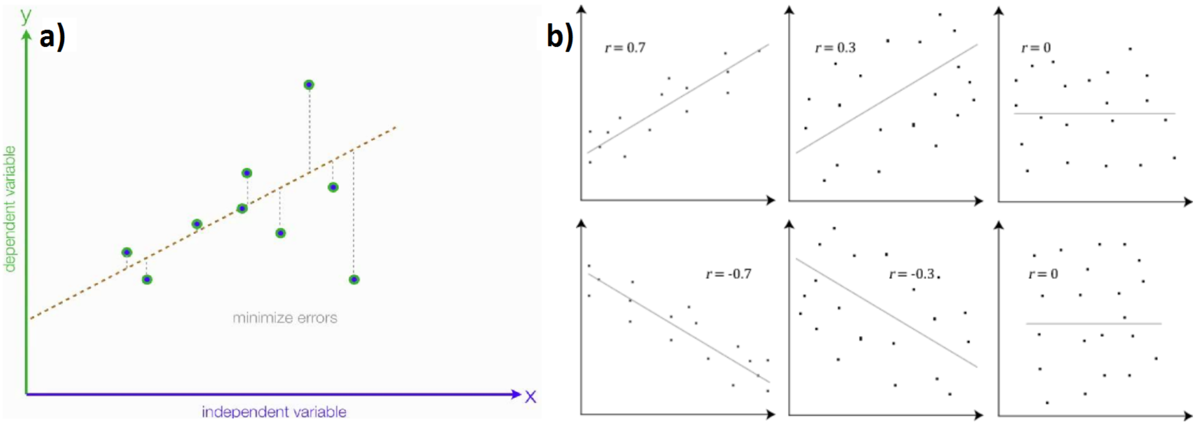

Figure 8: (a) Schematic of fitting a linear function to the available data points. Minimising the errors between the modelled and the actual data yields the best-fit model (https://i.ytimg.com/vi/zPG4NjIkCjc/maxresdefault.jpg). (b) Different linear relationships between two variables and their respective correlation coefficients (https://commons.wikimedia.org/wiki/File:Pearson_Correlation_Coefficient_and_associated_scatterplots.png.)

The estimators α° and β° for the best-fit linear model are calculated using a least-squares approach where the sum of the squared differences between the actual data point y_i and the predicted data point y_i° is minimised (Fig. 8a):

$$minimise : \sum_{i=1}^{n}(y_i - y_i^\circ)^2 = \sum_{i=1}^{n}(y_i - (\alpha^\circ + \beta^\circ \cdot x_i))^2, \tag{10}$$

$$\beta^\circ = \frac{\sum_{i=1}^{n}(x_i - \bar{x}) \cdot (y_i - \bar{y})}{\sum_{i=1}^{n}(x_i - \bar{x})^2}, \tag{11}$$

$$\alpha^\circ = \bar{y} - \beta^\circ \cdot \bar{x}, \tag{12}$$

where $\bar{x}$ and $\bar{y}$ are the mean values of x and y:

$$\bar{x} = \frac{1}{n} \cdot \sum_{i=1}^{n} x_i, \tag{13}$$

$$\bar{y} = \frac{1}{n} \cdot \sum_{i=1}^{n} y_i. \tag{14}$$

The correlation coefficient $\rho_{x,y}$ between the two data series x and y quantifies their relationship to one another. The most commonly used coefficient for linear relationships is Pearson's correlation coefficient (referred to as *correlation*). It gives insight into how adequate a linear model is in representing the link between the variables. It is a scaled

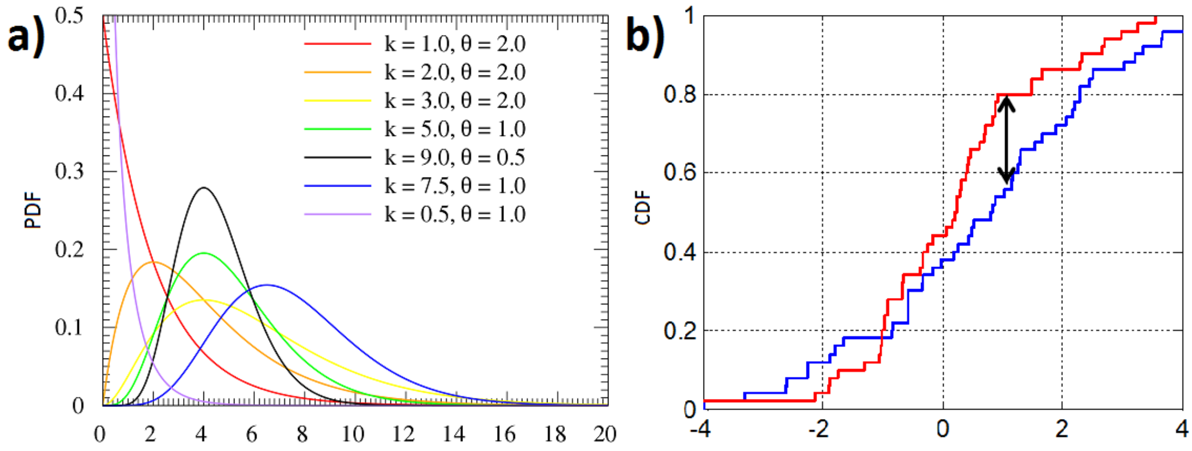

Figure 9: (a) Gamma distributions for various combinations of shape parameter k and scale parameter θ (https://commons.wikimedia.org/wiki/File:Gamma_distribution_pdf.svg). (b) Visualisation of the KS statistics $D_{n,m}$ which is based on the maximum difference between two CDFs (https://commons.wikimedia.org/wiki/File:KS2_Example.png).

measure bounded between 1 and -1. The closer the coefficient to 0, the weaker the linear relationship is. Conversely, the closer it is to 1 or -1, the stronger the linear relationship is. While values above 0 represent positive relationships between x and y, values less than 0 characterise negative relationships (compare Fig. 8b). Pearson's correlation coefficient is defined such as:

$$\rho_{x,y} = \frac{\sum_{i=1}^{n}(x_i - \bar{x}) \cdot (y_i - \bar{y})}{\sqrt{\sum_{i=1}^{n}(x_i - \bar{x})^2 \cdot (y_i - \bar{y})^2}}. \tag{15}$$

3.5.5 Gamma Distribution and Kolmogorov-Smirnov Test

The Gamma distribution is a statistical, continuous distribution and a useful tool to model the distribution of atmospheric quantities as many of them are bounded at the lower end and distinctly asymmetrical. For instance, wind speed and precipitation distributions are commonly described using the Gamma distribution (*Morgan et al.*, 2011; *Liang et al.*, 2012). The Gamma distribution is defined over the interval $[0, \infty)$ and parameterised by a shape parameter k and a scale parameter θ (examples given in Fig. 9a). Its probability density function f (**PDF**) is as follows:

$$f(x; k, \theta) = \frac{x^{k-1} \cdot e^{-x/\theta}}{\Gamma(k) \cdot \theta^k}, \tag{16}$$

where $\Gamma(k)$ is the Gamma function

$$\Gamma(k) = (k-1)!. \tag{17}$$

It is possible to account for the lower bound of the modelled process by shifting it along the x-axis with a location parameter μ which, eventually, influences the interval over which the distribution is defined as $[\mu, \infty)$:

$$f(x; k, \theta, \mu) = \frac{(x-\mu)^{k-1} \cdot e^{-(x-\mu)/\theta}}{\Gamma(k) \cdot \theta^k}. \tag{18}$$

The Kolmogorov-Smirnov (**KS**) test is a non-parametric test that can be used as a goodness-of-fit test to compare two samples to evaluate whether or not these originate from a common distribution (*Lopes et al.*, 2007). It assumes a null hypothesis under which both samples come from the same, continuous distribution. The KS statistics $D_{n,m}$ evaluates the local difference between both cumulative density functions F_1 and F_2 (**CDF**s) and calculates the maximum difference (Fig. 9b):

$$D_{n,m} = sup_x |F_{1,n}(x) - F_{2,m}(x)|, \tag{19}$$

where sup_x is the supremum function and n and m are the sizes of the respective samples. If, at any point, a certain critical value is exceeded, the null hypothesis is rejected and the samples are considered to originate from different distributions. The critical value to be exceeded in order to reject the null hypothesis depends on the size of the samples and the desired significance level α. For a two-sided KS test with a significance level of $\alpha = 5\%$, the criterion becomes:

$$D_{n,m} > 1.36 \cdot \sqrt{\frac{n+m}{n \cdot m}} \tag{20}$$

4 Tuning the Tracker

Before tracking the storms, a reasonable set of tracking parameters needs to be established that will be used uniformly for the experiments. This preliminary step will also provide an opportunity to estimate the sensitivity of the results to these parameters and also detect potential errors that can occur and which could impact the results.

First, it has to be noted that it is possible to set the domain and the time period over which to track the storms. This allows to speed up the tracking procedure by removing areas and seasons either for which TCs are not expected to form in or which are outside the scope of this study. Similarly, it is a useful feature to exploit performing small tests: By limiting the domain to a single month and to only a part of a basin, one can speed up the tracking considerably. Besides the domain size and the time period, a set of five different parameters can be adjusted prior to the tracking. Modifying these parameters will impact, to various degrees, the cyclones detected by the tracker. These parameters are:

- The minimum MSLP a low has to reach in order to be registered as a potential storm candidate;
- The threshold value of the 400 hPa horizontal temperature decrease in order to be classified as a tropical or extratropical cylone;
- The outward surface pressure gradient that needs to be maintained in order to be classified as a storm;
- The minimum azimuthally-averaged cyclonic tangential wind speed at 850 hPa (or 500 hPa) that needs to be maintained in order to be classified as a storm;
- The surface pressure interval between the storm centre and the environment, i.e., the increase in surface pressure needed between the centre and each isobar the tracker tries to close.

The tracker comes with a standard value for each parameter. Depending on the objective of the performed study, the user can choose to modify the parameters. For example, it is useful to reduce the MSLP parameter when examining the Indian Ocean or West Pacific where MSLPs are generally lower due to higher SSTs. To estimate the sensitivity of the results to these parameters and to determine whether they should be modified, a series of tests is performed. To illustrate the impact that these parameters can have on the results, two extreme cases for each parameter are presented: one which is more permissive and one which is more stringent. These assessments are carried out using test cases that are assumed to be representative of the typical TCs simulated by the model. After assessing the tracker's performance, the final set of parameters is chosen.

The first parameter that is tested is the minimum MSLP threshold, and the tracking response to three different values (1000 hPa, 1010 hPa (standard) and 1020 hPa) is examined. A test case confirms the expected outcome that the lower threshold of 1000 hPa generates significantly fewer storms (-44%) than the standard value, while the more relaxed condition generates slightly more storms (+7%). Giving further confidence in the integrity of this tracker feature is the fact that all storms, that were recognised by the lower threshold, were also recognised by the higher thresholds. Considering the large difference in registered storms between the 1000 hPa and 1010 hPa threshold and the increase in computational time needed to perform the experiment at a threshold of 1020 hPa, the standard parameter value of 1010 hPa is maintained for the following analyses.

Secondly, the parameter for the warm-core criterion is assessed. In contrast to the minimum MSLP check, the warm-core check does not influence the number of storms detected, it only serves as a classification tool. Three different values for the required outward temperature decrease are evaluated: 0.5°C, 1.0°C (standard) and 2.0°C. In general, this tool works well for all three values. Fig. 10 shows the 400 hPa temperature field associated with an example TC in the WNP. The local maximum temperature (see colour coding) of the model output data is found close to the estimated vortex centre by the tracker (green dot). The three isotherms represent the three different temperature decrease criteria (0.5°C, 1.0°C, 2.0°C) relative to the maximum temperature. The figure reveals that all three considered isolines are closed within 8° of the maximum temperature, indicating that this storm should be classified as warm-core, regardless of the threshold chosen. The visual output is confirmed by the tracker which characterises this storm as warm-core for each of the three cases. If one of the isotherms had not been closed, the tracker would have classified this storm as cold-core (extratropical). Further analyses showed that, overall, the classification tool is reliable, although there are cases for which the visual output of the (closed) isolines and the tracker output do not match each other (not shown). However, this issue mainly arises for storms of weaker magnitude and it is expected to have little impact on the final results since these weak storms are filtered out due to the wind speed threshold for TCs in the post-processing. Due to the successful testing of all three parameters, the recommended standard value of 1.0°C is maintained.

The standard outward surface pressure gradient value of 0.010 $\mathrm{hPa\,km^{-1}}$ is assessed and compared to the results given by a reduction to 0.005 $\mathrm{hPa\,km^{-1}}$ and by increasing it to 0.020 $\mathrm{hPa\,km^{-1}}$. For all test cases the total storm count remained constant. The lack of change in storm counts appears surprising but coincides with the finding of the tracker's developer who, too, found that changing this parameter does not have an impact on the ending of the tracking. In all examined cases, the tracking was never terminated because of the pressure gradient. Similar to the outward surface pressure gradient, the 850 hPa wind speed is evaluated at its standard value of 5 $\mathrm{m\,s^{-1}}$, at a

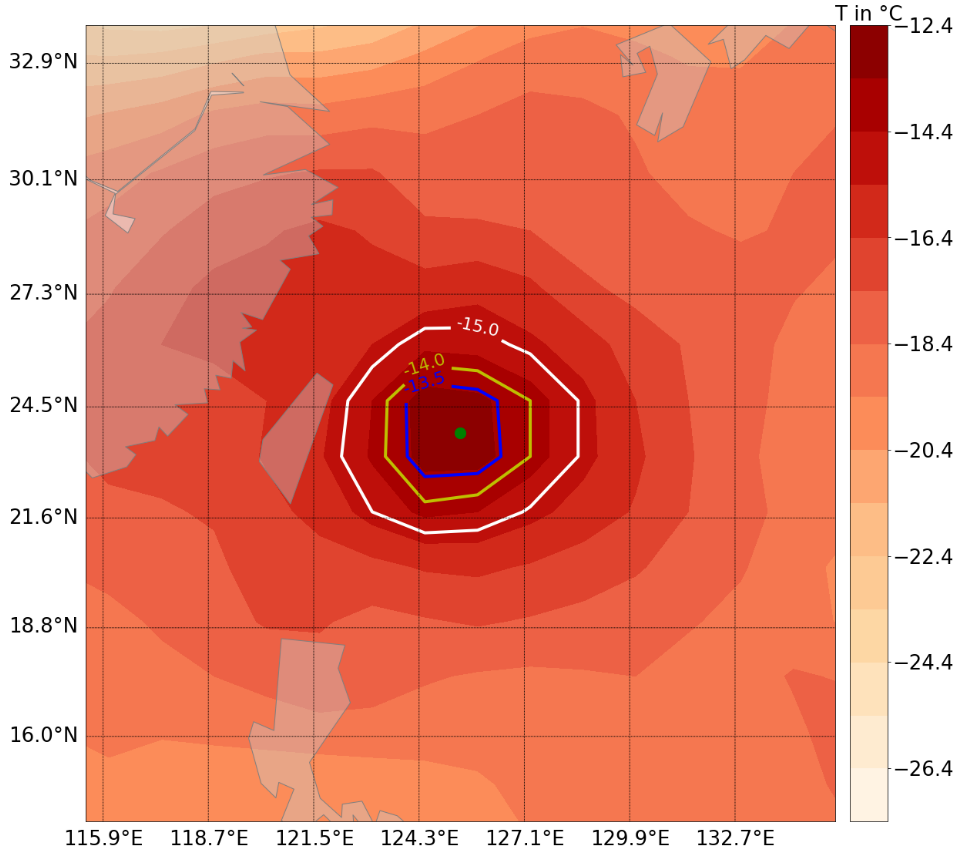

Figure 10: 400 hPa temperature field associated with an example TC in the WNP. The storm centre as recognised by the tracker is shown by the green dot. The isotherms associated with the three different tested temperature decrease thresholds of 0.5°C, 1.0°C and 2.0°C relative to the maximum temperature are highlighted in blue, yellow and white, respectively.

reduced value of 2 $\mathrm{m\,s^{-1}}$ and at an increased value of 7 $\mathrm{m\,s^{-1}}$. All things being equal, it would be expected that a higher wind speed threshold leads to a lower storm count. In general, this is what has been observed, although there were exceptional cases in which a storm would be identified with the higher but not the lower threshold. A possible reason for this might be the interpolation scheme used in the tracker code that could possibly cause the tracker problems closing isolines. This could result in wind speed conditions which lead to the difference in storm registrations. As for the warm-core check, the issue of storms being detected by higher thresholds but not by lower thresholds arises relatively rarely and thus the standard value of 5 $\mathrm{m\,s^{-1}}$ for the 850 hPa wind speed is maintained to exclude the weakest storms.

The last parameter requiring evaluation is the surface pressure interval between the pressure of the centre of the storm and the first closed isobar. If one isobar has successfully been closed, this value determines the pressure interval between this isobar and the next potentially closed isobar. At the same time, a higher interval value should exclude storms with a lower pressure difference between the centre and the environment.

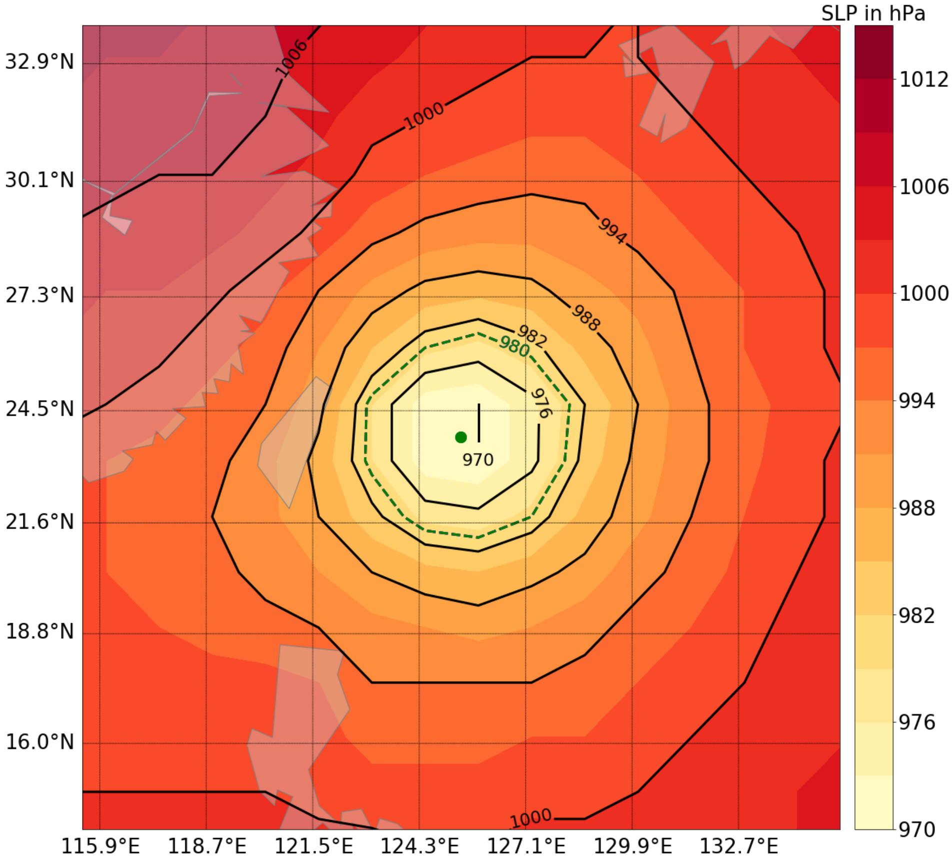

Figure 11: MSLP field and related isobars associated with an example TC in the WNP. The storm centre as recognised by the tracker is shown by the green dot. The last closed isobar as detected by the tracker (for all three different tested surface pressure interval values of 0.5 hPa, 1.0 hPa and 2.0 hPa) is highlighted in green.

In general, this result can be seen in test cases where changing the standard parameter value from 1.0 hPa to 0.5 hPa and 2.0 hPa results in higher and lower storm counts, respectively. Unfortunately, in almost all cases, the tracker output of the last closed isobar does not coincide with the model data. For example, in Fig. 11, the last closed isobar with respect to the 0.5 hPa, 1.0 hPa and 2.0 hPa interval as identified by the tracker is highlighted in green. It is evident that this 980 hPa isobar is not the last closed isobar around the storm centre. It is suspected that this issue arises due to the interpolation scheme inherent to the tracking procedure and despite many attempts, identifying the exact cause of the issue was unsuccessful, let alone solving it. This could potentially have an impact on the final output, but the nature of that impact is difficult to evaluate. Accordingly, the default value for this parameter, i.e., 1 hPa, is chosen.

Besides the five parameters which can be adjusted, it is informative to investigate whether the tracker performs as expected at different model resolutions. Comparing the HR integration against LR in a test case, yields an increase in storm counts of approximately 60% which matches the expectations. In addition, the minimum MSLP found in

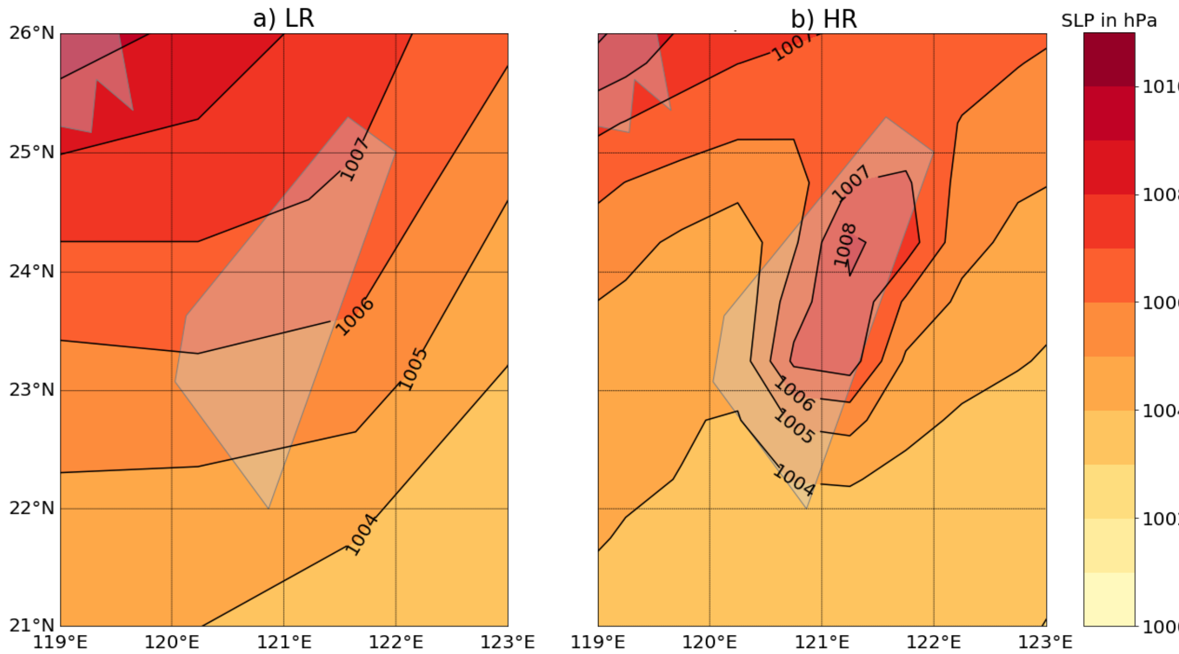

Figure 12: Average MSLP in September for a test case over Taiwan in the WNP for LR (a) and HR (b). The increased resolution enables the representation of topographic features over small land masses which leads to an interaction with the local MSLP.

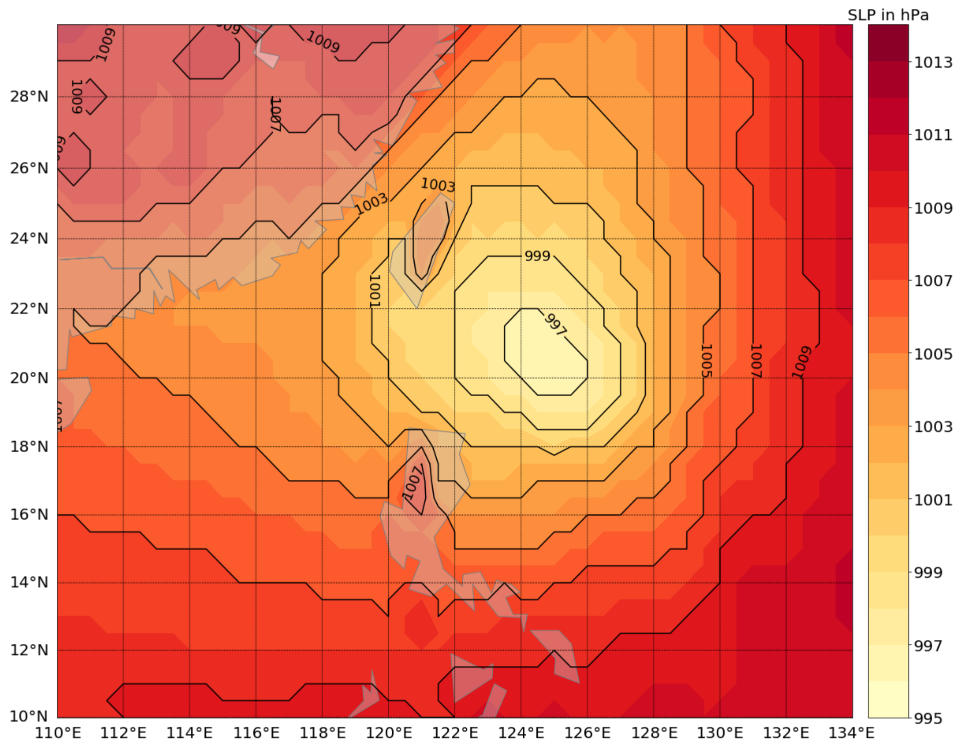

Figure 13: MSLP field and isobars associated with an example TC in the WNP in a HR test experiment. The positive MSLP anomaly over Taiwan distorts the pressure field of the nearby cyclone.

all detected TCs decreased from 934 hPa in LR to 912 hPa in HR. The maximum wind speed registered for TCs showed an increase from 30 $\mathrm{m\,s^{-1}}$ to 56 $\mathrm{m\,s^{-1}}$, also agreeing with the notion of lower pressures and higher winds at finer resolutions. Despite these positive findings, the tracker seemed to fail to continuously track some storms in HR relative to LR. Although those storms were detected at each time step, these individual data points were not connected and not considered as one continuous storm but registered as several single storms so that they had to be pieced together in order to create a continuous storm track. Especially strongly impacted areas include small islands of high topography like Taiwan and Hawaii. The reason for this appears to be the increased horizontal resolution and representation of these small landmasses which are not properly resolved in LR. Eventually, the topography creates a positive horizontal anomaly in MSLP over these regions as can be seen in Fig. 12 (example for Taiwan in the WNP). The anomaly is persistent over the entire storm season and interacts with approaching cyclones, leading to high pressure anomalies within the storm systems. These anomalies arise from the use of MSLP which in case of high orography is a virtual value which appears to interfere with the tracking of nearby storms. An example is provided in Fig. 13 where the high pressure anomaly over Taiwan distorts the pressure field of a nearby cyclone (see interaction of 1003 hPa isobar with 1001 hPa isobar). It is suggested that this distortion leads to problems with closing the isobars related to the cyclone (as mentioned above) and finally ends the tracking of the storm. Regions of similar characteristics like Hawaii, the Philippines and parts of the Caribbean also suffer from these topographical issues in HR which can introduce uncertainties to the analyses.

5 TCs in the CNRM Climate Model

In this section, the climate model's TC activity is shown to first provide an overview of the number of storms, their location, intensity and obviously, IKE. Subsequently, the findings for the effects of model resolution and a changing climate on IKE characteristics are presented, individually for the Western North Pacific (WNP), the Eastern North Pacific (ENP), the North Atlantic (NA) and in combination ("NH").

5.1 Storm Frequency, Intensity and Track Density

The frequency of TCs, their intensity and global distribution are key factors to take into consideration when characterising a model's ability to reproduce observed TC activity. Fig. 14 shows the tracks of all the simulated TCs. Their maximum lifetime intensity, based on the SSHWS, is given by the colour-coding. First, it is evident that in all experiments the WNP is the most active basin, followed by the NA and the ENP. This differs from the observed climatology presented in Fig. 4 in which the ENP is characterised by higher TC activity than the NA. A possible reason for the underestimation of registered TCs might be the North American topography: As pointed out by *Zehnder* (1991) and *Mozer & Zehnder* (1996), the Sierra Madre plays an important role in providing vorticity required to initiate TCs. These orographic features may not be well represented in the model and result in a low number of TCs in the ENP.

Secondly, Fig. 14 reveals that experiments with a finer model resolution are able to generate more TCs than their coarse resolution counterparts, but also, that TCs in all basins remain biased low with respect to the observed climatology (WNP: 25 storms per year, ENP: 15 storms per year, NA: 13 storms per year). This result is expected and aligns with the findings of *Chauvin et al.* (2019) and *Roberts et al.* (2020) who also found that a refinement of the CNRM model resolution positively impacts TC frequency which, nevertheless, is still biased low with respect to observations. Particularly, the ENP and the NA benefit from the increase in resolution where the storm counts per year for the period 1950-2050 rise from 0.4 to 3.7 (ENP) and from 1.5 to 9.3 (NA). The WNP, too, experiences an increase in storm numbers from 8.4 to 16.6, however, this increase is relatively not as large as the increase seen in the other two basins.

Thirdly, an increase in storm intensity with resolution can also be noticed in all basins. Whereas the highest storm intensity in the LR experiment is found to be category 1, TCs of categories 2-5 could be generated in the HR experiment, as can be seen by the orange, red, purple and black tracks (Fig. 14b, d). This finding is also consistent with the previous studies of *Chauvin et al.* (2019) and *Roberts et al.* (2020) who pointed out that the enhanced resolutions in the CNRM model were able to generate TCs of the highest categories, producing more realistic results.

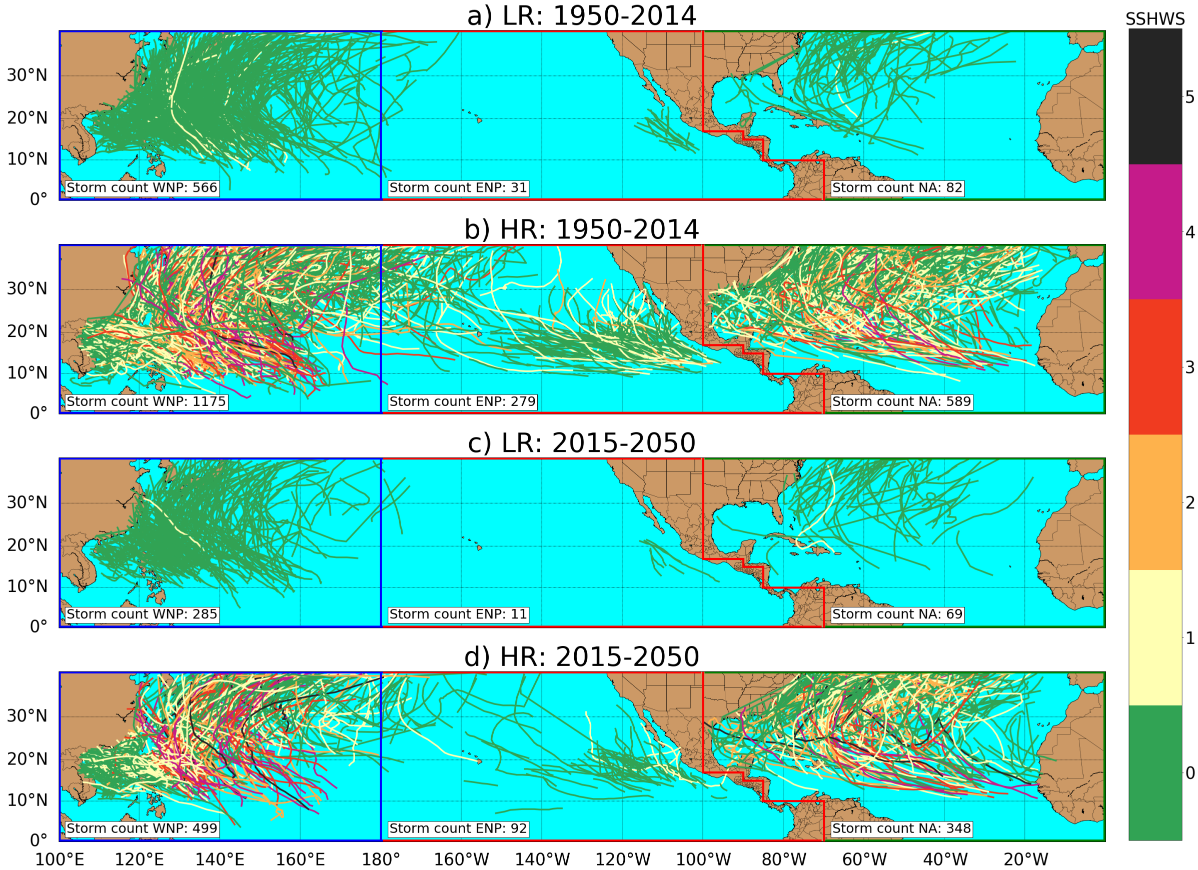

Figure 14: Storm tracks for LR present (a), HR present (b), LR future (c) and HR future (d). Every storm is colour-coded according to its maximum lifetime intensity with respect to the SSHWS (tropical storms are counted as category 0). The total storm count for the entire period for each basin is shown in the boxes.

Comparing the present period (1950-2014) and the future period (2015-2050) against each other reveals that the global annual frequency slightly declines for both resolutions: In LR, the value drops from 10.5 to 10.1 whereas it decreases more from 31.5 to 26.2 in the HR integration (not checked for statistical significance). The figure also displays differences in the frequency response between the individual basins. Both basins in the North Pacific are characterised by a decrease in storm activity as opposed to the NA which shows increasing activity in the future. However, although a decrease in global future TC activity has been found in other studies (*Knutson et al.*, 2019), it has to be kept in mind that this study is based on atmospheric-only simulations with prescribed SSTs and one model simulation only which adds uncertainty to projections of future changes so that interpreting the presented numbers must be done with caution.

Next, it is evaluated whether a change in intensity between the present and future period can be detected. To provide two examples, the percentages of storms in SSHWS categories 0 and 4 relative to the overall storm count are evaluated and reveal that there is only little change between both periods: The LR integration yields values of 98%

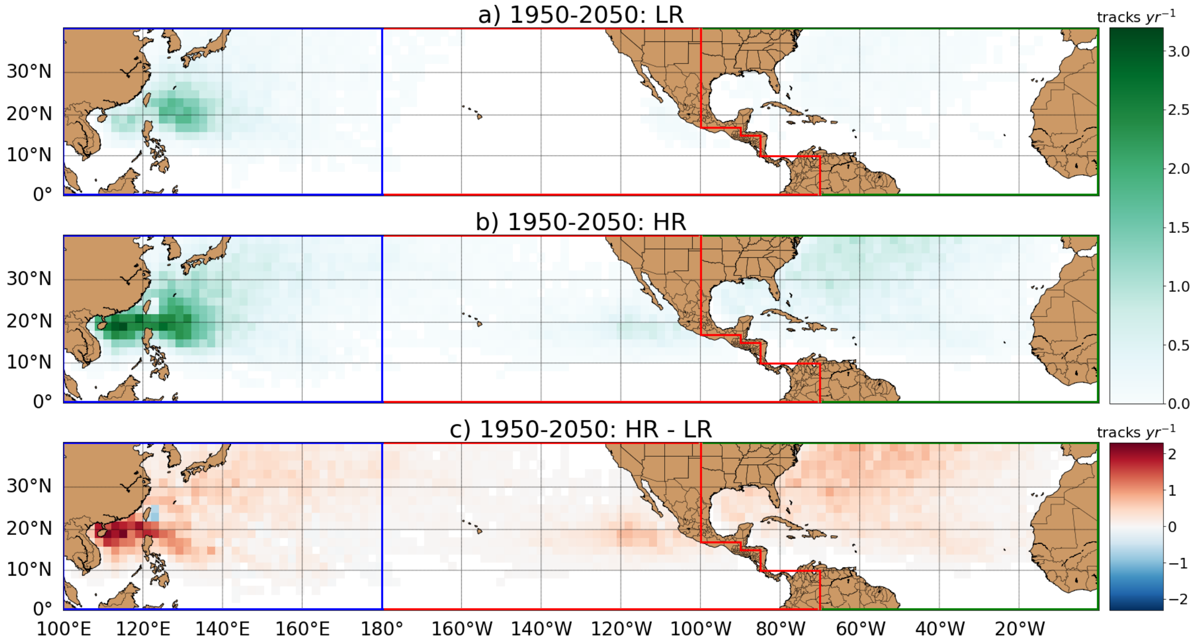

Figure 15: Track distribution per year in the NH per $2° \times 2°$ grid cells from 1950-2050 for (a) LR and (b) HR, (c) difference between HR and LR. All storm transits in the respective grid boxes were counted and averaged over time.

(present) and 99% (future) for category 0 and no storms of category 4 in both time periods. HR shows percentages of 59.3% versus 62.3% and 3.3% versus 3.9% for category 0 and 4, respectively. Considering all categories (not shown), the numbers indicate a slight increase in storms of categories 0 and 3-5 at expense of category 1 and 2 storms. Although no statistical test for significance has been applied, the low differences suggest no clear trend toward more or less intense storms in the future unlike presented in the study of *Knutson et al.* (2019).

A more precise picture about the global storm distribution can be obtained from Fig. 15 which shows storm occurrences per $2° \times 2°$ grid box per year from 1950-2050. As already anticipated from Fig. 14, the majority of storm tracks is registered in the WNP. Since the signal in the ENP and NA is very weak compared to that in the WNP, Fig. 25-Fig. 27 in the Appendix provide a close-up view of the individual basins. These confirm the increase in storms from the LR experiment to HR for all three basins. This finding disagrees with the result of *Roberts et al.* (2020), who - despite concluding an overall increase in global TC frequency from LR to HR - found increases as well as decreases in all individual basins using the CNRM model. A possible explanation for this could be the use of two other tracking mechanisms (*TRACK* and *Tempest Extremes*) which might lead to differences in storm recognition: While *TRACK* (*Hodges et al.*, 2017) uses the vorticity average over 850 hPa, 700 hPa and 600 hPa as tracking feature, *Tempest Extremes* (*Ullrich & Zarzycki*, 2017; *Zarzycki & Ullrich*, 2017) also uses minima in MSLP as tracking feature but in addition, use differences in geopotential height between 500 hPa and 250 hPa. Further consequences of the enhancement in resolution include:

- A shift in the WNP maximum storm frequency toward the South China Sea, between Hong Kong, Taiwan and the Philippines.
- No detected storms around the north eastern coast of Taiwan in the HR experiments, leading to negative signals in the figures for the difference. This behaviour is due to a bug in the tracker and was linked to the topography, as discussed in Sect. 4.
- An increase in ENP storm activity, with its maximum centred off the coast of Mexico.
- An increase in storm activity throughout almost the entire NA basin, with its maximum between 60°W and 70°W.

5.2 Impact of Model Resolution on Simulated IKE

After providing an overview of the TC activity, the IKE will be assessed. Here, IKE is defined as the integration of the energy, i.e., intensity and size, of the wind field above the 18 $\mathrm{m\,s^{-1}}$ wind speed threshold. With the demonstrated increase in maximum storm intensity from LR to HR, the question arises whether a shift in probability toward storms of higher maximum lifetime IKE can be expected as well. In order to address this question, first the spatial distribution of maximum lifetime IKE values between the two resolutions is evaluated. Due to the lack of sufficient storm numbers to perform robust statistical methods in the ENP, this basin is not analysed in isolation but in combination with the WNP and the NA.

Fig. 16 provides an overview of the basin wide maximum lifetime IKE per storm per $2° \times 2°$ grid cells for the period 1950-2050. This figure has to be considered in combination with the track densities in Fig. 15, as every $2° \times 2°$ box is characterised by a different amount of storm transits which influences the IKE value per storm. A close-up view of the individual WNP and NA basins can be found in Fig. 28 and Fig. 29 in the Appendix. The difference in response in the WNP (Fig. 16c) is mixed throughout the basin with an emerging tripole pattern with centres of action located in the South China Sea, east of Japan and east of Taiwan/south of Japan. This finding suggests that an increase in resolution shifts the maximum IKE content of storms toward the Chinese and Japanese coasts whereas storms are less energetic off the east coast of Taiwan. Taking into consideration the increased track density in the South China Sea (Fig. 15c), this area is characterised by more frequent and more energetic storms when enhancing the model resolution.

In the NA, the difference between the resolutions is positive north of 20°N, with its maximum increase just north of 30°N and between 40°W-60°W. The signal is very

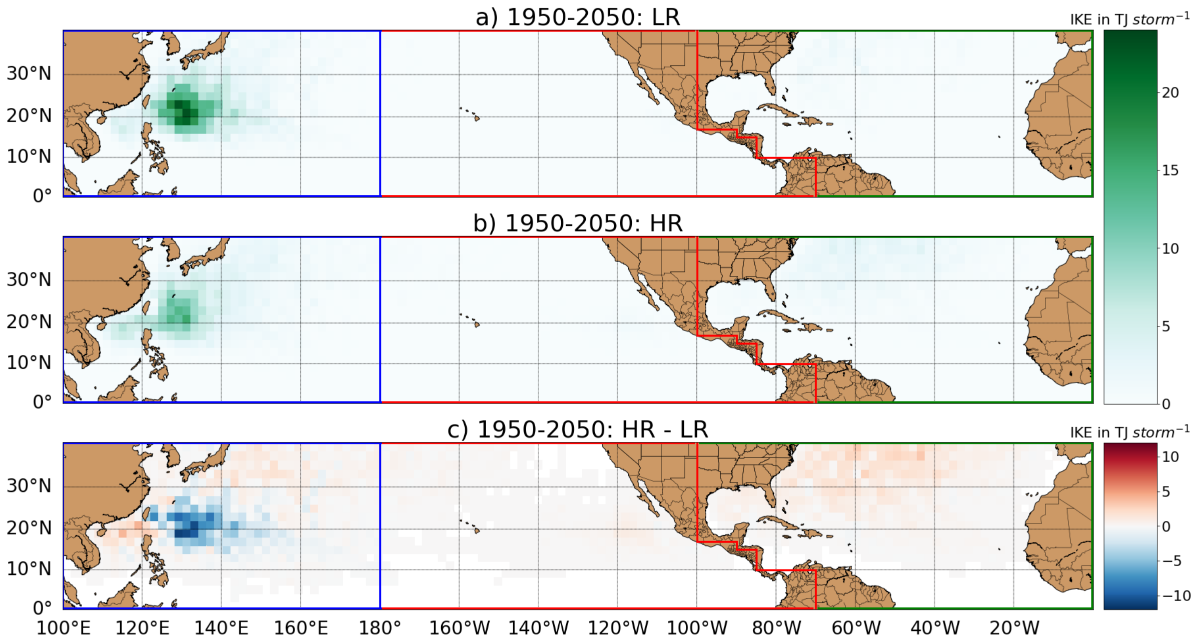

Figure 16: Maximum lifetime IKE distribution per storm in the NH per 2° × 2° grid cells for (a) LR and (b) HR from 1950-2050, (c) difference between HR and LR. The IKE associated with all storm transits in the respective grid boxes was summed up and then averaged over all those storm transits.

similar to the change in track density as seen in Fig. 15, so that more frequent and energetic storms are to be expected in the entire NA in HR. This basin wide increase in maximum IKE may be caused by the overall better representation of storms in the NA compared to LR, as was already emphasised by the difference in total storm occurrences in Fig. 14. Overall, the results suggest differences in the basin wide spatial distribution of the IKE response to increased resolution: positive throughout the NA and a tripole pattern in WNP.

Next, the probability density (**PD**) of storms to reach specific maximum lifetime IKE ranges in both resolutions from 1950 through 2050 is evaluated. To get a hemispheric and a regional insight, the NH as a whole and the WNP and the NA are analysed individually. The PDs between LR and HR in the NH (Fig. 17a) are similar, particularly in the IKE range above 200 TJ. Differences are present in the low-energy range with HR producing proportionally more of the weakest storms (0-25 TJ) and LR generating more storms in the band from 25-150 TJ. To receive a more clear and quantitative assessment, best-fit Gamma distributions have been added to the PDs of both resolutions (orange and grey). These reveal that there is a pronounced difference in probability for low-energetic storms, especially in the range between 0 and 150 TJ, verifying an increase in the weakest storms from LR to HR and a decrease in the band from 25-150 TJ. A KS test confirms that the two fitted distributions are significantly different from each other at the 5% significance level. With the decrease in low-energy storms (except for the weakest

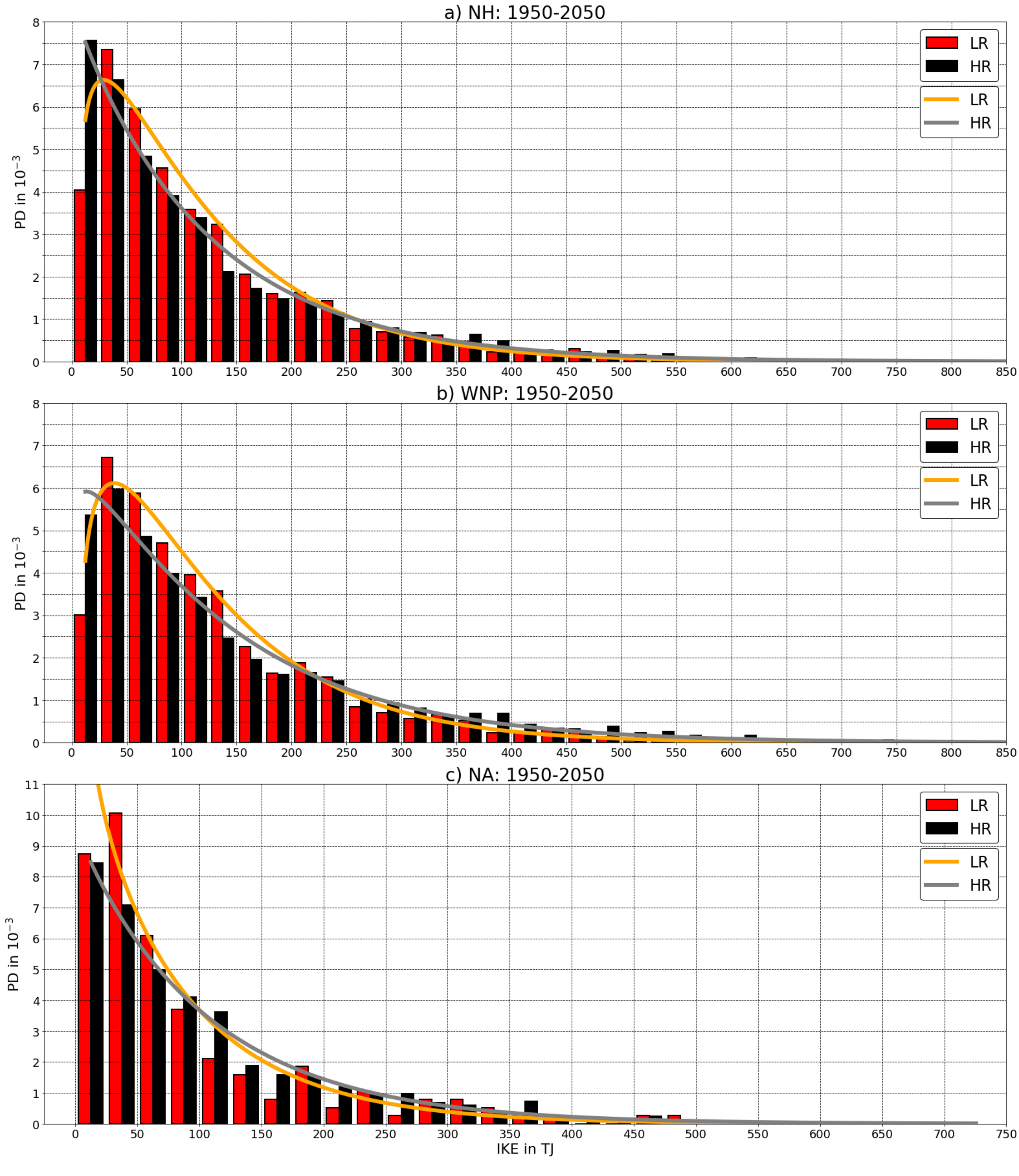

Figure 17: Comparison of PDs for all storms from 1950-2050 in the respective ocean basins to reach specific lifetime maximum IKE. Bin sizes are 25 TJ, starting at 0 TJ. Red and black bars are for LR and HR, respectively. (a) represents the entire NH, (b) the WNP and (c) the NA. Best-fit Gamma distributions for the PDs are added in orange for LR and in grey for HR.

storms), an increase in more energetic storms would be anticipated. However, the change in probability from LR to HR above IKE values of 150 TJ is minor, suggesting no clear increase in probability of high-energetic storms. A possible reason for this could be the impact of storm size on IKE which - besides intensity - is the other factor determining

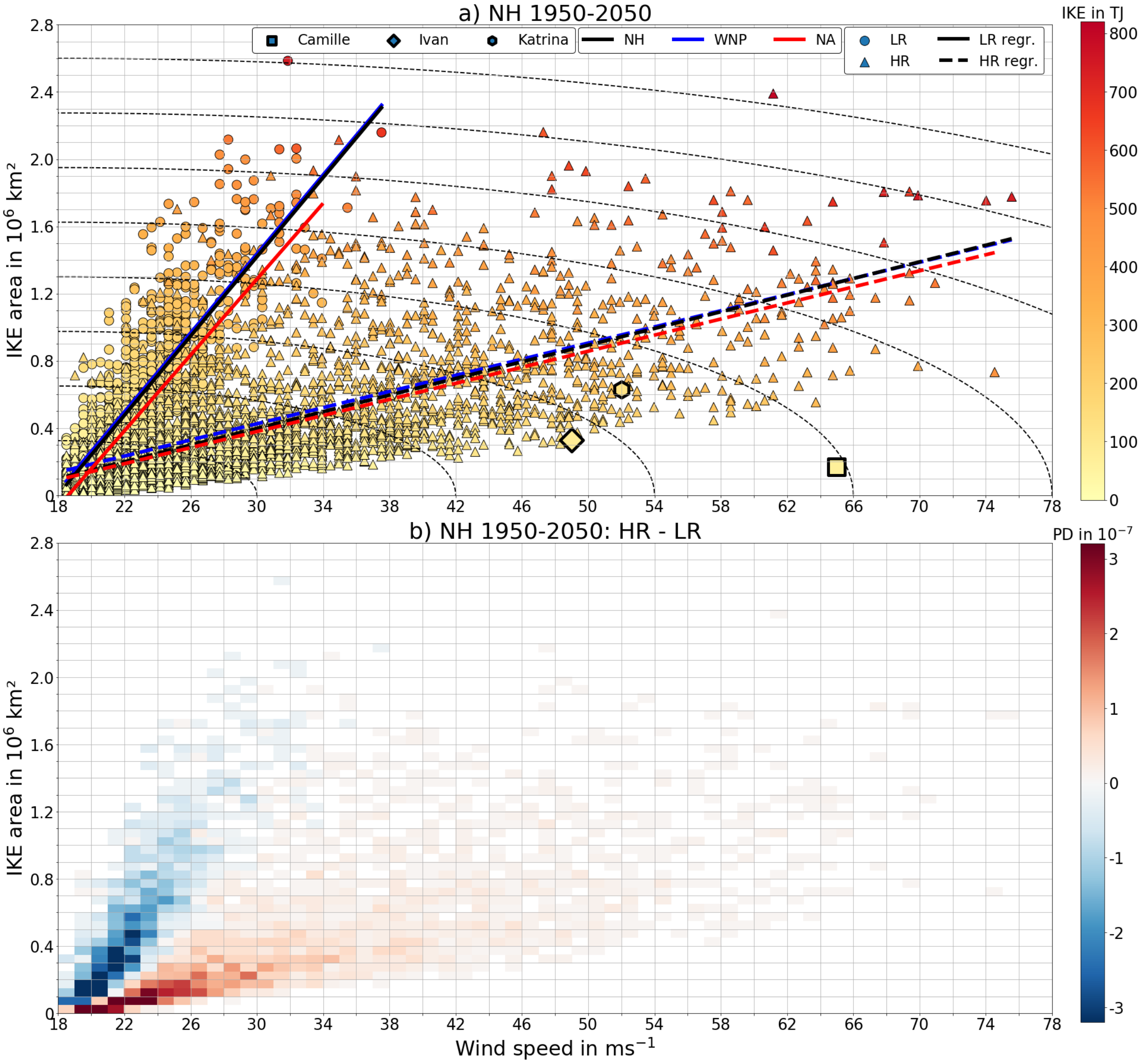

Figure 18: (a) Scatter plot of storm area above the 18 m s^{-1} wind speed threshold (IKE area) against wind speed associated with maximum lifetime IKE of all the storms in the entire NH from 1950-2050. IKE values are colour-coded for both resolutions, LR (circles) and HR (triangles). Regression lines (relative to wind speed threshold) are drawn in solid for LR and in dashed for HR. The regressions for the storms attributed to the WNP and NA are shown in blue and red, respectively. The dashed ellipses show an approximation of constant IKE values across the scatter plot. *Hurricanes Camille*, *Ivan* and *Katrina* are added using the data given in *Powell & Reinhold* (2007). (b) Difference between HR and LR in joint PD for IKE area and wind speed associated with maximum lifetime IKE of all the storms in the entire NH from 1950-2050. The bins are 1 m s^{-1} for the wind speed and $0.05 \cdot 10^6$ km^2 for the IKE area.

IKE. A decrease in TC size with resolution has been observed in previous studies as well (*Bengtsson et al.*, 2007; *Caron et al.*, 2011), thus this result is not entirely unexpected and motivates investigating the contribution of storm size to IKE.

Analysing the WNP and NA separately provides a similar picture. In the WNP (Fig. 17b), the difference between LR and HR in the range of 25-150 TJ is even more pronounced than for the entire NH, resulting in a stronger compensation by storms in the medium-energy range (200-500 TJ). Here, too, the KS-test confirms a significant change in probabilities. The NA shows a similar behaviour as the WNP, but additionally, is characterised by a decrease in probability for the weakest storms (0-25 TJ). This leads to an intersection between the two resolutions which is shifted more toward lower values (about 100 TJ) relative to the WNP where the curves intersect at about 200 TJ. It should be noted that the most extreme IKE values in the NA are lower than those in the WNP, which is consistent with typhoons being larger than NA hurricanes, on average (*Chavas & Emanuel*, 2010).

In order to gain insights into the IKE and to understand why LR and HR simulations produce storms with similar maximum IKE (on average), the relationship between wind speed and storm area with surface winds above tropical storm strength, i.e., the area of the storm that contributes to the IKE (IKE area), is evaluated. (Fig. 18a) depicts the relationship for both variables, as detected by the tracker at the time of maximum lifetime IKE for all storms in the entire NH from 1950 through 2050 and for both resolutions.

First, the figure provides additional proof that there is a higher number of storms in the HR integration (triangles) and that these are more intense than the storms in the LR integration (circles): The maximum wind speed associated with maximum lifetime IKE almost doubles from roughly 38 $\mathrm{m\,s^{-1}}$ to about 76 $\mathrm{m\,s^{-1}}$. Secondly, it shows that the largest storm area above tropical storm strength between both experiments is similar, with about $2.6 \cdot 10^6$ km^2 for LR and approximately $2.4 \cdot 10^6$ km^2 for HR. However, a clear difference between LR and HR is the distribution of the data points with storms in HR being shifted toward higher wind speeds. The linear regressions (solid and dashed black lines) confirm this difference and reveal that TCs in HR are characterised by a smaller IKE area relative to TCs in LR (at constant wind speed). The blue and red lines, depicting the regressions for storms in the WNP and NA, show a similar behaviour, stating a uniform response for the individual basins. Furthermore, it is visible that storms in the NA are smaller than in the WNP as indicated by the red lines relative to the blue lines, consistent with the findings of *Chavas & Emanuel* (2010) who found typhoons being larger than NA hurricanes. (Fig. 18b) quantifies the difference in occurrence of storms of specific size and intensity at maximum lifetime IKE in the entire NH between HR and LR and clearly shows that for a given wind speed, storms tend to be larger in LR than in HR.

In Fig. 18a the wind speed, the storm area above tropical storm strength and the IKE at landfall of *Hurricanes Camille* (1969), *Ivan* (2004) and *Katrina* (2005) are added using the data given in *Powell & Reinhold* (2007). Since *Powell & Reinhold* (2007) do not provide direct data for IKE area, it was computed using the provided values (see Eq. 21 in the Appendix). The three storms clearly show that the wind speeds produced by the HR experiment are reasonable compared to major hurricanes but that

Correlation between maximum IKE and	NH (LR, HR)	WNP (LR, HR)	NA (LR, HR)
wind speed	0.87, 0.82	0.86, 0.81	0.90, 081
IKE area	0.99, 0.96	0.99, 0.96	0.99, 0.96
minimum MSLP	-0.78, -0.85	-0.76, -0.84	-0.88, -0.88

Table 5: Overview of correlations of maximum lifetime IKE of all storms for the period 1950-2050 with associated wind speed, IKE area and minimum MSLP for NH, WNP and NA. The first value is the correlation for LR, the second for HR.

the simulated IKE values are biased high with respect to these observations (compare colour-coding along the ellipses). This is mainly due to storm sizes too large in the CNRM model, especially compared to *Hurricane Camille*, whose size is considerably lower than simulated storms of similar intensity in the model. This indicates that a further increase in model resolution would be needed to realistically simulate very intense storms.

To determine whether storm intensity or size is the controlling factor on maximum IKE, the correlation coefficients (time period 1950-2050) are computed and displayed in Tab. 5. Additionally, the correlation between IKE and the minimum MSLP of the storm associated with the lifetime maximum IKE is shown. As expected, the correlations show that there is a strong relationship between the quantities: Correlation values of 0.99 in the LR integration in all basins show that IKE almost completely follows variations in storm size. The wind speed is correlated with slightly lower values of 0.87, 0.86 and 0.90 in NH, WNP and NA, still providing an excellent predictor for maximum IKE. Minimum MSLP, too, exhibits high correlation values, which is not surprising given that maximum surface wind and minimum MSLP are closely connected. Interestingly, the relationship between IKE and MSLP is stronger in the NA (-0.88) relative to the WNP (-0.76) indicating an enhanced predictive potential in that particular basin. The correlations in the HR experiment for wind speed and storm size are lower than in the LR experiment. Values in all basins drop from 0.99 to 0.96 for storm size and to 0.82 (NH) and 0.81 (WNP and NA) for wind speed, suggesting that the increase in resolution decreases the amount of explained variance in IKE by these particular quantities. Interestingly, MSLP seems to be more correlated to IKE than maximum wind speed at HR, but this is not the case in LR. The reason for this is not clear at this stage. However, the correlations show that storm size remains the dominant factor in driving IKE, even at HR.

5.3 IKE Variability and Impacts of a Changing Climate

In the previous section, it was shown that LR and HR simulations generate storms of similar maximum lifetime IKE, despite the enhanced resolution and the resulting increase in wind speed in HR. However, it has also been shown that HR produces more storms relative to LR (Fig. 14) which means that the seasonally accumulated IKE, i.e., the Track Integrated Kinetic Energy (TIKE) summed up over all storms per season (seasonal TIKE), is expected to be higher in HR. Indeed, Fig. 19 confirms that the seasonal TIKE (5-year running mean applied to smooth out strong interannual variabilities like ENSO) for the NH (a), the WNP (b) and the NA (c) is considerably higher in HR than in LR, owing to the higher storm frequency. Moreover, it reveals that most of the IKE generated in the NH is produced in the WNP, also owing to the largest portion of storms being generated in that basin. Although the number of storms generated in the NA is lower than in the WNP, the increase in resolution and thus the increase in storm frequency result in a relatively higher increase in TIKE relative to LR. The order of magnitude of the range of the NA seasonal TIKE in HR compares well to the study of *Misra et al.* (2013) who, too, calculated NA seasonal TIKE using the Colorado State University Extended Best Track dataset from 1990-2011 (*Demuth et al.*, 2006): Their estimate roughly ranged between 1 and 22 TJ whereas the seasonal TIKE presented in this study ranges from 6 to 12 TJ, yielding less extreme values. Taken into consideration the low bias in TC frequency and intensity relative to observations and the fact that *Misra et al.* (2013) considered all TCs in the NA rather than up to 40°N, the value presented here appears reasonable.

The linear trend over the 100-year time period has been calculated and is shown with a dashed line. In LR, the trend is slightly negative for the NH and the WNP, whereas it shows a steady behaviour in the NA over the entire period. In HR, the WNP is characterised by a decreasing trend whereas the NA is characterised by an increasing trend. This difference might be due to the contributions of the future period which has been found to have a relatively lower storm frequency in the WNP and a higher frequency in the NA (Fig. 14). As mentioned above, the WNP contributes most of the IKE output in the NH, hence why the trend in the NH is also negative.

As pointed out, a trend in the seasonal TIKE can strongly be related to the number of storms in a given time period and is not necessarily connected to the maximum IKE of storms. A more detailed insight into the temporal evolution of the maximum energy content of the storms is given in Fig. 20. It shows the 5-year aggregated maximum lifetime IKE in terms of the the 5-year median (black horizontal line), the 25$^{\text{th}}$ and 75$^{\text{th}}$ percentiles (upper and lower corners of the boxes), the 5$^{\text{th}}$ and 95$^{\text{th}}$ percentiles (whiskers) and the outliers above the 95$^{\text{th}}$ percentiles (crosses) for storms in the NH. The figure gives further evidence for the similarity in maximum IKE between LR and HR as it

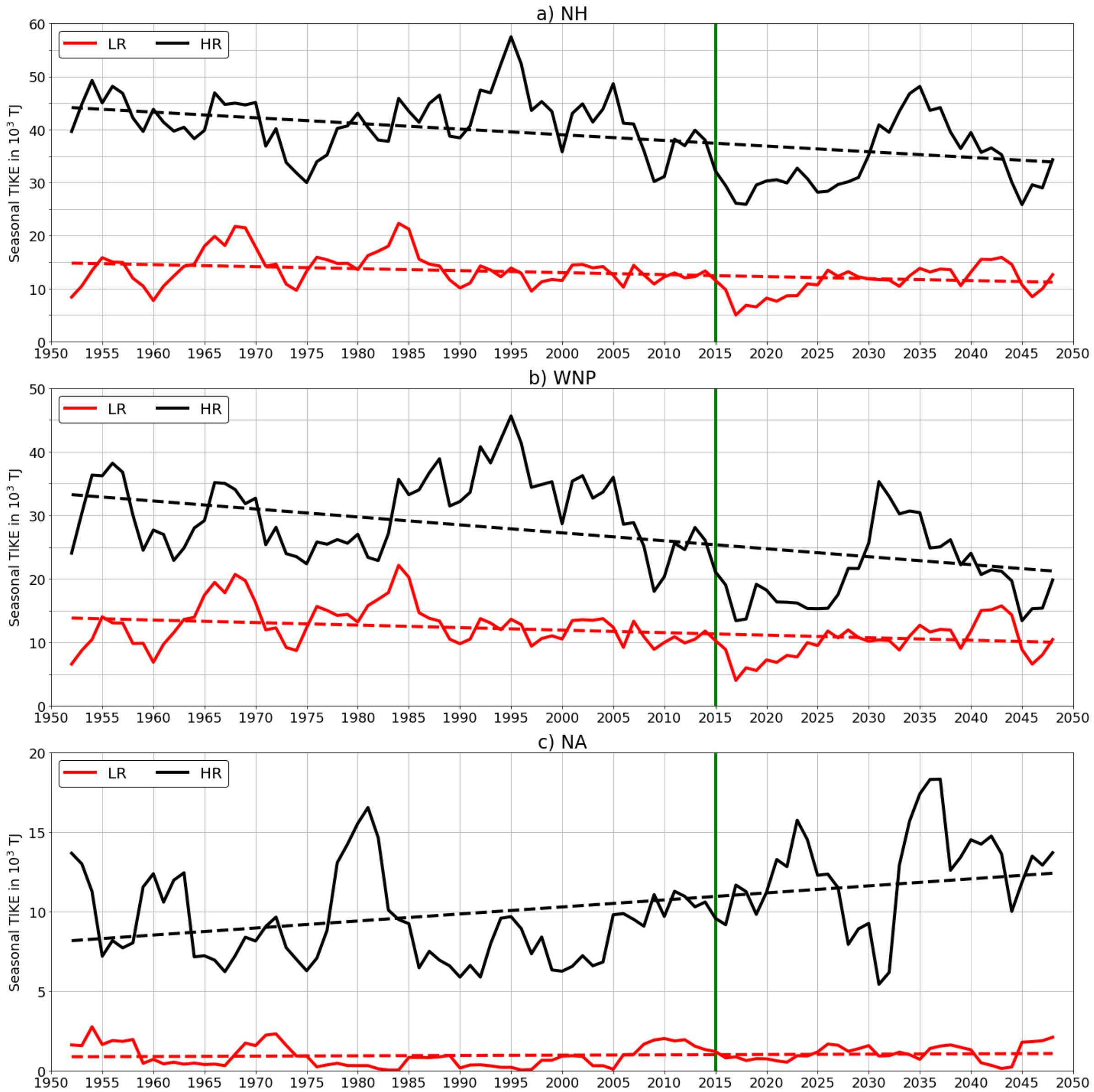

Figure 19: Seasonally accumulated maximum TIKE for all storms (seasonal TIKE) in the NH (a), the WNP (b) and the NA (c). LR is shown red, HR in black. A 5-year running mean has been applied. The respective regression lines for the entire period are shown in dashed.

reveals that the median maximum IKE remains relatively constant between a range of 80-100 TJ for both resolutions. Furthermore, the individual 5-year medians always stay within the 25th and 75th percentiles of all the other years.

The 95th percentiles indicate that HR can produce storms with larger IKE than LR. The upper whiskers in HR reach values of around 400 TJ more frequently than in LR, where they mostly reach values around 300 TJ. A comparable median between the two resolutions is achieved by the fact that HR also generates more weak storms relative to LR as can be seen by the 5th percentiles which include smaller values in HR. This behaviour can be seen throughout the entire time period with no indication for a trend

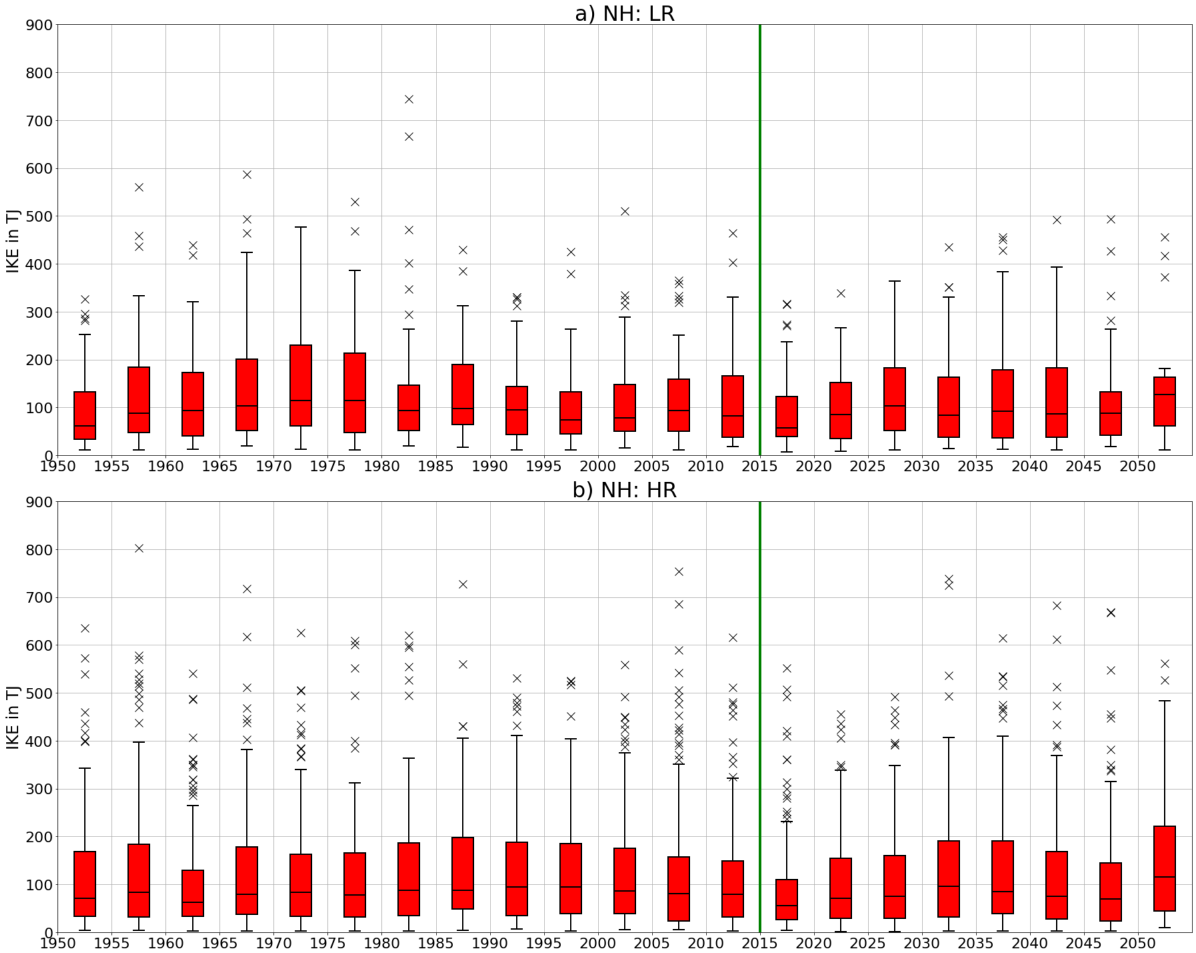

Figure 20: Boxplot of all storms in the NH from 1950-2050 for LR (a) and HR (b). The storms are aggregated in 5-year intervals (e.g., from 1950-1954, 1955-1959 etc.) with the box being centred in the middle of the respective interval. The black bar within the boxes depicts the median (50$^{\text{th}}$ percentile), while the lower and upper boundaries of the boxes represent the 25$^{\text{th}}$ and 75$^{\text{th}}$ percentiles, respectively. The lower and upper whiskers represent the 5$^{\text{th}}$ and 95$^{\text{th}}$ percentiles. The crosses mark all the storms which lie outside of the 95$^{\text{th}}$ percentile. The green line represents the transition from present to future time period.

in median maximum IKE in any of the resolutions, suggesting there is little impact of the altered climate. The figures for the WNP and NA are shown in Fig. 30 and Fig. 31 in the Appendix and offer similar pictures and further confidence in the results presented here.

Fig. 21 is presented to investigate whether there are notable differences in wind speed and storm size between the present and the future period. It shows all the storms in the NH for the period 1950-2050 but separated for 1950-2014 (circles) and 2015-2050 (triangles) and for both resolutions (Fig. 21a, b). Only the NH is shown here since it is representative of the individual basins as demonstrated in Fig. 18 where the WNP and NA are in close agreement with the results of the NH. The differences between the regression lines for present (dashed) and future (solid) in both resolutions are of different

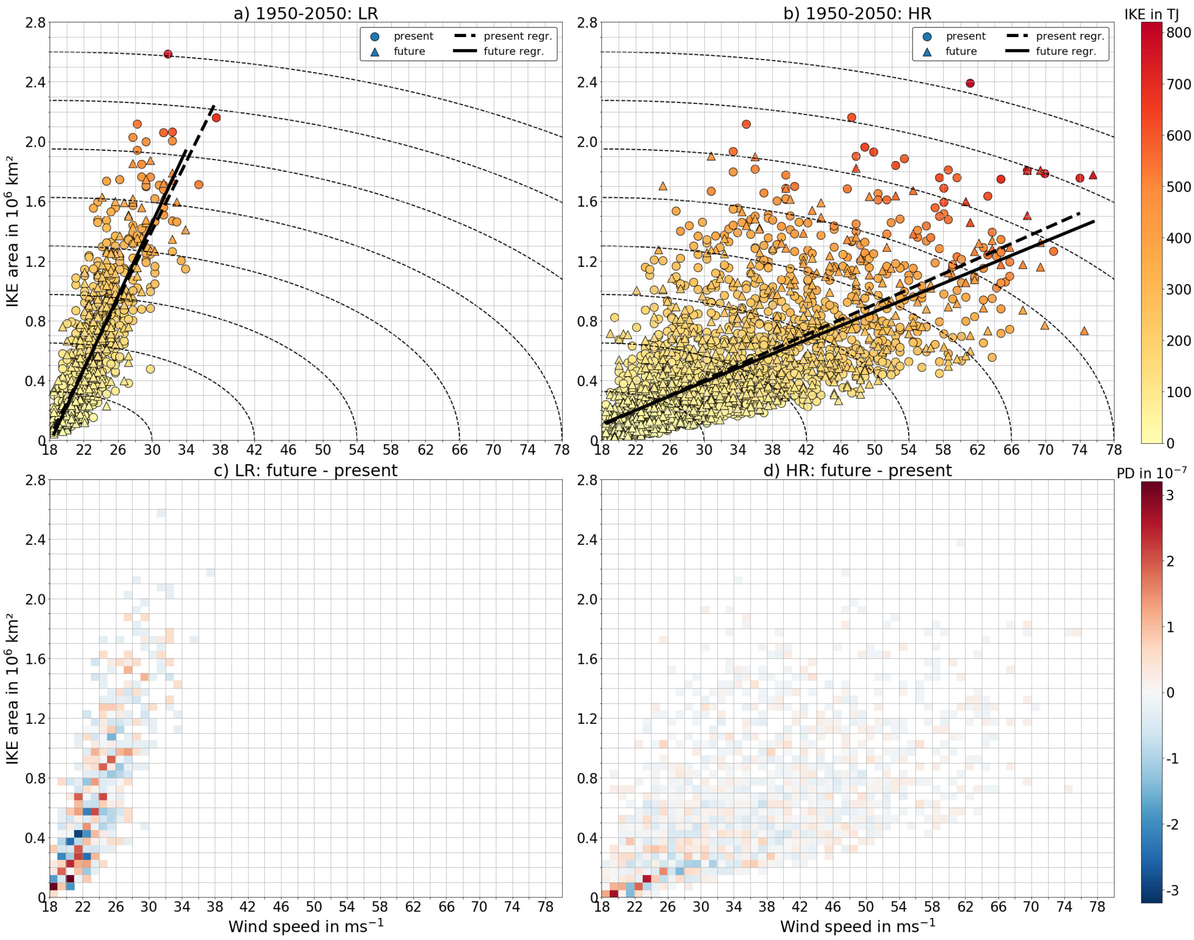

Figure 21: (a) Scatter plot of storm area above 18 $\mathrm{m\,s^{-1}}$ wind speed threshold (IKE area) against wind speed associated with maximum lifetime IKE of all the storms in the entire NH from 1950-2050 for LR (a) and HR (b). IKE values are colour-coded for both periods, present (circles) and future (triangles). NH regression lines (relative to wind speed threshold) are drawn in dashed for present and in solid for future. The dashed ellipses show an approximation of constant IKE values across the scatter plot. Differences between future and present in joint PD for IKE area and wind speed associated with maximum lifetime IKE of all the storms in the entire NH are shown for LR (c) and HR (d). The bins are 1 $\mathrm{m\,s^{-1}}$ for the wind speed and $0.05 \cdot 10^6$ km^2 for the IKE area.

signs, but overall, they are minor, indicating that there is no significant change in storm intensity or size. The small change, especially relative to the impact of resolution, explains the similar IKE characteristics for present and future. Additional evidence is given by Fig. 21c, d which show the differences in joint PDs between future and present. As anticipated, they do not reveal considerable changes or patterns between the time periods.

Given similar storm intensity and size conditions between present and future, no or only very little change in maximum IKE PDs is expected. This expectation is confirmed by Fig. 22 which separates the PD analysis for the individual basins and resolutions: The PDs and fitted Gamma distributions for the NH and the WNP reveal almost identical

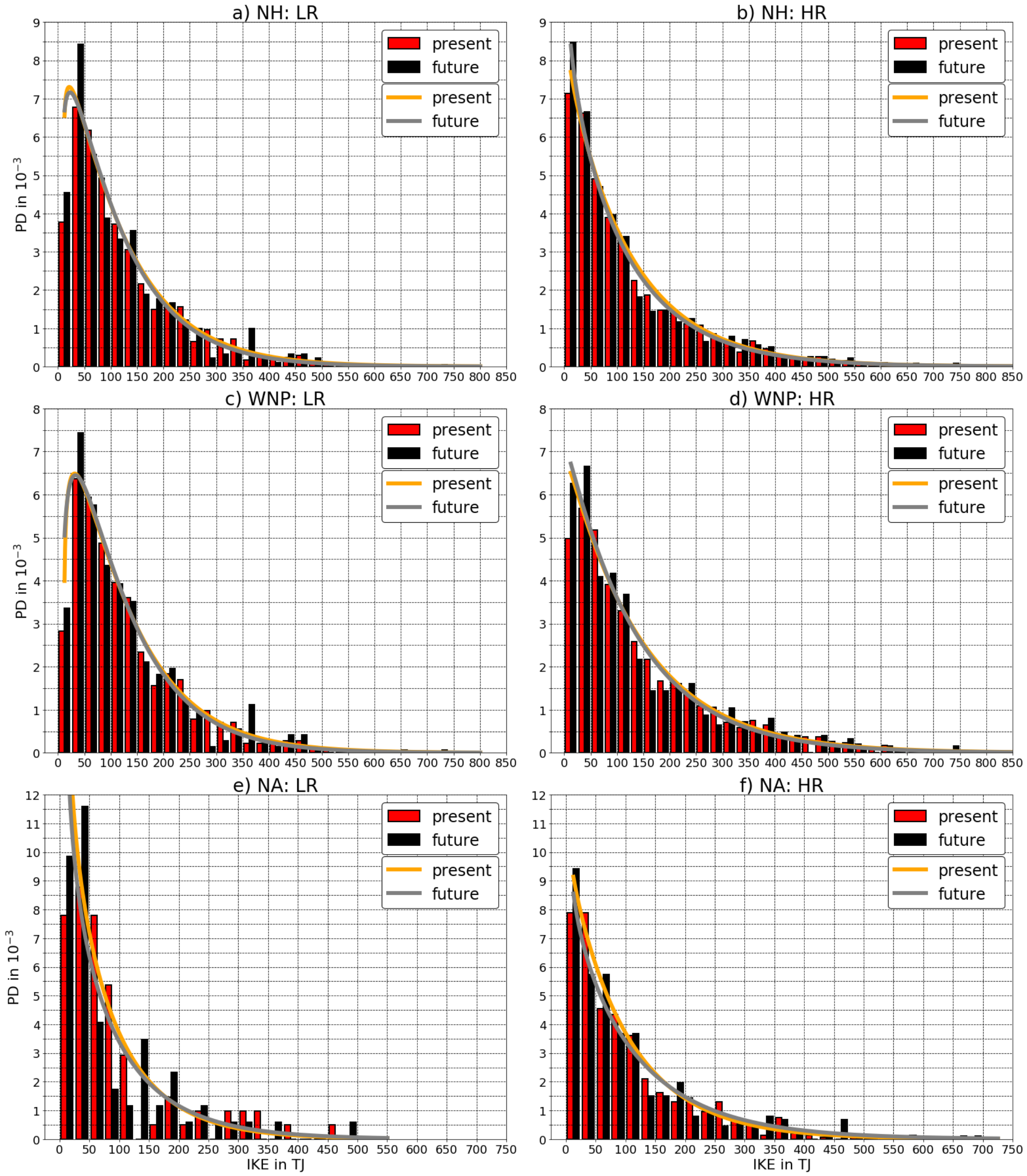

Figure 22: Comparison of PDs for all storms in the respective ocean basins in LR and HR to reach specific lifetime maximum IKE. Bin sizes are 25 TJ, starting at 0 TJ. Red and black bars are for present and future time period, respectively. Left panels represent the LR experiment, right panels the HR experiment. The top row represents the entire NH, the middle row the WNP and the bottom row the NA. Best-fit Gamma distributions for the PDs are added in orange for the present and in grey for the future.

characteristics at both resolutions. Consequently, the KS test fails to detect a significant difference between the time periods. The same outcome is given for the NA, concluding a uniform response of the individual basins and the NH to the altered climate. However, a slight but not sufficiently large decrease in PD in the NA can be seen below maximum IKE values of 150 TJ in both resolutions and an accompanying slight increase above values of 200 TJ. For the LR integration this might be a consequence of the above-mentioned low number of storms which is also reflected in some of the bis in Fig. 22e. The HR integration, which is more robust in terms of TC sample size, could be impacted by the influence of a multidecadal natural variability like the AMO. For instance, a positive phase of the AMO would enhance NA SSTs (*Vimont & Kossin*, 2007; *Patricola et al.*, 2014) and provide more energy to intensify TCs. That increase in intensity could be responsible for the observed slight shift in IKE toward higher values.

Considering that previous studies have found indications for an increase in global maximum lifetime storm intensity (*Knutson et al.*, 2019) and an increase in storm size (*Sun et al.*, 2017) with climate change, the above findings are surprising. The lack of intensity change between present and future in this formulation of the CNRM model is also unexpected as *Chauvin et al.* (2019) were able to detect an increase in the intensity of major hurricanes in the CNRM model. However, their model formulation did not follow the HighResMIP protocol and included a horizontal resolution of 15 km which is about three times as fine as the resolution used for the HR experiment in this study. A further refinement from 50 km down to 15 km might lead to the representation of unresolved processes and eventually to the representation of a signal in storm intensity between present and future. It should also be noted that - due to its capability to resolve wind speeds close to observations - the CNRM model is not representative of the majority of models used to assess TC characteristics in a changing climate (*Roberts et al.*, 2020): According to *Davis* (2018), the CNRM model should not be capable of producing such high wind speeds at the used resolutions and presently it is being investigated how the CNRM model is able to do so. It is suggested that a newly implemented turbulence scheme might be the cause for this (*Chauvin et al.*, 2019).

Now that no significant change between present and future maximum IKE time series has been found, it is assessed whether a different response at the basin wide scale can be found. Fig. 23 presents the maximum IKE per storm per $2° \times 2°$ grid boxes for the present and future for both resolutions. Close-up views of the WNP and the NA basin are shown in Fig. 32 and Fig. 33 in the Appendix. The changes in track density and their close-up views are shown in Fig. 34-Fig. 36. In the WNP, a mixed response of positive and negative signals, similar to that in Fig. 16, can be seen in both resolutions (Fig. 23e, f). However, the pattern is characterised by a bipolar structure rather than a tripolar structure. In LR, there is a pronounced negative signal east of Taiwan and a weaker positive signal southwest of Japan. In HR, the response is weaker in general, but also with a negative signal east of Taiwan. In addition, the area southwest of Japan is also characterised by a negative response. The centre of positive response is shifted toward the region east of Japan. Overall, although both resolutions show some different

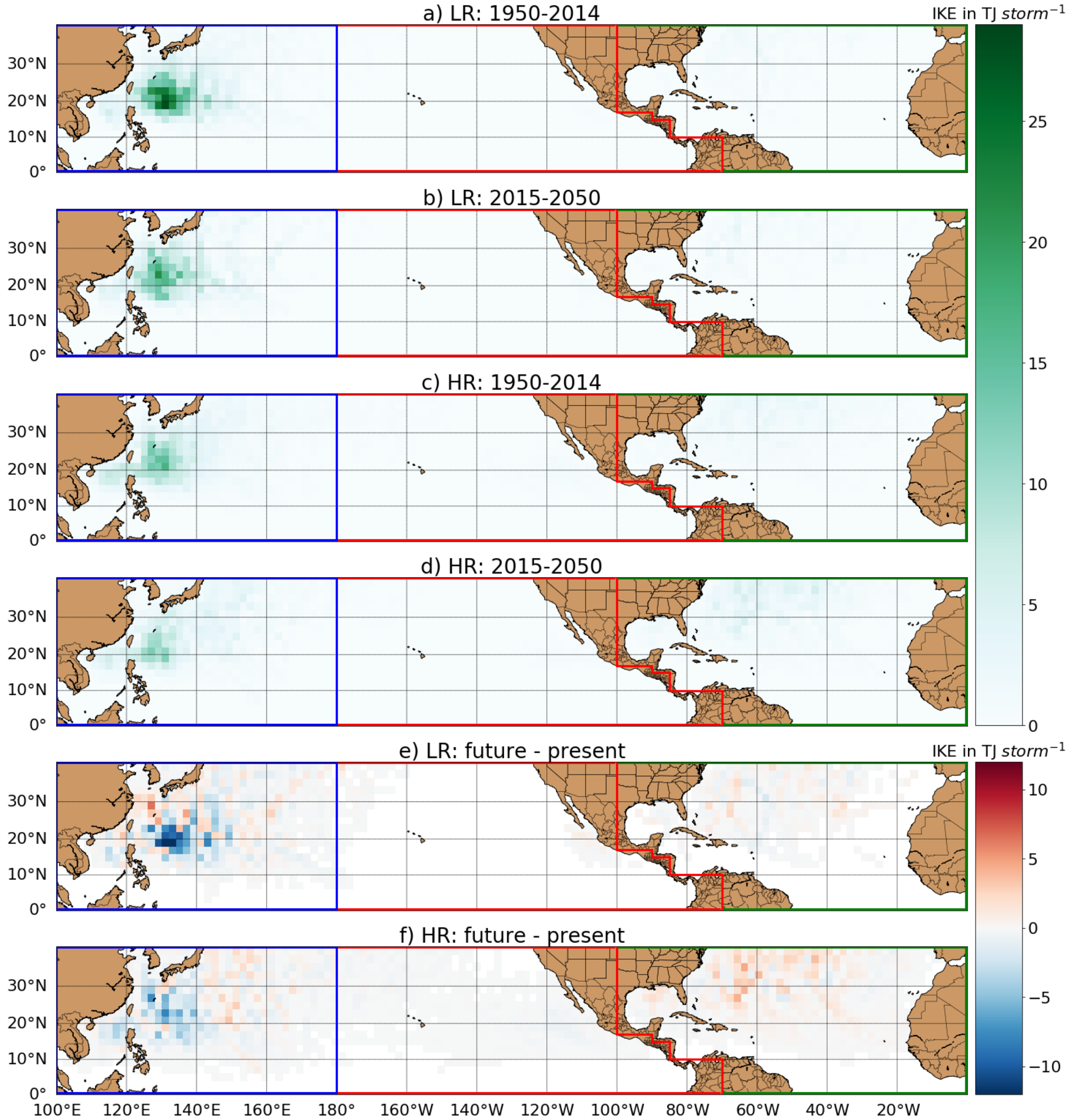

Figure 23: Maximum IKE distribution per storm in the NH per $2^\circ \times 2^\circ$ grid cells for LR and HR from 1950-2014 and 2015-2050 (a-d), (e) and (f) differences between future and present. The IKE associated with all storm transits in the respective grid boxes was summed up and then averaged over all those storm transits.

features, they agree on a decrease in maximum IKE east of Taiwan, with LR showing the stronger signal.

In the NA, the LR shows a weak and mixed response throughout the entire basin. The weak signal detected may be a consequence of the low total number of storms detected in this integration. In HR, a positive change relative to the present period is notable north of 20°N with its maximum between 60°W-70°W, suggesting that storms in the NA

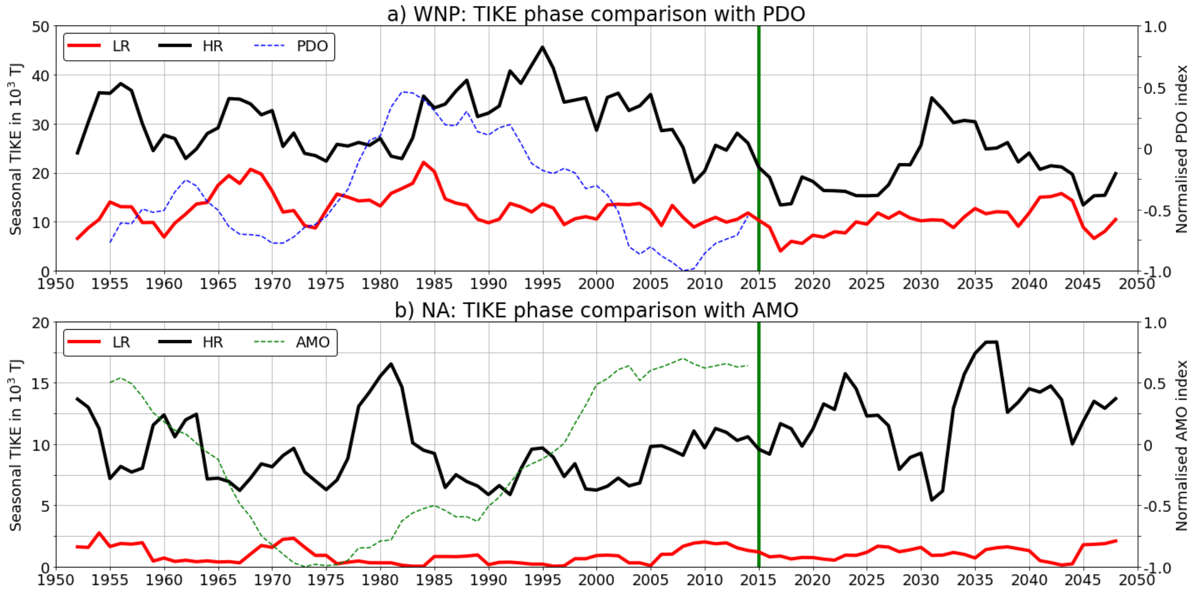

Figure 24: Comparison of the seasonal TIKE in the WNP (a) and the NA (b) with the normalised PDO and AMO indices described in Sect. 3.5.3. A 5-year running mean has been applied to the TIKE time series and an 11-year running mean to PDO and AMO indices.

may become slightly more energetic. The magnitude of the changes in the NA is slightly weaker than the response in the WNP basin. This finding could be related to the minor and non-significant shift in PDs toward more energetic storms as seen in Fig. 22f which could be driven by natural variability or by anthropogenic climate change.

To reveal if the PDO and AMO - which have been demonstrated to influence TC behaviour in the WNP and NA (*Vimont & Kossin*, 2007; *Chan*, 2008; *Patricola et al.*, 2014) - exhibit an impact on the seasonal TIKE, Fig. 24 displays the seasonal TIKE for the WNP (a) and the NA (b) together with the normalised PDO and AMO indices (11-year running mean applied). Especially, the phases of the PDO and the seasonal TIKE in the WNP appear to be related. The seasonal TIKE in the WNP follows the phase of the PDO with some delay. This can be seen by the peak of the PDO around 1982 and a subsequent decline which can also be observed in the WNP TIKE, roughly ten years later. As pointed out by *Chan* (2008), positive phases of the PDO steer TCs in the WNP such that these experience an increased energy input from large SSTs. Correlation values of 0.28 and 0.24 for LR and HR are not large (not tested for significance) but suggest some potential for predictability of TIKE through the PDO which might even be enhanced at a given time lag. The correlations between the AMO and seasonal TIKE in the Atlantic are 0.24 and -0.03 for LR and HR, respectively. Based on the correlation with the HR experiment, the AMO is an unlikely candidate for being the driver of the changes in NA maximum IKE, but *Mei et al.* (2019) and *Roberts et al.* (2020) have shown that in climate studies many ensemble members are needed to extract robust relationships with interannual variabilities. However, on shorter time scales the MJO, ENSO and the AWP are known to influence TC activity in the NA (*Pielke & Landsea*, 1999; *Vimont & Kossin*, 2007; *Wang et al.*, 2011; *Misra et al.*, 2013; *Klotzbach*, 2014), but the applied smoothing to the TIKE should have eliminated those signals. Solely the AMM has been found to impact TC activity in the NA on time scales longer than the applied smoothing of five years (*Vimont & Kossin*, 2007), thus it could be the driver for the variability associated with NA TIKE.

6 Conclusions

As no other study before, this study addressed the impact of a refinement in horizontal model resolution and a changing climate on the Integrated Kinetic Energy of tropical cyclones, a recent measure to address the lack of information on storm size in damage estimates. This has been done by assessing the capability of the CNRM climate model to produce TCs and by evaluating their characteristics and statistics with respect to their frequency, intensity and IKE. Two uncoupled atmosphere-only experiments for a historical forced simulation (1950-2014) and a future projection (2015-2050), following the CMIP6 HighResMIP protocol, have each been run at a standard resolution (LR: $1.4° \times 1.4°$) and an increased resolution (HR: $0.5° \times 0.5°$) to attribute the simulated changes to either the resolution or the time period. The study has focused on TCs in the NH and investigated changes in three ocean basins (WNP, ENP, NA), individually and in combination. The findings and their interpretation are presented in the following:

- Using the *BSC Cyclone Tracker* to detect TCs in the CNRM model output required the choice of a set of tracking parameters. Testing the tracker in various test cases showed that the standard values suggested by the developers were able to produce reasonable results in terms of TC detection and tracking hence why those values were adopted for this study. The tests also revealed issues with tracking TCs close to areas of high orography in HR, e.g like Taiwan: An increase in resolution leads to a better representation of the topography which results in virtual MSLP values above those regions. Those anomalies appear to interfere with the tracking of nearby storms by distorting their pressure field (Fig. 13) which is suggested to be responsible for the unexpected ending of the tracking of many TCs in those areas.
- TC climatology in all experiments performed in this study (Fig. 14) shows that the WNP is the most active basin in terms of TC frequency, followed by the NA and the ENP. According to the observed climatology derived from the IBTrACS data base (*Knapp et al.*, 2010; *Ramsay*, 2017), the ENP is more active than the NA, in contradiction with the results presented here. A possible reason for that could be too coarse a resolution of the CNRM model to sufficiently resolve orography on the American continent (e.g., Sierra Madre) which plays an important role for generating TCs in the ENP by providing vorticity (*Zehnder*, 1991; *Mozer & Zehnder*, 1996). The detected low number of storm events in the ENP hindered statistical analyses due to a small sample size so that the ENP was only considered in combination with the other two basins.
- The increase in resolution leads to an enhanced capability to generate TCs in all basins (Fig. 14 and Fig. 15). The largest increase in storm frequency was observed

in the South China Sea, close to the Chinese coast, increasing the hazard of land-falling TCs. However, despite the increase in storm frequency, which relatively is more pronounced in the ENP and NA than it is in the WNP, TCs remain biased low in all basins with respect to the observed climatology. Furthermore, a basin wide increase in storm intensity with resolution could be found in all individual basins. The highest observed SSHWS category in LR was 1 which could be enhanced to category 5 in HR. Both findings are consistent with previous studies of *Chauvin et al.* (2019) and *Roberts et al.* (2020) who also concluded increasing global TC frequency and intensity with resolution using the CNRM model. However, *Roberts et al.* (2020) showed positive and negative signals in all basins in response to the increase in resolution. This result might be a consequence of the chosen trackers which differ from the one used in this study.

- Comparing the present and the future period against each other (Fig. 14) does not reveal considerable changes in global TC activity (in terms of storm numbers per year). However, different responses between the Pacific and the Atlantic could be found where the signal was negative and positive, respectively. This is in line with the findings from *Chauvin et al.* (2019), *Roberts et al.* (2020) and *Roberts et al.* (subm.) who also found mixed responses in the NH and were unable to detect a significant trend in storm frequency between present and future. Moreover, no robust change toward storms of higher intensity was found between the time periods, not supporting the finding by *Knutson et al.* (2019).
- Increasing the resolution has a significant impact on the PDs (Fig. 17) associated with the maximum lifetime IKE of TCs in the entire NH, the WNP and the NA in the time period from 1950 through 2050. A performed KS test significantly distinguishes Gamma distributions (at the 5% significance level) fitted to the data of the LR and HR experiment. Particularly, the low-energy range below 200 TJ (100 TJ for the NA) shows a pronounced decrease in PDs with resolution, whereas the energy-range above this value is characterised by only a small increase. With the increase in TC intensity with resolution, a strong increase in maximum IKE had been expected, but analyses of the wind speeds and storm sizes above tropical strength showed that the increase in intensity is accompanied by decreasing storm sizes (Fig. 18). This result is in agreement with the study of *Bengtsson et al.* (2007) and *Caron et al.* (2011) who, too, were able to establish a decrease in TC size with a refinement in horizontal resolution. The opposing effects of higher wind speed and reduced storm size with resolution somewhat balance one another and result in similar IKE values between LR and HR. Furthermore, correlation analyses showed that the observed storm sizes have a bigger impact on the IKE relative to the wind speed in all basins. The result is consistent across both

resolutions, suggesting that wind speeds have to change relatively more than storm sizes in order to balance the IKE contributions.

- Basin wide analyses of the maximum IKE content per storm in the time period from 1950-2050 (Fig. 16) reveal a mixed signal throughout the WNP basin in response to the increase in resolution: A tripole pattern emerges with centres of increased IKE per storm located in the South China Sea as well as east of Japan and decreased IKE per storm east of Taiwan/south of Japan. Taking into consideration the enhanced storm frequency in the South China Sea, a refinement in model resolution increases the risk associated with TCs near the Chinese coast. In the NA, a positive response north of 20°N with a lower magnitude than in the WNP could be observed, resembling the change in track density caused by the enhanced resolution. This suggests an increase in storm frequency and storm IKE throughout the entire basin. However, due to the low frequency of storms in the NA in LR, this result may be related to the increase of the sample size and should be interpreted with caution.
- Seasonally accumulated TIKE over all storms is considerably higher in HR than in LR for all basins (Fig. 19), owing to the higher storm frequency. The increase in seasonal TIKE from LR to HR is most pronounced in the NA basin due to the relatively larger increase in storm frequency. The simulated range of the seasonal TIKE in the NA in the HR experiment yields reasonable values (6-12 TJ) compared to the observations of *Misra et al.* (2013) (1-22 TJ). Correlations with the PDO and AMO indices (Fig. 24) show that the PDO has some influence on the evolution of the seasonal TIKE in the WNP, whereas the AMO exhibits almost no influence on NA seasonal TIKE (in HR). However, as shown by *Mei et al.* (2019) and *Roberts et al.* (2020), multiple ensemble members are needed to detect robust relationships with climate variabilities in climate models. While no clear trend in seasonal TIKE could be found over the 100-year period in the LR experiment, the HR integration showed a negative trend in the WNP which - due to a higher storm frequency relative to the other basins - also drives a similar trend in the entire NH. In the NA, a positive trend could be found which is suggested to be a consequence of the different responses in storm frequency toward the end of the time series (future period). In addition, it has been shown that the median maximum IKE remains relatively constant between a range of 80-100 TJ for both resolutions (Fig. 20). Although HR produces storms of larger maximum IKE than LR, their contribution is balanced by an increase of the weakest storms, as shown by the PD analysis (0-25 TJ in the NH and WNP).
- For all basins, it has been shown that for both resolutions there are no pronounced differences in the relationship of storm intensity and size between the present

and the future, especially relative to the changes caused by the refinement in resolution (Fig. 21). These small changes explain why the PDs of maximum lifetime IKE are not significantly distinguishable from one another (Fig. 22) and why the median seasonal TIKE remains stable around values of 80-100 TJ across both time periods. These results suggest there is no clear impact of the change in forcings on storm size and intensity which is in contrast to previous studies that have found an increase in global maximum lifetime storm intensity (*Knutson et al.*, 2019) and an increase in storm size (*Sun et al.*, 2017) with anthropogenic climate change. It also disagrees with the study of *Chauvin et al.* (2019) who detected an increase in the intensity of major hurricanes in the CNRM model, although that study used a resolution of 15 km. It has to be kept in mind that the presented study only includes one model with one ensemble member from which it is difficult to obtain robust conclusions. Furthermore, the current formulation of the CNRM model has been shown to not be representative of other climate models as it produces wind speeds too high relative to its resolution (*Davis*, 2018; *Roberts et al.*, 2020), possibly related to the implementation of a new turbulence scheme (*Chauvin et al.*, 2019). Future studies with more ensemble members, coupled model configurations and multiple models could help bridge the gap between the demonstrated differences. In particular, it will be interesting to see whether a changed forcing has little impact on the storm IKE, as in the CNRM model.

- Lastly, the changes in maximum lifetime IKE per storm on a basin wide scale between the present and the future were assessed (Fig. 23). Across both resolutions, the model suggests a slight decrease in IKE in the western end of the WNP. The response in the LR experiment in the NA is more mixed and of lower magnitude than in the WNP. It is likely that the results for this particular basin suffer from the poor representation of TCs in the Atlantic in LR. In HR, a slight positive change - although weaker than in the WNP - relative to the present period is notable north of 20°N, suggesting that storms in the NA may become slightly more energetic. PDs have shown that this increase is non-significant and it is suggested that this signal might be caused by a climate variability longer than five years, such as the AMM which has been shown to impact TC activity in the NA on longer time scales (*Vimont & Kossin*, 2007).

As mentioned above, the use of only one model and one ensemble member is not sufficient to draw robust conclusions. In order to obtain reliable results about the development of IKE in a future climate, further analyses need to be performed. Ideally, an extension of this study to more ensemble members and other models could prove to be beneficial. Further studies should also address the use of a coupled atmosphere-ocean model to allow for adjustments in the state of the ocean to the future forcing. As pointed out by *Emanuel* (2001) and *Cione & Uhlhorn* (2003), atmosphere-only simulations suffer from the lack of atmospheric feedback to the ocean and cannot represent the reduced exchange of heat between the two, which eventually leads to a weakening of the TC. Thus, although still biased low relative to observations, TC intensities in uncoupled simulations tend to be overestimated.

A further increase in model resolution toward the proposed threshold of 2 km (*Gentry & Lackmann*, 2010) to completely resolve features relevant to TC formation such as convection, mixing or local orography will positively impact the representation of TCs and their characteristics. To enable simulations of these resolutions at climate time scales, locally refined grids or adaptive grids could prove to be useful until advances in computational technology allow for further enhancements of the global resolution. Also, the use and comparison of different trackers will be crucial to comparing results. *Roberts et al.* (2020) used two trackers (*TRACK* and *TempestExtremes*) in their study, both using different criteria for storm recognition than the tracker used in this study, and were able to produce different signals in track density changes between HR and LR, whereas this study only found changes of positive sign.

Particularly, insurance companies would benefit from these improvements to simulating TC IKE. The use of the ACE index or PDI, which are based on maximum sustained wind speed, might turn out to be an inaccurate practice when calculating damages, especially under a future climate change scenario: Projected increases in maximum storm intensity would be accounted for using those indices, but changes in storm size and their impact on potential losses would not be represented. As this study has shown that storm size is a more important driver of IKE than storm intensity, the importance of including storm size for extrapolating future changes in damages is highlighted which favours the use of IKE over ACE and PDI. However, further studies need to be performed in order to provide additional evidence for the relationship of IKE and climate change.

Overall, the presented study emphasises the relevance of model resolution for the representation of TC characteristics, especially with respect to the measure of IKE, storm intensity and size. The impact of a changing climate on maximum lifetime IKE of the simulated storms in this particular model and experiment configuration is unexpectedly low, motivating further studies to understand the processes and mechanisms leading to this result.

References

Aon Benfield (2018): Global economic losses. Weather, climate and catastrophe insight 2017 annual report. Aon Benfield UCL Hazard Research Centre Rep. 2–5. URL: http://thoughtleadership.aonbenfield.com/Documents/20180124-abif-%20annual-report-weather-climate-2017.pdf.

ASCE (2016): Associated Criteria for Buildings and Other Structures. *ASCE/SEI*, 7–16.

Baudouin, J.-P., Caron, L.-P. & Boudreault, M. (2019): Impact of reanalysis boundary conditions on downscaled Atlantic hurricane activity. *Climate dynamics*, 52.5-6, 3709–3727.

Bell, G. D. & Chelliah, M. (2006): Leading tropical modes associated with interannual and multidecadal fluctuations in North Atlantic hurricane activity. *Journal of Climate*, 19.4, 590–612.

Bell, G. D., Halpert, M. S., Schnell, R. C., Higgins, R. W., Lawrimore, J., Kousky, V. E., Tinker, R., Thiaw, W., Chelliah, M. & Artusa, A. (2000): Climate assessment for 1999. *Bulletin of the American Meteorological Society*, 81.6, S1–S50.

Bellucci, A., Haarsma, R., Gualdi, S., Athanasiadis, P., Caian, M., Cassou, C., Fernandez, E., Germe, A., Jungclaus, J., Kröger, J. et al., (2015): An assessment of a multi-model ensemble of decadal climate predictions. *Climate Dynamics*, 44.9-10, 2787–2806.

Bengtsson, L., Böttger, H. & Kanamitsu, M. (1982): Simulation of hurricane-type vortices in a general circulation model. *Tellus*, 34.5, 440–457.

Bengtsson, L., Hodges, K. I., Esch, M., Keenlyside, N., Kornblueh, L., Luo, J.-J. & Yamagata, T. (2007): How may tropical cyclones change in a warmer climate? *Tellus A: Dynamic Meteorology and Oceanography*, 59.4, 539–561.

Bryan, G. H. & Rotunno, R. (2009): The maximum intensity of tropical cyclones in axisymmetric numerical model simulations. *Monthly Weather Review*, 137.6, 1770–1789.

Camargo, S. J. & Sobel, A. H. (2005): Western North Pacific tropical cyclone intensity and ENSO. *Journal of Climate*, 18.15, 2996–3006.

Camargo, S. J., Wheeler, M. C. & Sobel, A. H. (2009): Diagnosis of the MJO modulation of tropical cyclogenesis using an empirical index. *Journal of the Atmospheric Sciences*, 66.10, 3061–3074.

Camargo, S. J. & Wing, A. A. (2016): Tropical cyclones in climate models. *Wiley Interdisciplinary Reviews: Climate Change*, 7.2, 211–237.

Caron, L.-P., Boudreault, M. & Bruyere, C. L. (2015): Changes in large-scale controls of Atlantic tropical cyclone activity with the phases of the Atlantic multidecadal oscillation. *Climate Dynamics*, 44.7-8, 1801–1821.

Caron, L.-P., Jones, C. G. & Winger, K. (2011): Impact of resolution and downscaling technique in simulating recent Atlantic tropical cylone activity. *Climate dynamics*, 37.5-6, 869–892.

Carr III, L. & Elsberry, R. L. (1990): Observational evidence for predictions of tropical cyclone propagation relative to environmental steering. *Journal of the atmospheric sciences*, 47.4, 542–546.

Chan, J. C. (1985): Tropical cyclone activity in the northwest Pacific in relation to the El Niño/Southern Oscillation phenomenon. *Monthly Weather Review*, 113.4, 599–606.

– (2008): Decadal variations of intense typhoon occurrence in the western North Pacific. *Proceedings of the Royal Society A: Mathematical, Physical and Engineering Sciences*, 464.2089, 249–272.

Chauvin, F., Pilon, R., Palany, P. & Belmadani, A. (2019): Future changes in Atlantic hurricanes with the rotated-stretched ARPEGE-Climat at very high resolution. *Climate dynamics*, 54, 947–972.

Chauvin, F., Royer, J.-F. & Déqué, M. (2006): Response of hurricane-type vortices to global warming as simulated by ARPEGE-Climat at high resolution. *Climate Dynamics*, 27.4, 377–399.

Chavas, D. R. & Emanuel, K. (2010): A QuikSCAT climatology of tropical cyclone size. *Geophysical Research Letters*, 37.18.

Chu, P.-S. & Wang, J. (1997): Tropical cyclone occurrences in the vicinity of Hawaii: Are the differences between El Niño and non–El Niño years significant? *Journal of Climate*, 10.10, 2683–2689.

Cione, J. J. & Uhlhorn, E. W. (2003): Sea surface temperature variability in hurricanes: Implications with respect to intensity change. *Monthly Weather Review*, 131.8.

Craig, A., Valcke, S. & Coquart, L. (2017): Development and performance of a new version of the OASIS coupler, OASIS3-MCT_3. 0. *Geoscientific Model Development*, 10.9.

Davis, C. (2018): Resolving tropical cyclone intensity in models. *Geophysical Research Letters*, 45.4, 2082–2087.

Davis, C., Ahijevych, D. A., Wang, W. & Skamarock, W. C. (2016): Evaluating medium-range tropical cyclone forecasts in uniform-and variable-resolution global models. *Monthly Weather Review*, 144.11, 4141–4160.

Delworth, T. L., Rosati, A., Anderson, W., Adcroft, A. J., Balaji, V., Benson, R., Dixon, K., Griffies, S. M., Lee, H.-C., Pacanowski, R. C. et al., (2012): Simulated climate and climate change in the GFDL CM2. 5 high-resolution coupled climate model. *Journal of Climate*, 25.8, 2755–2781.

Demuth, J. L., DeMaria, M. & Knaff, J. A. (2006): Improvement of Advanced Microwave Sounding Unit Tropical Cyclone Intensity and Size Estimation Algorithms. *Journal of Applied Meteorology and Climatology*, 45.11, 1573–1581.

Donelan, M., Haus, B. K., Reul, N., Plant, W., Stiassnie, M., Graber, H. C., Brown, O. & Saltzman, E. (2004): On the limiting aerodynamic roughness of the ocean in very strong winds. *Geophysical Research Letters*, 31.18.

Elsner, J. B. & Kocher, B. (2000): Global tropical cyclone activity: A link to the North Atlantic Oscillation. *Geophysical Research Letters*, 27.1, 129–132.

Emanuel, K. (1987): The dependence of hurricane intensity on climate. *Nature*, 326.6112, 483–485.

– (2001): Contribution of tropical cyclones to meridional heat transport by the oceans. *Journal of Geophysical Research: Atmospheres*, 106.D14, 14771–14781.

– (2005): Increasing destructiveness of tropical cyclones over the past 30 years. *Nature*, 436.7051, 686–688.

– (2007): Environmental factors affecting tropical cyclone power dissipation. *Journal of Climate*, 20.22, 5497–5509.

Emanuel, K. & Nolan, D. S. (2004): “Tropical cyclone activity and the global climate system”. *26th Conference on Hurricanes and Tropical Meteorolgy*, pp. 240–241.

Evans, J. L. & Braun, A. (2012): A climatology of subtropical cyclones in the South Atlantic. *Journal of Climate*, 25.21, 7328–7340.

Eyring, V., Bony, S., Meehl, G. A., Senior, C. A., Stevens, B., Stouffer, R. J. & Taylor, K. E. (2016): Overview of the Coupled Model Intercomparison Project Phase 6 (CMIP6) experimental design and organization. *Geoscientific Model Development (Online)*, 9.LLNL-JRNL-736881.

Fink, A. H., Schrage, J. M. & Kotthaus, S. (2010): On the potential causes of the nonstationary correlations between West African precipitation and Atlantic hurricane activity. *Journal of Climate*, 23.20, 5437–5456.

Fulton, S. R. (2001): An adaptive multigrid barotropic tropical cyclone track model. *Monthly weather review*, 129.1, 138–151.

Gentry, M. S. & Lackmann, G. M. (2010): Sensitivity of simulated tropical cyclone structure and intensity to horizontal resolution. *Monthly Weather Review*, 138.3, 688–704.

Goldenberg, S. B., Landsea, C. W., Mestas-Nuñez, A. M. & Gray, W. M. (2001): The recent increase in Atlantic hurricane activity: Causes and implications. *Science*, 293.5529, 474–479.

Gray, W. M. (1975): Tropical cyclone genesis. *Atmospheric science paper; no. 234*,

– (1984): Atlantic seasonal hurricane frequency. Part I: El Niño and 30 mb quasi-biennial oscillation influences. *Monthly Weather Review*, 112.9, 1649–1668.

Gray, W. M. & Landsea, C. W. (1992): African rainfall as a precursor of hurricane-related destruction on the US East Coast. *Bulletin of the American Meteorological Society*, 73.9, 1352–1364.

Haarsma, R., Roberts, M., Vidale, P. L., Senior, C. A., Bellucci, A., Bao, Q., Chang, P., Corti, S., Fučkar, N. S., Guemas, V. et al., (2016): High resolution model intercomparison project (HighResMIP v1. 0) for CMIP6. *Geoscientific Model Development*, 9.11, 4185–4208.

Hagedorn, R., Doblas-Reyes, F. J. & Palmer, T. (2005): The rationale behind the success of multi-model ensembles in seasonal forecasting—I. Basic concept. *Tellus A: Dynamic Meteorology and Oceanography*, 57.3, 219–233.

Held, I. M. & Zhao, M. (2011): The response of tropical cyclone statistics to an increase in CO2 with fixed sea surface temperatures. *Journal of Climate*, 24.20, 5353–5364.

Hodges, K., Cobb, A. & Vidale, P. L. (2017): How Well Are Tropical Cyclones Represented in Reanalysis Datasets? *Journal of Climate*, 30.14, 5243–5264.

Hodges, R. E. & Elsner, J. B. (2012): The spatial pattern of the sun-hurricane connection across the North Atlantic. *ISRN Meteorology*, 2012.

Hortal, M. & Simmons, A. (1991): Use of reduced Gaussian grids in spectral models. *Monthly Weather Review*, 119.4, 1057–1074.

Irish, J. L., Resio, D. T. & Ratcliff, J. J. (2008): The influence of storm size on hurricane surge. *Journal of Physical Oceanography*, 38.9, 2003–2013.

Jiang, X., Zhao, M. & Waliser, D. E. (2012): Modulation of tropical cyclones over the eastern Pacific by the intraseasonal variability simulated in an AGCM. *Journal of Climate*, 25.19, 6524–6538.

Kantha, L. (2006): Time to replace the Saffir-Simpson hurricane scale? *Eos, Transactions American Geophysical Union*, 87.1, 3–6.

Kendon, E. J., Roberts, N. M., Senior, C. A. & Roberts, M. (2012): Realism of rainfall in a very high-resolution regional climate model. *Journal of Climate*, 25.17, 5791–5806.

Klotzbach, P. J. (2014): The Madden–Julian oscillation's impacts on worldwide tropical cyclone activity. *Journal of climate*, 27.6, 2317–2330.

Knapp, K. R., Kruk, M. C., Levinson, D. H., Diamond, H. J. & Neumann, C. J. (2010): The international best track archive for climate stewardship (IBTrACS) unifying tropical cyclone data. *Bulletin of the American Meteorological Society*, 91.3, 363–376.

Knutson, T., Camargo, S. J., Chan, J. C., Emanuel, K., Ho, C.-H., Kossin, J., Mohapatra, M., Satoh, M., Sugi, M., Walsh, K. et al., (2019): Tropical cyclones and climate change assessment: Part II. Projected response to anthropogenic warming. *Bulletin of the American Meteorological Society*, 2019.

Kossin, J. P., Camargo, S. J. & Sitkowski, M. (2010): Climate modulation of North Atlantic hurricane tracks. *Journal of Climate*, 23.11, 3057–3076.

Kozar, M. E. & Misra, V. (2019): "Integrated Kinetic Energy in North Atlantic Tropical Cyclones: Climatology, Analysis, and Seasonal Applications". *Hurricane Risk*. Springer, pp. 43–69.

Krishnamurti, T., Oosterhof, D. & Dignon, N. (1989): Hurricane prediction with a high resolution global model. *Monthly weather review*, 117.3, 631–669.

Lander, M. A. (1994): An exploratory analysis of the relationship between tropical storm formation in the western North Pacific and ENSO. *Monthly Weather Review*, 122.4, 636–651.

Landsea, C. W. (2000): Seasonal Predictability of Tropical Cyclones. *El Niño and the Southern Oscillation: multiscale variability and global and regional impacts*, 149.

Landsea, C. W., Bell, G. D., Gray, W. M. & Goldenberg, S. B. (1998): The extremely active 1995 Atlantic hurricane season: Environmental conditions and verification of seasonal forecasts. *Monthly Weather Review*, 126.5, 1174–1193.

Liang, L., Zhao, L., Gong, Y., Tian, F. & Wang, Z. (2012): Probability distribution of summer daily precipitation in the Huaihe basin of China based on Gamma distribution. *Acta Meteorologica Sinica*, 26.1, 72–84.

Liu, K. S. & Chan, J. C. (2008): Interdecadal variability of western North Pacific tropical cyclone tracks. *Journal of Climate*, 21.17, 4464–4476.

Lopes, R. H., Reid, I. & Hobson, P. R. (2007): The two-dimensional Kolmogorov-Smirnov test.

Madden, R. A. & Julian, P. R. (1972): Description of global-scale circulation cells in the tropics with a 40–50 day period. *Journal of the atmospheric sciences*, 29.6, 1109–1123.

– (1994): Observations of the 40–50-day tropical oscillation—A review. *Monthly weather review*, 122.5, 814–837.

Mahendran, M. (1998): Cyclone intensity categories. *Weather and forecasting*, 13.3, 878–883.

Manabe, S., Holloway Jr, J. L. & Stone, H. M. (1970): Tropical circulation in a time-integration of a global model of the atmosphere. *Journal of the Atmospheric Sciences*, 27.4, 580–613.

Mantua, N. J. & Hare, S. R. (2002): The Pacific decadal oscillation. *Journal of oceanography*, 58.1, 35–44.

Mantua, N. J., Hare, S. R., Zhang, Y., Wallace, J. M. & Francis, R. C. (1997): A Pacific interdecadal climate oscillation with impacts on salmon production. *Bulletin of the american Meteorological Society*, 78.6, 1069–1080.

Mei, W., Kamae, Y., Xie, S.-P. & Yoshida, K. (2019): Variability and Predictability of North Atlantic Hurricane Frequency in a Large Ensemble of High-Resolution Atmospheric Simulations. *Journal of Climate*, 32.11, 3153–3167.

Minobe, S., Kuwano-Yoshida, A., Komori, N., Xie, S.-P. & Small, R. J. (2008): Influence of the Gulf Stream on the troposphere. *Nature*, 452.7184, 206–209.

Misra, V., DiNapoli, S. & Powell, M. (2013): The track integrated kinetic energy of Atlantic tropical cyclones. *Monthly weather review*, 141.7, 2383–2389.

Mizuta, R. (2008): *Estimation of the future distribution of sea surface temperature and sea ice using the CMIP3 multi-model ensemble mean.* Meteorological Research Institute, Japan.

Molinari, J. & Vollaro, D. (1989): External influences on hurricane intensity. Part I: Outflow layer eddy angular momentum fluxes. *Journal of the Atmospheric Sciences*, 46.8, 1093–1105.

Morgan, E. C., Lackner, M., Vogel, R. M. & Baise, L. G. (2011): Probability distributions for offshore wind speeds. *Energy Conversion and Management*, 52.1, 15–26.

Mozer, J. & Zehnder, J. (1996): Lee vorticity Production by Large-Scale Tropical Mountain Ranges. Part I: Eastern North Pacific Tropical Cyclogenesis. *Journal of The Atmospheric Sciences - J ATMOS SCI*, 53, 521–538.

Munich Re (2018): The natural disasters of 2018 in figures. URL: https://www.munichre.com/topics-online/en/climate-change-and-natural-disasters/natural-disasters/the-natural-disasters-of-2018-in-figures.html.

Nicholls, N. (1979): A possible method for predicting seasonal tropical cyclone activity in the Australian region. *Monthly Weather Review*, 107.9, 1221–1224.

NOAA (2018): Costliest U.S. tropical cyclones tables updated. URL: https://www.nhc.noaa.gov/news/UpdatedCostliest.pdf.

– (2019): The Saffir-Simpson Hurricane Wind Scale. URL: https://www.nhc.noaa.gov/pdf/sshws.pdf.

O'Reilly, C. H., Minobe, S. & Kuwano-Yoshida, A. (2016): The influence of the Gulf Stream on wintertime European blocking. *Climate Dynamics*, 47.5-6, 1545–1567.

Patricola, C. M., Saravanan, R. & Chang, P. (2014): The impact of the El Niño–Southern Oscillation and Atlantic meridional mode on seasonal Atlantic tropical cyclone activity. *Journal of Climate*, 27.14, 5311–5328.

Pielke, R. A. & Landsea, C. N. (1999): La nina, el nino, and atlantic hurricane damages in the united states. *Bulletin of the American Meteorological Society*, 80.10, 2027–2034.

Powell, M. D. & Reinhold, T. A. (2007): Tropical cyclone destructive potential by integrated kinetic energy. *Bulletin of the American Meteorological Society*, 88.4, 513–526.

Powell, M. D., Vickery, P. J. & Reinhold, T. A. (2003): Reduced drag coefficient for high wind speeds in tropical cyclones. *Nature*, 422.6929, 279–283.

Ramsay, H. (2017): “The global climatology of tropical cyclones”. *Oxford Research Encyclopedia of Natural Hazard Science.*

Revell, C. G. & Goulter, S. W. (1986): South Pacific tropical cyclones and the Southern Oscillation. *Monthly Weather Review*, 114.6, 1138–1145.

Roberts, M., Camp, J., Seddon, J., Vidale, P. L., Hodges, K., Vanniere, B., Mecking, J., Haarsma, R., Bellucci, A., Scoccimarro, E. et al., (subm.): Projected Future Changes in Tropical Cyclones using the CMIP6 HighResMIP Multi-model Ensemble.

Roberts, M., Camp, J., Seddon, J., Vidale, P. L., Hodges, K., Vanniere, B., Mecking, J., Haarsma, R., Bellucci, A., Scoccimarro, E. et al., (2020): Impact of Model Resolution on Tropical Cyclone Simulation Using the HighResMIP–PRIMAVERA Multimodel Ensemble. *Journal of Climate*, 33.7, 2557–2583.

Rudeva, I. & Gulev, S. K. (2007): Climatology of cyclone size characteristics and their changes during the cyclone life cycle. *Monthly weather review*, 135.7, 2568–2587.

Sakamoto, T. T., Komuro, Y., Nishimura, T., Ishii, M., Tatebe, H., Shiogama, H., Hasegawa, A., Toyoda, T., Mori, M., Suzuki, T. et al., (2012): MIROC4h—a new high-resolution atmosphere-ocean coupled general circulation model. *Journal of the Meteorological Society of Japan. Ser. II*, 90.3, 325–359.

Scoccimarro, E., Gualdi, S., Villarini, G., Vecchi, G. A., Zhao, M., Walsh, K. & Navarra, A. (2014): Intense precipitation events associated with landfalling tropical cyclones in response to a warmer climate and increased CO2. *Journal of climate*, 27.12, 4642–4654.

Shaevitz, D. A., Camargo, S. J., Sobel, A. H., Jonas, J. A., Kim, D., Kumar, A., LaRow, T. E., Lim, Y.-K., Murakami, H., Reed, K. A. et al., (2014): Characteristics of tropical cyclones in high-resolution models in the present climate. *Journal of Advances in Modeling Earth Systems*, 6.4, 1154–1172.

Shaffrey, L., Stevens, I., Norton, W., Roberts, M., Vidale, P.-L., Harle, J., Jrrar, A., Stevens, D., Woodage, M. J., Demory, M.-E. et al., (2009): UK HiGEM: The new UK high-resolution global environment model—Model description and basic evaluation. *Journal of Climate*, 22.8, 1861–1896.

Shapiro, L. J. (1989): The relationship of the quasi-biennial oscillation to Atlantic tropical storm activity. *Monthly weather review*, 117.7, 1545–1552.

Simpson, R. (1971): "A proposed scale for ranking hurricanes by intensity". *Minutes of the Eighth NOAA, NWS Hurricane Conference, Miami.*

Skamarock, W. C. & Klemp, J. B. (1993): Adaptive grid refinement for two-dimensional and three-dimensional nonhydrostatic atmospheric flow. *Monthly Weather Review*, 121.3, 788–804.

Stevens, B., Fiedler, S., Kinne, S., Peters, K., Rast, S., Müsse, J., Smith, S. J. & Mauritsen, T. (2016): Simple Plumes: A parameterization of anthropogenic aerosol optical properties and an associated Twomey effect for climate studies, Geosci. Model Dev. Discuss. *Model Dev. Discuss., doi: http://dx. doi. org/10.5194/gmd-2016-189*,

Sugi, M., Murakami, H. & Yoshimura, J. (2012): On the mechanism of tropical cyclone frequency changes due to global warming. *Journal of the Meteorological Society of Japan. Ser. II*, 90, 397–408.

Sun, Y., Zhong, Z., Li, T., Yi, L., Hu, Y., Wan, H., Chen, H., Liao, Q., Ma, C. & Li, Q. (2017): Impact of Ocean Warming on Tropical Cyclone Size and Its Destructiveness. *Scientific Reports*, 7.

Tang, Y., Lean, H. W. & Bornemann, J. (2013): The benefits of the Met Office variable resolution NWP model for forecasting convection. *Meteorological Applications*, 20.4, 417–426.

Terry, J. (2007): Tropical Cyclogenesis: Climatology and Impacts in the South Pacific. *Springer New York*, 15–25.

Titchner, H. A. & Rayner, N. A. (2014): The Met Office Hadley Centre sea ice and sea surface temperature data set, version 2: 1. Sea ice concentrations. *Journal of Geophysical Research: Atmospheres*, 119.6, 2864–2889.

Trenberth, K. E. (1997): The definition of el nino. *Bulletin of the American Meteorological Society*, 78.12, 2771–2778.

Trenberth, K., Zhang, R. & National Center for Atmospheric Research Staff (Eds.) (2019): The Climate Data Guide: Atlantic Multi-decadal Oscillation (AMO). URL: https://climatedataguide.ucar.edu/climate-data/atlantic-multi-decadal-oscillation-amo.

Ullrich, P. A. & Zarzycki, C. M. (2017): TempestExtremes: a framework for scale-insensitive pointwise feature tracking on unstructured grids. *Geoscientific Model Development*, 10.3, 1069–1090.

Villarini, G., Lavers, D. A., Scoccimarro, E., Zhao, M., Wehner, M. F., Vecchi, G. A., Knutson, T. & Reed, K. A. (2014): Sensitivity of tropical cyclone rainfall to idealized global-scale forcings. *Journal of climate*, 27.12, 4622–4641.

Villarini, G. & Vecchi, G. A. (2012): North Atlantic power dissipation index (PDI) and accumulated cyclone energy (ACE): Statistical modeling and sensitivity to sea surface temperature changes. *Journal of climate*, 25.2, 625–637.

Vimont, D. J. & Kossin, J. P. (2007): The Atlantic meridional mode and hurricane activity. *Geophysical Research Letters*, 34.7.

Voldoire, A., Saint-Martin, D., Sénési, S., Decharme, B., Alias, A., Chevallier, M., Colin, J., Guérémy, J.-F., Michou, M., Moine, M.-P. et al., (2019): Evaluation of CMIP6 DECK Experiments With CNRM-CM6-1. *Journal of Advances in Modeling Earth Systems*, 11.7, 2177–2213.

Walsh, K. J. & Ryan, B. F. (2000): Tropical cyclone intensity increase near Australia as a result of climate change. *Journal of Climate*, 13.16, 3029–3036.

Walsh, K., McBride, J. L., Klotzbach, P. J., Balachandran, S., Camargo, S. J., Holland, G., Knutson, T., Kossin, J. P., Lee, T.-c., Sobel, A. H. et al., (2016): Tropical cyclones and climate change. *Wiley Interdisciplinary Reviews: Climate Change*, 7.1, 65–89.

Wang, C., Liu, H., Lee, S.-K. & Atlas, R. (2011): Impact of the Atlantic warm pool on United States landfalling hurricanes. *Geophysical Research Letters*, 38.19.

Wang, S. & Toumi, R. (2016): On the relationship between hurricane cost and the integrated wind profile. *Environmental Research Letters*, 11.11, 114005.

Williams, K., Harris, C., Bodas-Salcedo, A., Camp, J., Comer, R., Copsey, D., Fereday, D., Graham, T., Hill, R., Hinton, T. et al., (2015): The met office global coupled model 2.0 (GC2) configuration. *Geoscientific Model Development*, 8.5, 1509–1524.

World Economic Forum (2019): The Global Risks Report 2019. URL: http://www3.weforum.org/docs/WEF_Global_Risks_Report_2019.pdf.

Yu, J.-Y. & Chiu, P.-G. (2012): Contrasting Various Metrics for Measuring Tropical Cyclone Activity. *Terrestrial, Atmospheric & Oceanic Sciences*, 23.3.

Yu, J.-Y., Chou, C. & Chiu, P.-G. (2009): A revised accumulated cyclone energy index. *Geophysical research letters*, 36.14.

Zarzycki, C. M. & Ullrich, P. A. (2017): Assessing sensitivities in algorithmic detection of tropical cyclones in climate data. *Geophysical Research Letters*, 44.2, 1141–1149.

Zarzycki, C. M., Jablonowski, C. & Taylor, M. A. (2014): Using variable-resolution meshes to model tropical cyclones in the Community Atmosphere Model. *Monthly Weather Review*, 142.3, 1221–1239.

Zehnder, J. (1991): The Interaction of Planetary-Scale Tropical Easterly Waves with Topography: A Mechanism for the Initiation of Tropical Cyclones. *Journal of Atmospheric Sciences*, 48.10, 1217–1230.

Zhai, A. R. & Jiang, J. H. (2014): Dependence of US hurricane economic loss on maximum wind speed and storm size. *Environmental Research Letters*, 9.6.

Zhang, C. (2005): Madden-julian oscillation. *Reviews of Geophysics*, 43.2.

Zhang, Y., Wallace, J. M. & Battisti, D. S. (1997): ENSO-like interdecadal variability: 1900–93. *Journal of climate*, 10.5, 1004–1020.

Zhao, M., Held, I. M., Lin, S.-J. & Vecchi, G. A. (2009): Simulations of global hurricane climatology, interannual variability, and response to global warming using a 50-km resolution GCM. *Journal of Climate*, 22.24, 6653–6678.

Appendix

This section provides additional material that has not been placed in the main body of this report, but which has been referenced to. This includes equations, figures such as close-up views for the individual basins for track and IKE density as well as boxplots.

The IKE area used for *Hurricanes Camille*, *Ivan* and *Katrina* in Fig. 18a in Sect. 5.2 is derived from Powell & Reinhold (2007) using the radius of the maximum wind speed R_{max} and the radius of the outer threshold of tropical storm strength R_{18}, assuming a circular storm and wind speeds below tropical storm strength at radii below R_{max}:

$$IKE\ area = \pi \cdot (R_{18}^2 - R_{max}^2). \tag{21}$$

This equation slightly underestimates $IKE\ area$, because, in reality, the wind speeds at radii below R_{max} are not everywhere lower than tropical storm strength, especially close to R_{max}. Thus, they contribute to the $IKE\ area$, but this contribution is argued to be small.

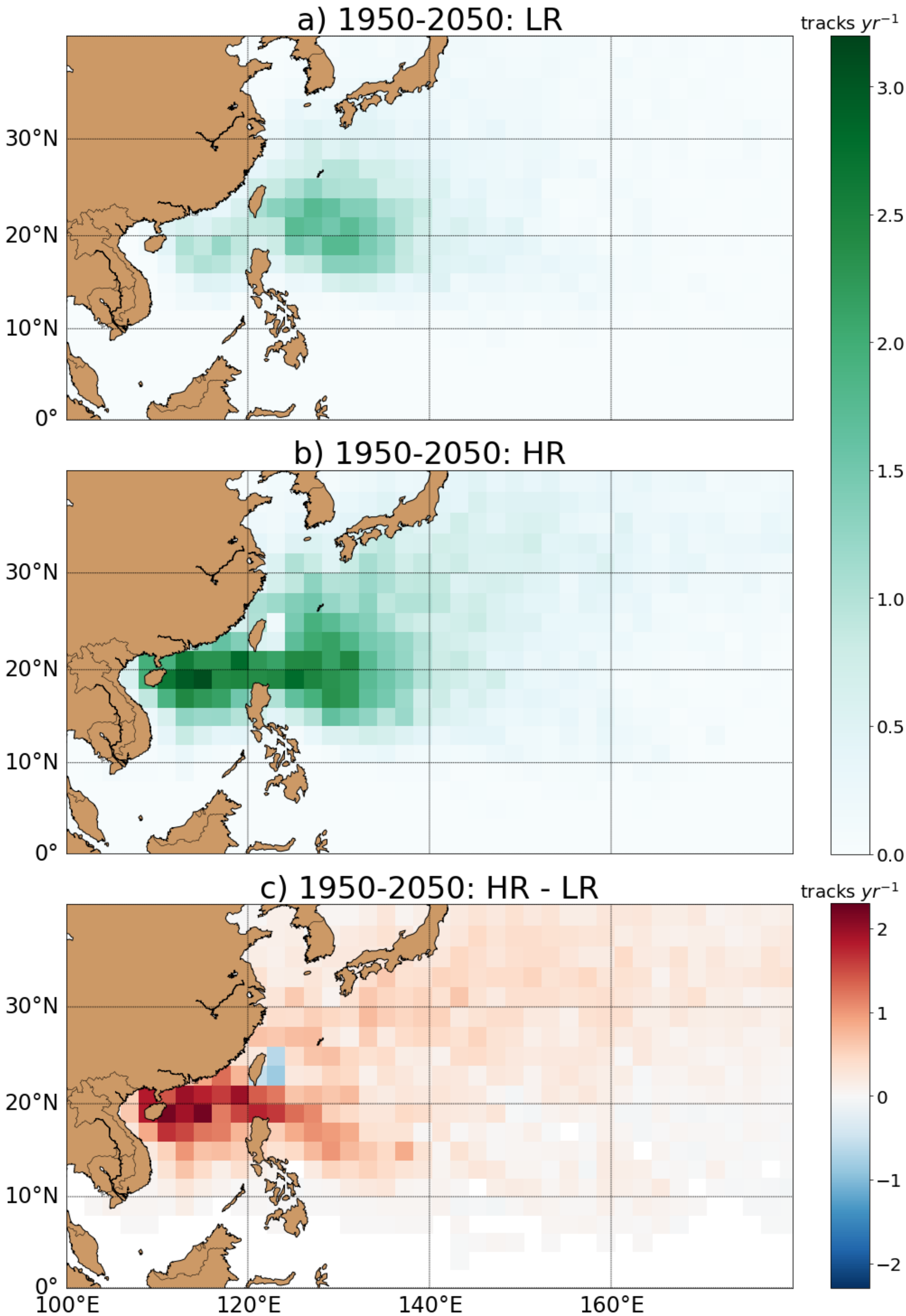

Figure 25: Track distribution per year in the WNP per $2^\circ \times 2^\circ$ grid cells from 1950-2050 for (a) LR and (b) HR, (c) difference between HR and LR. All storm transits in the respective grid boxes were counted and averaged over time.

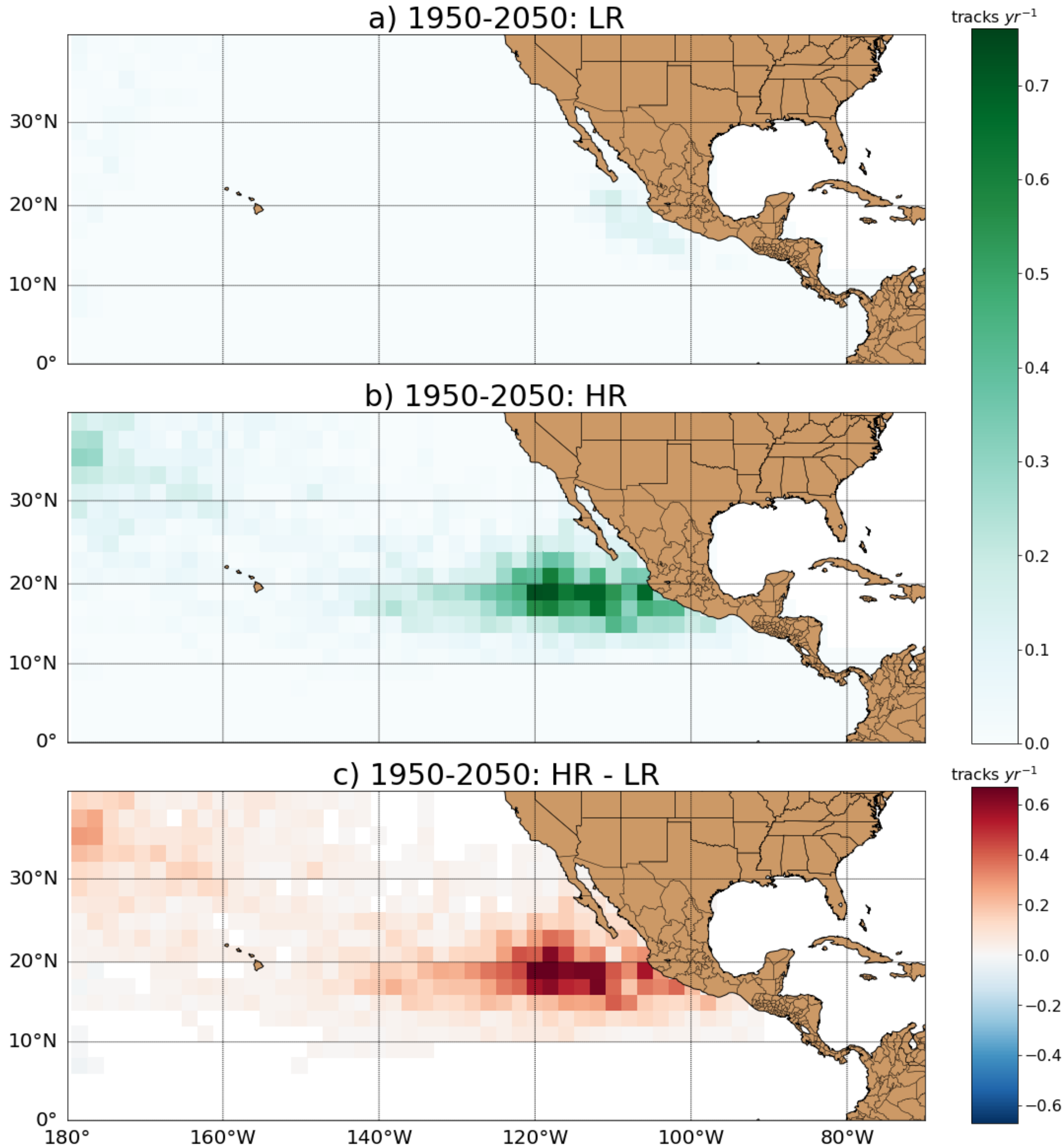

Figure 26: Track distribution per year in the ENP per $2^\circ \times 2^\circ$ grid cells from 1950-2050 for (a) LR and (b) HR, (c) difference between HR and LR. All storm transits in the respective grid boxes were counted and averaged over time.

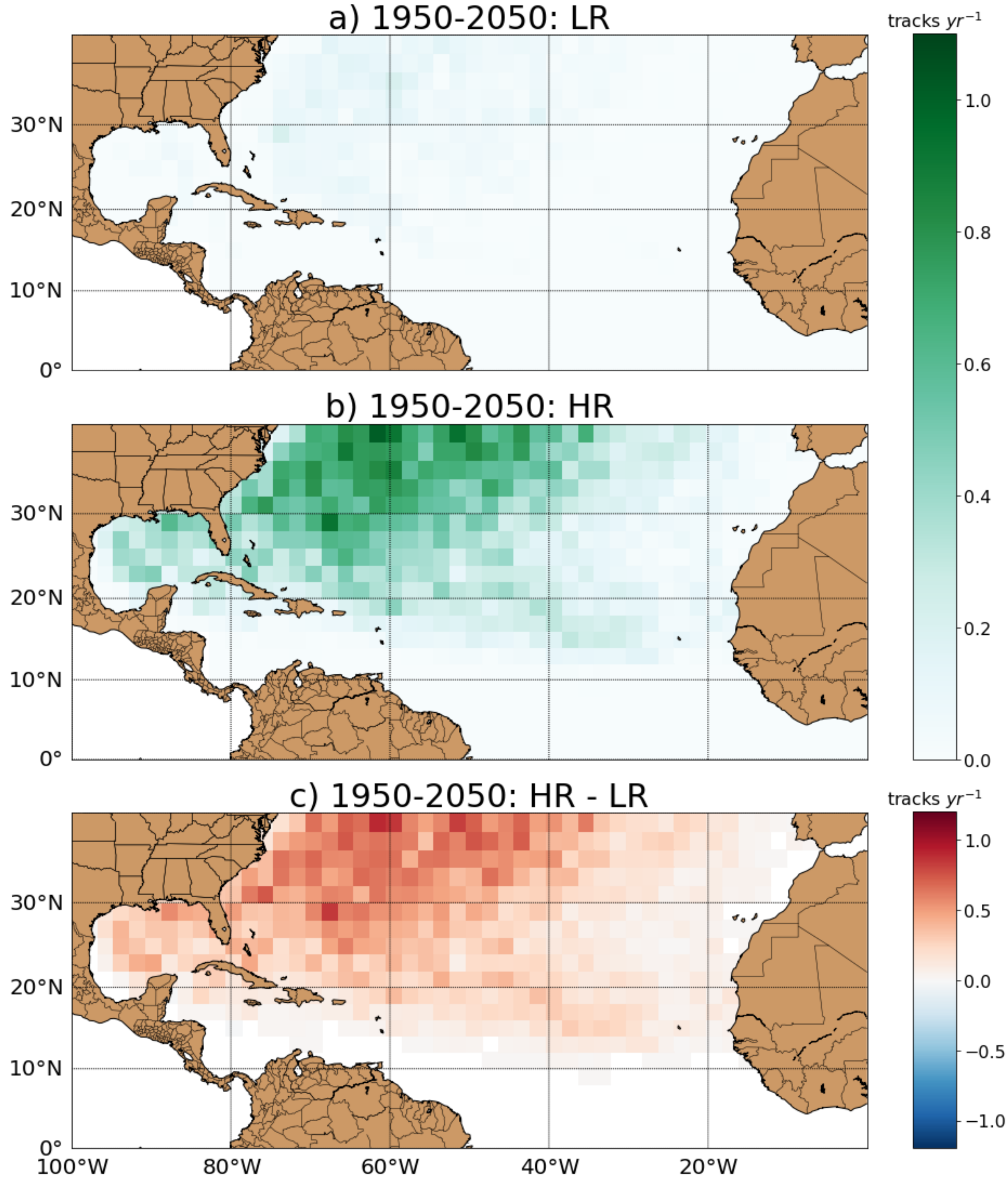

Figure 27: Track distribution per year in the NA per $2° \times 2°$ grid cells from 1950-2050 for (a) LR and (b) HR, (c) difference between HR and LR. All storm transits in the respective grid boxes were counted and averaged over time.

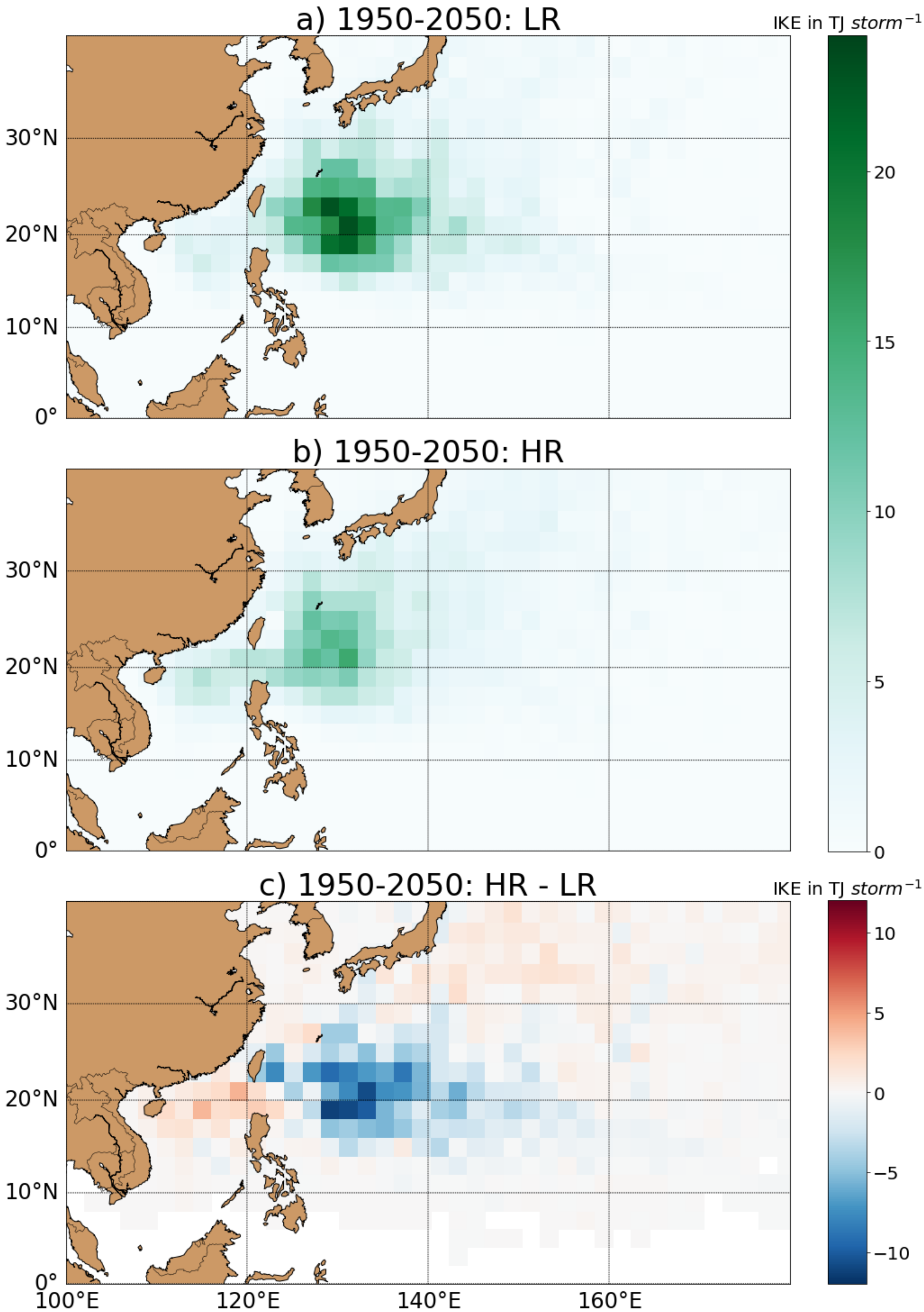

Figure 28: Maximum IKE distribution per storm in the WNP per $2^\circ \times 2^\circ$ grid cells for (a) LR and (b) HR from 1950-2050, (c) difference between HR and LR. The IKE associated with all storm transits in the respective grid boxes was summed up and then averaged over all those storm transits.

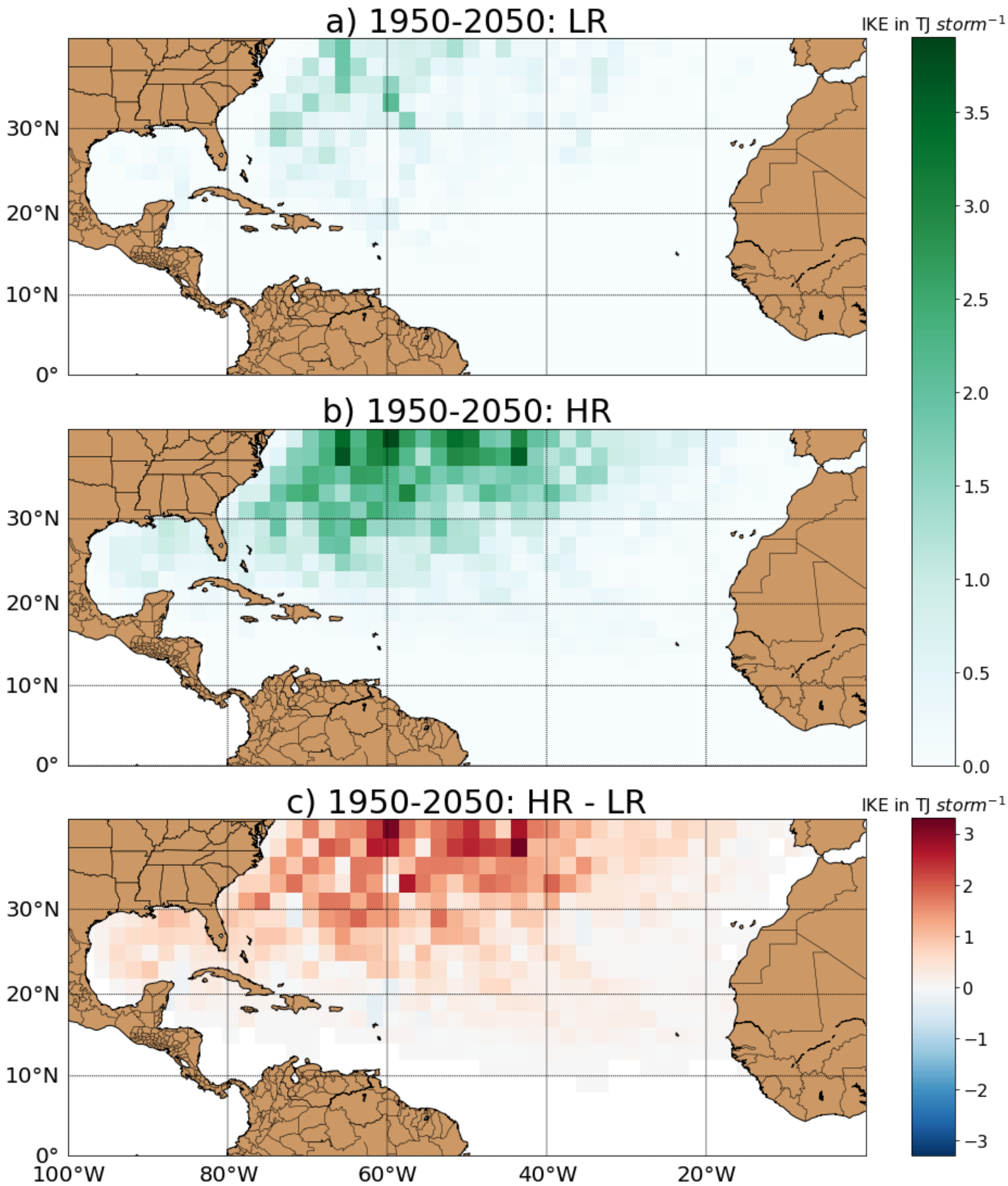

Figure 29: Maximum IKE distribution per storm in the NA per $2^\circ \times 2^\circ$ grid cells for (a) LR and (b) HR from 1950-2050, (c) difference between HR and LR. The IKE associated with all storm transits in the respective grid boxes was summed up and then averaged over all those storm transits.

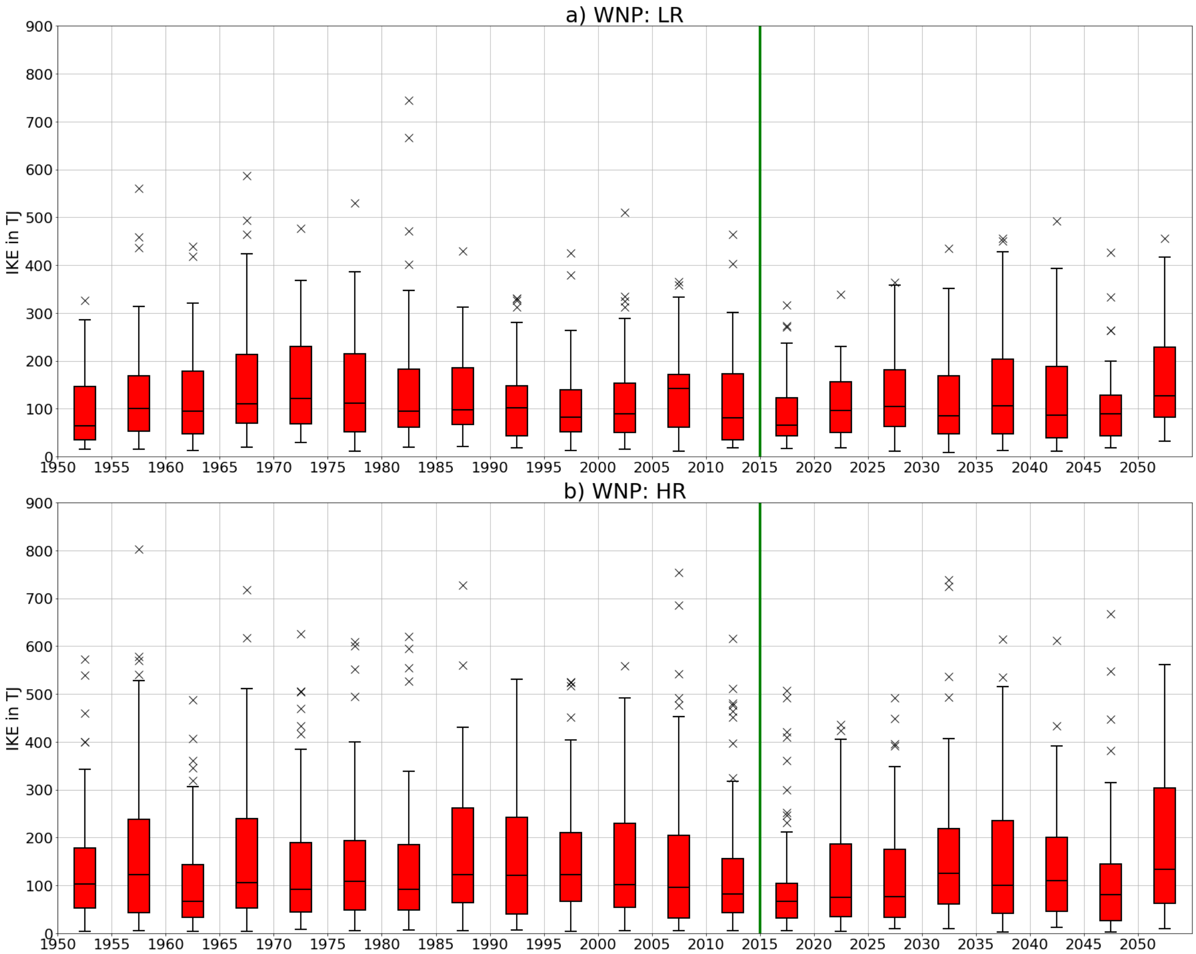

Figure 30: Boxplot of all storms in the WNP from 1950-2050 for LR (a) and HR (b). The storms are aggregated in 5-year intervals (e.g., from 1950-1954, 1955-1959 etc.) with the box being centred in the middle of the respective interval. The black bar within the boxes depicts the median (50^{th} percentile), while the lower and upper boundaries of the boxes represent the 25^{th} and 75^{th} percentiles, respectively. The lower and upper whiskers represent the 5^{th} and 95^{th} percentiles. The crosses mark all the storms which lie outside of the 95^{th} percentile. The green line represents the transition from present to future time period.

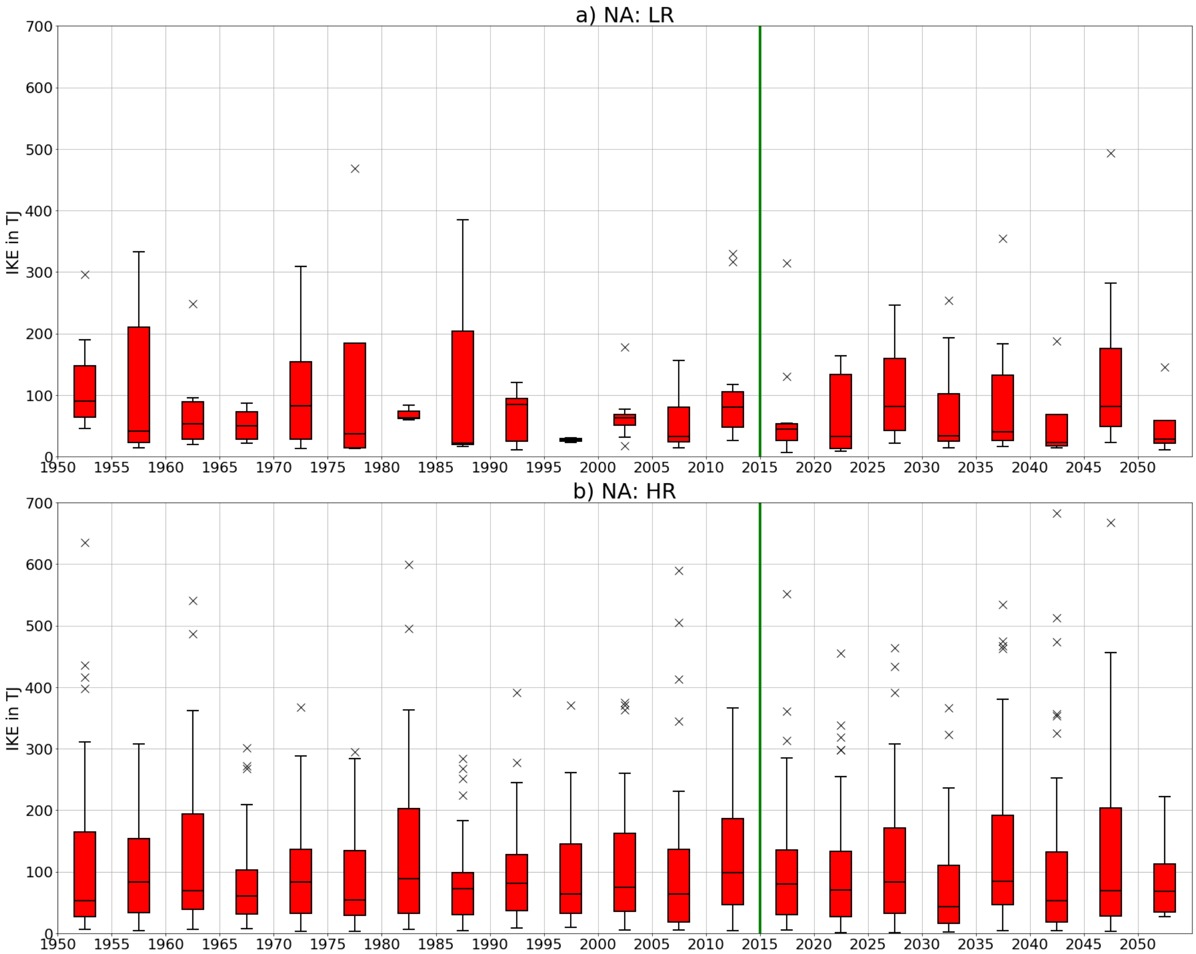

Figure 31: Boxplot of all storms in the NA from 1950-2050 for LR (a) and HR (b). The storms are aggregated in 5-year intervals (e.g., from 1950-1954, 1955-1959 etc.) with the box being centred in the middle of the respective interval. The black bar within the boxes depicts the median (50^{th} percentile), while the lower and upper boundaries of the boxes represent the 25^{th} and 75^{th} percentiles, respectively. The lower and upper whiskers represent the 5^{th} and 95^{th} percentiles. The crosses mark all the storms which lie outside of the 95^{th} percentile. The green line represents the transition from present to future time period.

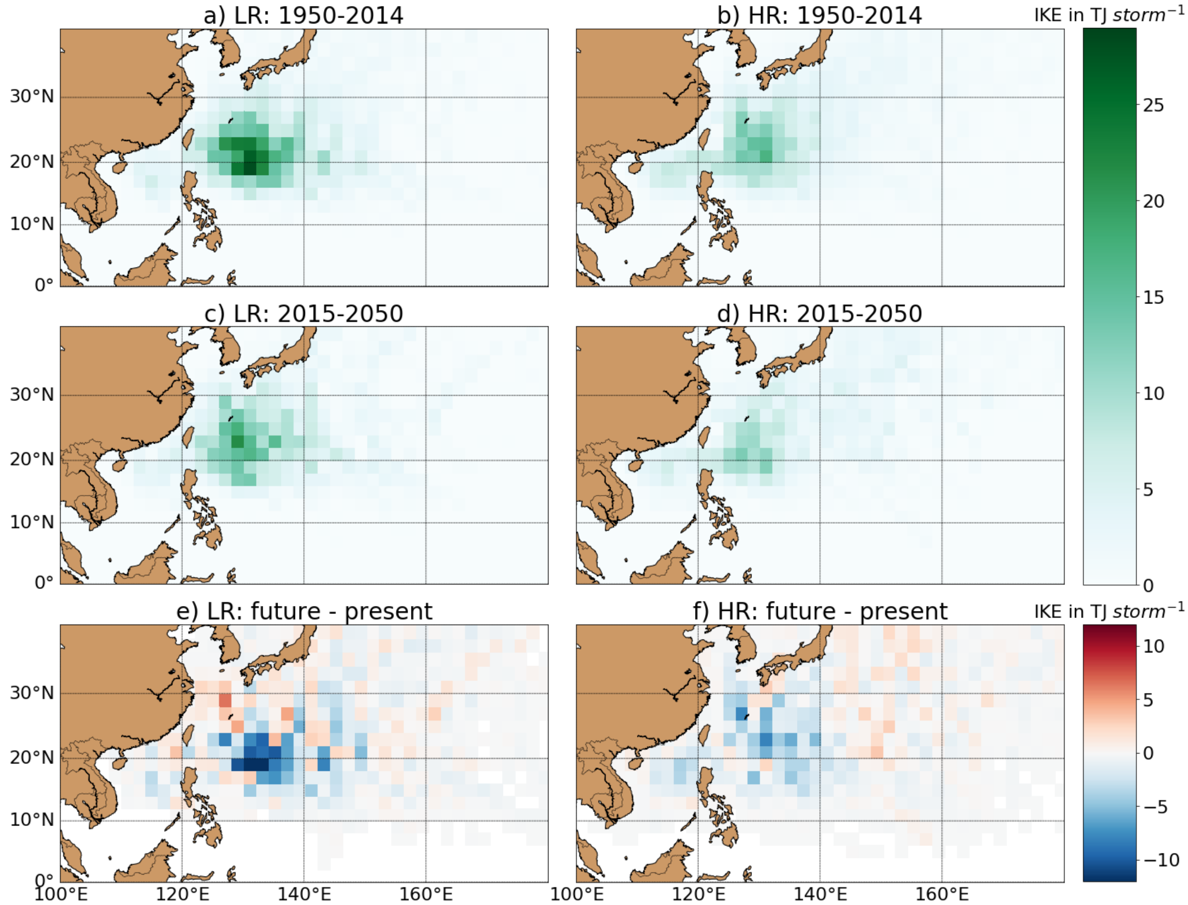

Figure 32: Maximum IKE distribution per storm in the WNP per $2^{\circ} \times 2^{\circ}$ grid cells for LR and HR from 1950-2014 and 2015-2050 (a-d), (e) and (f) differences between future and present. The IKE associated with all storm transits in the respective grid boxes was summed up and then averaged over all those storm transits.

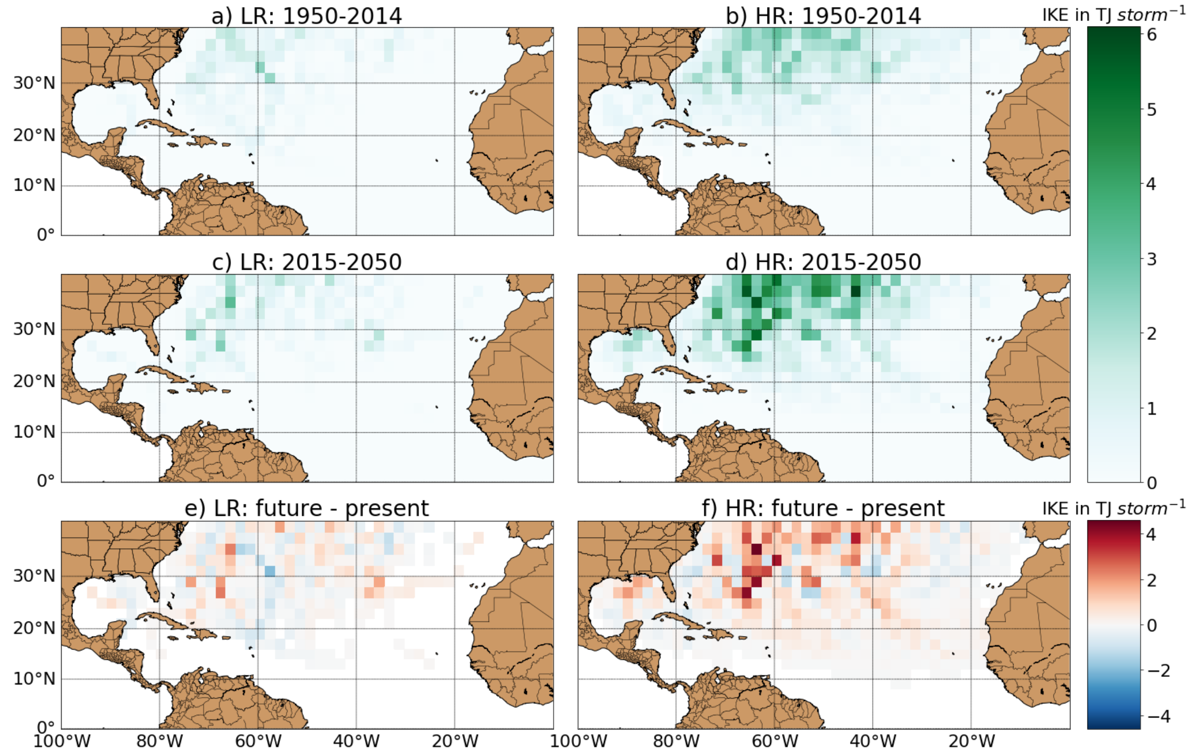

Figure 33: Maximum IKE distribution per storm in the NA per $2^\circ \times 2^\circ$ grid cells for LR and HR from 1950-2014 and 2015-2050 (a-d), (e) and (f) differences between future and present. The IKE associated with all storm transits in the respective grid boxes was summed up and then averaged over all those storm transits.

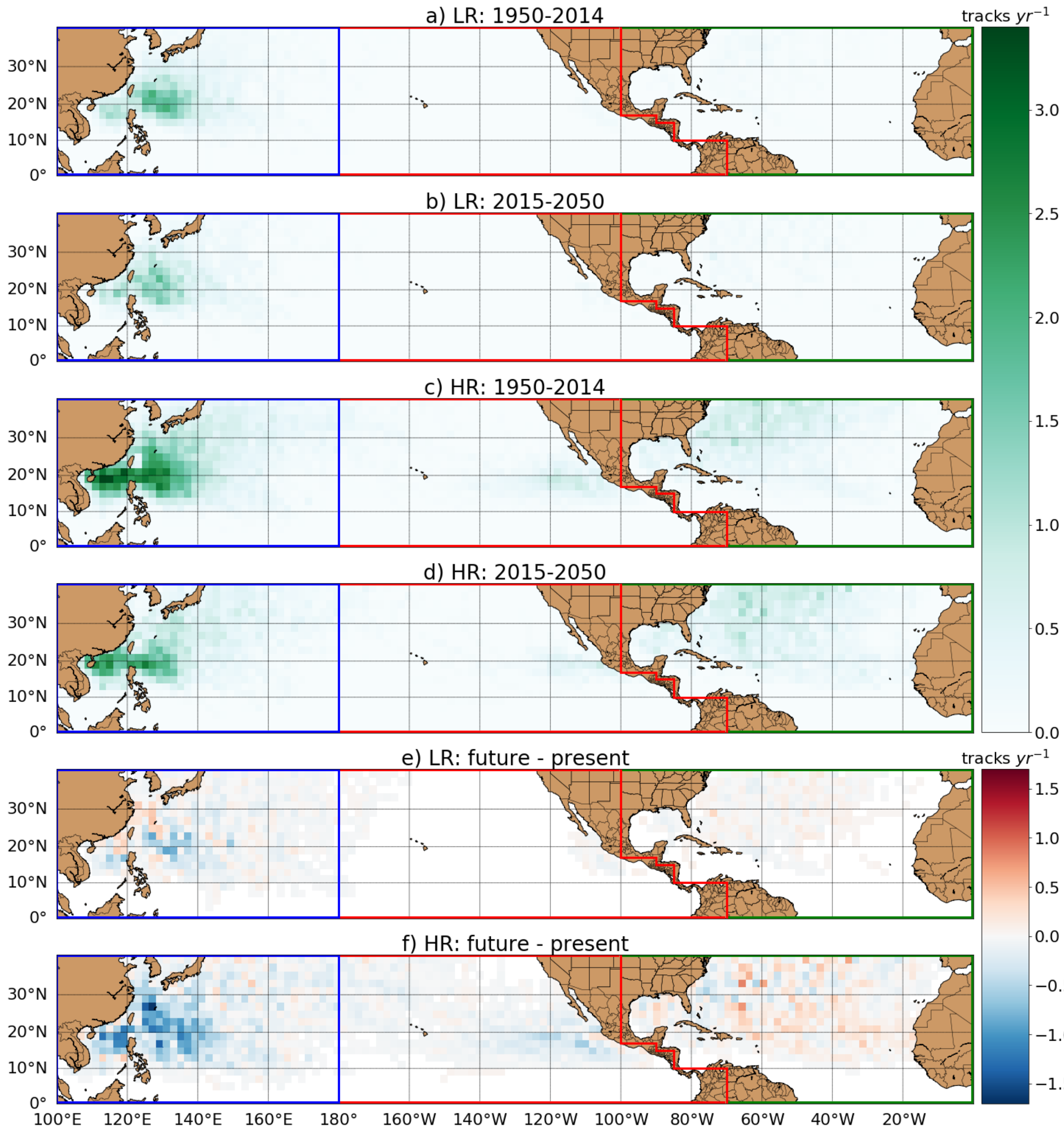

Figure 34: Track distribution per year in the NH per 2° × 2° grid cells from 1950-2014 and 2015-2050 for LR and HR (a-d), (e) and (f) differences between future and present. All storm transits in the respective grid boxes were counted and averaged over time.

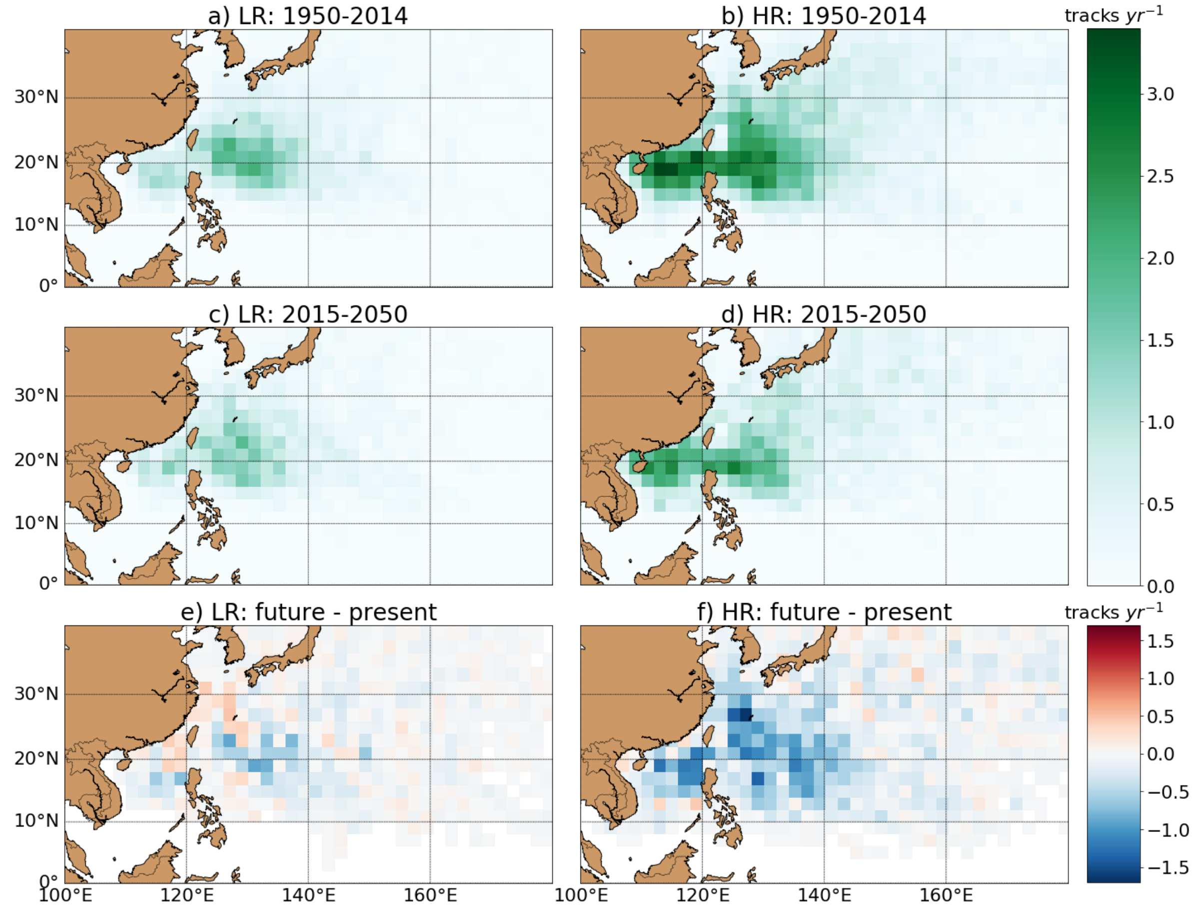

Figure 35: Track distribution per year in the WNP per $2° \times 2°$ grid cells from 1950-2014 and 2015-2050 for LR and HR (a-d), (e) and (f) differences between future and present. All storm transits in the respective grid boxes were counted and averaged over time.

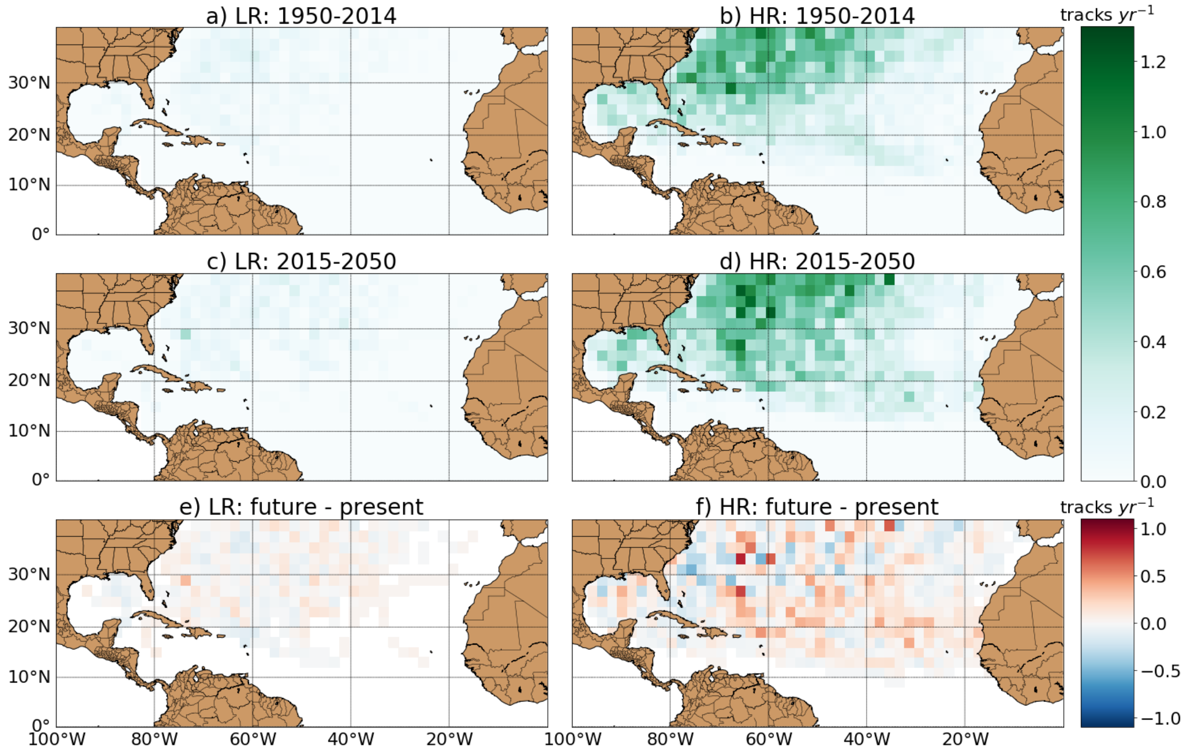

Figure 36: Track distribution per year in the NA per 2° × 2° grid cells from 1950-2014 and 2015-2050 for LR and HR (a-d), (e) and (f) differences between future and present. All storm transits in the respective grid boxes were counted and averaged over time.

Acknowledgements

I would like to thank Prof. Dr. Katja Matthes for her guidance throughout this thesis and for making it possible to compose this thesis in cooperation with the *Barcelona Supercomputing Center* in Barcelona, Spain (BSC).

Furthermore, I would like to thank the BSC, in particular Dr. Louis-Philippe Caron and Dr. Simon Wild, for giving me the opportunity to write this thesis in collaboration with the department of *Climate Prediction*. I am very thankful for all their advice and support during every stage of this thesis. It was a great pleasure to work under their supervision which has deeply inspired me to follow a career path related to the fascinating topic of tropical cyclones.

Also, I would like to thank Saskia Loosevelt from the BSC for providing valuable help regarding technical issues.

Lastly, I would like to thank my family and friends for all their support and encouragement without whom it would have not been possible to complete this work.

Erklärung

Hiermit erkläre ich, dass ich die vorliegende Arbeit selbständig und ohne fremde Hilfe angefertigt und keine anderen als die angegeben Quellen und Hilfsmittel verwendet habe.

Hiermit bestätige ich, dass die digital eingereichte Fassung meiner Masterarbeit mit der gedruckten Fassung übereinstimmt.

Die eingereichte schriftliche Fassung der Arbeit entspricht der auf dem elektronischen Speichermedium.

Weiter versichere ich, dass diese Arbeit noch nicht als Abschlussarbeit an anderer Stelle vorgelegen hat.

Kiel, den 26. Mai 2020 — P. Kreußler

Kiel, den 26. Mai 2020 — Philip Kreußler